The Meteoritical Society

Meteoritics & Planetary Science 47, Nr 4, 471–524 (2012)
doi: 10.1111/j.1945-5100.2012.01337.x

Comprehensive examination of large mineral and rock fragments in Stardust tracks: Mineralogy, analogous extraterrestrial materials, and source regions

David J. JOSWIAK[1*], Donald E. BROWNLEE[1], Graciela MATRAJT[1], Andrew J. WESTPHAL[2], Christopher J. SNEAD[3] and Zack GAINSFORTH[2]

[1]Department of Astronomy, University of Washington, Seattle, Washington 98195, USA
[2]Space Sciences Laboratory, University of California at Berkeley, Berkeley, California 94720, USA
[3]Department of Earth and Space Sciences, UCLA, Los Angeles, California 90095, USA
[*]Corresponding author. E-mail: joswiak@astro.washington.edu

(Received 26 May 2011; revision accepted 11 January 2012)

Abstract–Transmission electron microscopy examination of 87 large fragments from 16 carrot-shaped and bulbous Stardust (SD) tracks was performed to study the range and diversity of materials present in comet Wild 2. Olivines and low-Ca pyroxenes represent the largest proportions of fragments observed; however, a wide range of minerals and rocks were found including probable ferromagnesian, Al-rich and Si-rich chondrule fragments, a refractory inclusion, possible matrix mineral/lithic clasts, and probable condensate minerals. These materials, combined with fine-grained components in the tracks, are analogous to components in unequilibrated chondrite meteorites and cluster interplanetary dust particles (IDPs). Two unusual lithologies in the bulbous tracks are only observed in chondritic porous IDPs and may have direct links to IDPs. The absence of phyllosilicates indicates that comet Wild 2 may be a "dry" comet that did not accrete or form significant amounts of hydrated phases. Some large mineral fragments in the SD tracks are analogous to large mineral IDPs. The large variations of the coarse-grained components within and between all 16 tracks show that comet Wild 2 is mineralogically diverse and unequilibrated on nearly all scales and must have accreted materials from diverse source regions that were widely dispersed throughout the solar nebula.

INTRODUCTION

On January 2, 2004, the Stardust (SD) spacecraft successfully collected thousands of particles from the nucleus of comet 81P/Wild 2, a Jupiter family comet that is believed to have formed in the Kuiper belt ~4.6 Ga. Comets contain materials that accreted at the edge of the solar system and should preserve records of its early history (Brownlee 2004). Direct study of these materials therefore is vital to improve our understanding of the origin and early evolution of the solar system.

Since the return of the Stardust capsule to Earth in January of 2006, numerous laboratories have been examining the captured samples using a variety of techniques. So far, a large range of crystalline materials recovered from the silica aerogel collector have been found including CAIs (calcium aluminum-rich inclusions) (Simon et al. 2008; Chi et al. 2009; Matzel et al. 2010); ferromagnesian chondrules or chondrule fragments (Nakamura et al. 2008; Gainsforth et al. 2010); an Al-rich chondrule fragment or amoeboid olivine aggregate (AOA) (Joswiak et al. 2010); and a range of silicate, oxide, and sulfide minerals (Zolensky et al. 2006; Joswiak et al. 2007; Leroux et al. 2008a). One surprise has been the low abundance of carbonaceous matter (Matrajt et al. 2008) and presolar grains (McKeegan et al. 2006; Stadermann et al. 2008; Messenger et al. 2009). It remains unclear if these low abundances are intrinsic to comet Wild 2 or if they result from effects of the capture process that systematically degrades captured materials.

A summary of the coarse fragments observed from a sampling of the SD tracks was given by Zolensky et al. (2006) during the preliminary mineralogy and petrology examination of the samples. Subsequently, other studies have also examined large fragments in the tracks (Joswiak

et al. 2007, 2009; Leroux et al. 2008a; Nakamura et al. 2008; Schmitz and Brenker 2008; Stephan et al. 2008; Tomeoka et al. 2008; Zolensky et al. 2008; Jacob et al. 2009; Gainsforth et al. 2010; Nakamura-Messenger et al. 2011). Only a few studies (Nakamura-Messenger et al. 2011), however, have methodically looked at the range and abundances of the coarse-grained materials from individual SD tracks with the purpose of reconstructing the original impacting particles prior to capture in aerogel. Important questions that this approach can answer include: What range of mineralogical heterogeneity was present in coarse fragments in each captured particle? What is the mineralogical diversity between different SD tracks? How do the reconstructed Wild 2 particles compare with other extraterrestrial (ET) materials? How primitive are the samples that were collected by Stardust? Were the clumps of comet material that produced individual tracks just random clusters of unrelated materials or did they have a common origin such as different portions of a fractured chondrule? Here, we report on systematic dissections of entire tracks, or portions of tracks, examining all or most large fragments including terminal particles and other large fragments embedded in track walls or in short side tracks. We provide detailed mineralogical and petrologic information on most of the fragments we observed, thereby providing important context information on the range of fragments in each track. Such a comprehensive examination can greatly improve our understanding of the relationships and scope of the largest components that were present in the original particles.

In total, we examined 87 coarse fragments from 16 tracks largely by transmission electron microscopy (TEM). We use the results of our observations to reconstruct the likely physical and mineralogical characteristics of the impactors that produced the tracks, assess possible origins of many of the large fragments, suggest analog ET materials that have properties similar to the impactors, and judge the likely primitiveness of the samples. We conclude that the particles from comet Wild 2 are not mineralogically equilibrated and are similar to and possibly identical to components that have also been found in large mineral IDPs (interplanetary dust particles), cluster IDPs, and chondrites, including components such as chondrules (fragments), refractory inclusions, condensate minerals, and matrix clasts. The results indicate that comet Wild 2 is heterogeneous and probably accreted materials that formed in diverse source regions that were widely dispersed in the solar nebula.

SAMPLE PREPARATION AND ANALYTICAL TECHNIQUES

Aerogel keystones (Westphal et al. 2004) containing entire tracks or portions of tracks were prepared at the curatorial facility at the Johnson Space Center. Tracks 10 and 41 were not cut into keystones, but were processed in their original irregular shaped chips of silica aerogel. To prepare the samples for ultramicrotomy and improve the optical properties of the aerogel and track fragments and to minimize the risk of sample loss, the keystones or aerogel chips were flattened between clean glass microscope slides and embedded in acrylic resin. Optical examination of the <100 μm thick flattened and embedded tracks with high numerical aperture objectives in a compound microscope was needed to locate and map the presence of large (>1 μm) transparent grains (typically silicates) and opaque minerals such as sulfides. Typically, terminal particles were extracted first (when available) followed successively by other large mineral grains moving up the track toward the entrance hole. All fragments were embedded in $\sim$1 cm high acrylic resin cylinders after removal from their flattened parent tracks by cutting in strips, typically orthogonal to the track axis. Several mesas, cut to successively smaller sizes around the embedded fragment(s), were produced with the topmost mesa 100–200 μm in size. The upper mesa and its included fragment(s) were microtomed with a 45° diamond knife on a Leica Ultracut S ultramicrotome into sections approximately 70–100 nm thick. Microtome sections were placed onto commercially prepared 200-mesh Cu or Au TEM grids coated with 10nm-thick carbon films. See Matrajt and Brownlee (2006) for additional details of the embedding process and sample preparation techniques.

The microtome sections were studied using a Tecnai 200 keV field-emission TEM equipped with bright-field (BF) and dark-field (DF) CCD cameras and secondary electron (SE) and high angle annular dark field (HAADF) STEM detectors. High-resolution lattice fringe images and selected area electron diffraction patterns were used to measure atomic spacings in individual minerals. The measured *d*-spacings and their associated angles obtained from the diffraction patterns were compared with X-ray diffraction data (XRD) from the JCPDS Mineral Powder Diffraction File Data Book (Bayliss et al. 1980) to confirm mineral atomic structures. Atomic spacings from well-known mineral standards were used for calibration of the high-resolution TEM images. Ring patterns from an evaporated Al-thin film were used for calibration of camera lengths for electron diffraction patterns. Estimated errors are typically less than 5% for both the high-resolution TEM images and the electron diffraction patterns. Angular measurements between reflections in the diffraction patterns have errors of less than 2°.

Energy dispersive X-ray (EDX) spectra were obtained from samples that were placed in a low background beryllium sample holder with double-tilt capability. An EDAX light element X-ray detector and Genesis analysis system were used to obtain and quantify all EDX spectra.

To reduce volatilization and minimize electron beam damage, broad beam techniques consisting of condensing the beam to no less than 50–100 nm in diameter in conventional TEM mode along with a reduction in electron beam current were employed during acquisition of EDX spectra rather than using the scanning transmission electron microscopy (STEM) mode, which produces high current densities capable of sample damage. Olivines, pyroxenes, and sulfides were generally quite robust during analyses showing little to no effects from electron beam exposure; however, extra care was required when analyzing feldspars and silicate glasses, which were susceptible to irradiation damage. Fitting and background subtraction routines using EDAX Genesis algorithms were employed to measure peak integrals. EDX spectral quantification was performed by the k-factor element ratio technique (Cliff and Lorimer 1975). Si-normalized k-factors for O, Mg, Ca, and Fe were measured using a NIST SRM 2063a thin-film standard, and mineral standards were used for all other elements. Spectral energy calibration was performed using a Cu and Al thin-film prepared at the University of Washington. Estimated relative errors for the major elements are typically less than 5%. For the minor elements, relative errors are much higher due to poorer counting statistics and higher sensitivities to background fits. Prior to quantification, we inspected most spectra for proper background fitting and manually adjusted the background fit, if necessary. We estimate that most minor element errors are less than 25–30% except in spectra where minor elements fell under overlapping peaks (such as $Cr_{K\beta}$ overlapping $Mn_{K\alpha}$) where the relative errors were higher. Typical measured detection limits were ~0.1 wt%. A similar detection limit was calculated from a theoretical analysis using the minimum mass fraction relation given in Joy et al. (1986).

To complement TEM studies, we observed the potted butts of some of the fragments with backscatter electrons (BSE) at 10 keV on a JEOL JSM 7000F field emission scanning electron microscope (FESEM) located in the Materials Science and Engineering department at the University of Washington. To minimize damage to the SD samples and the acrylic resin, which is susceptible to shrinkage under the electron beam, BSE images were collected at low electron doses and with minimal beam exposure time. The minerals in the potted butts were qualitatively confirmed with an attached EDX detector.

TRACK DESCRIPTIONS

Track Nomenclature

A total of 16 tracks were examined during this study with the emphasis placed on obtaining petrographic relationships and mineralogical identifications of the large (> 1 μm) grains. In many tracks, the distribution of grains (Fig. 1) was often complex; the nature and distribution of these grains were an important part of this study. To minimize terminology confusion, we briefly define terms and present our naming scheme used in this article. We use the term "terminal particle" to refer to the solid grain (fragment) that is present at the terminus of the longest track. In some cases, fragments were present at the termini of slightly shorter tracks that were sub-parallel to the main track containing the terminal particle. We refer to these fragments as "sub-terminal" particles. No special term is used to designate fragments that were present at the ends of very short side tracks. In general, we use the term "fragment" to refer to any coarse particle present in a track including terminal and sub-terminal particles. Fragments could be single mineral grains such as olivine or Fe-Ni sulfide or mixed assemblages of more than one mineral species (rocks). Different fragments from a given track may have been, but were not necessarily, genetically related.

Many tracks contain discrete impact-produced melted grains, which are observed either isolated in the tracks or surrounding large mineral fragments. We have observed three compositional types: (1) grains/regions composed of pure SiO_2, which were produced simply by melting of silica aerogel, (2) grains/regions composed of nanophase Fe,Ni metal beads with Fe sulfide rims in Mg-free silicate glass, and (3) grains/regions composed of nanophase Fe,Ni metal beads with Fe sulfide rims in Mg-bearing silicate glass. We refer to this last type of material as MSG (Metal and Sulfide in Glass), which occurs in discrete grains up to several microns in size or more and often partially or completely surrounds coarse fragments (Fig. 2). MSG was formed by melting and mixing of Fe-Ni sulfides and Mg-silicates from the impacting particles and silica aerogel. Often, the Mg-bearing silicate glass in MSG contains other elements including Al and Ca. Materials in the tracks with the nanophase metal beads with sulfide rims, whose glasses were free of Mg (number 2 above), were probably formed by mixing and melting of Fe-sulfides (Ishii et al. 2008) and silica aerogel, without Mg-silicates. When referring to MSG in this article, we do not include this latter material as MSG. Our observations suggest that it is not volumetrically abundant compared with MSG. Extensive studies and discussions of these materials can be found in Leroux et al. (2008b), Stodolna et al. (2009), Roskosz et al. (2008), Trigo-Rodríguez et al. (2008) and Velbel and Harvey (2009).

Sample numbers were given to each track during preliminary examination at the NASA-JSC curatorial facility. In addition, we gave nicknames to each track, typically from gods or goddesses, which we use throughout. The abbreviated track numbers and their

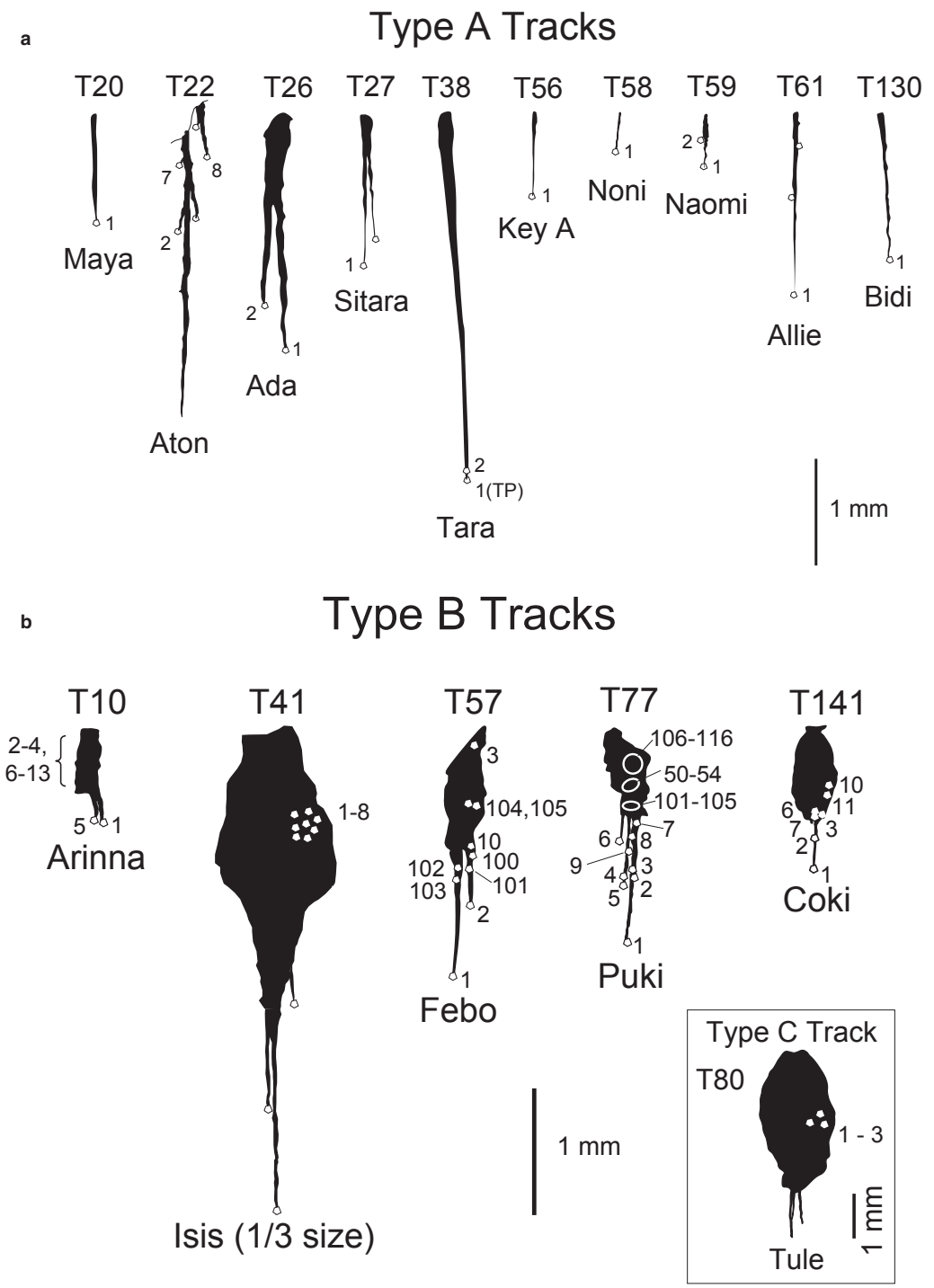

Fig. 1. Scaled cross-sectional profiles of all 16 tracks studied. Profiles were obtained from optical images from flattened tracks. Small nonfilled outlined shapes represent locations of terminal particles and other large fragments studied. Numbers correlate with fragment numbers in Table 2. Unnumbered outlined shapes represent locations of large fragments that were present in the tracks, but not studied. On some track profiles, unstudied large fragments are not shown. a) Ten type A tracks studied by TEM and FESEM. Top portions of tracks 22 and 26 were not available for study. Small track present at the top of Aton is the lower portion of a small root extending from the upper portion of the track. b) Outlines of five bulbous type B tracks and one type C track (inset). Circular regions shown in the interior of track 77 give locations where multiple fragments were studied. The upper portions of tracks 57 and 77 were not available for examination. Terminal particle from Isis was removed from track prior to this study. Track 41, which is 11-mm long, is scaled to 1/3 of actual length. In Tule, the single type C track in this study, only three fragments in the bulbous portion of the track were observed. Track types A, B, and C classification after Hörz et al. (2006) and Burchell et al. (2008).

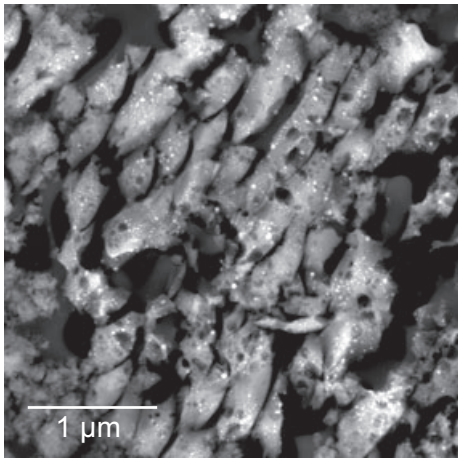

Fig. 2. HAADF image of the interior of a >10 μm grain of silicate glass with inclusions of nanophase metal and Fe-sulfides in track 41. We use the acronym MSG (metal and sulfide in glass) to refer to this material, which is ubiquitous in the type B and C tracks and generally absent in type A tracks.

corresponding University of Washington track names are listed in Table 1, columns 1 and 2, respectively. The full NASA name is given in column 3 and corresponds to the name listed on the NASA Stardust catalog homepage: curator.jsc.nasa.gov/stardust/sample catalog/index.cfm.

As many tracks contain one or more large minerals or rock fragments, the naming scheme of individual fragments and terminal particles can be complex. We named each fragment or terminal particle based on parent track number or name followed by a fragment number, such as Tack 141 – fragment 2 (or Coki – fragment 2). For terminal particles, we often use the terminology "TP," but these also have fragment numbers, typically "fragment 1." Thus, the terminal particle from track 141 (Coki) is labeled Coki – fragment 1 or track 141 – fragment 1 or track 141 – TP(1). Table 2 can be used to cross-reference terminal particles with fragment numbers.

Track Morphology

Names, track numbers, TP mineralogy, and physical properties of the tracks are listed in Table 1 for the 16 tracks in this study. Terminal particles were not present in three keystones allocated to us because they had previously been removed. Terminal particle mineralogy was determined from the literature for tracks 22 and 41

Table 1. Numbers, track names, track lengths, track types, mineralogy, apparent sizes of TPs, and other characteristics of 16 SD tracks.

Track no.	UW name	NASA JSC name	Track length (mm)	Type[a]	TP mineralogy	TP apparent size (μm)	Estimated impactor size (μm)	Comments
20	Maya	C2115,22,20	0.9	A	En_{100}	5	9	TP shocked?
22	Aton	C2115,24,22	3.9	A	$Fo_{64–93}$ + Diop + Al-sil gls[b]	6	14	Upper track not studied
26	Ada	C2054,5,26	>2	A	Fay/tridymite	17	–	Upper track missing
27	Sitara	C2054,5,27	1.3	A	$En_{79–83}$, Ko-aug, Pent, Pyrr	8	9	Two long roots
38	Tara	C2044,0,38	3.2	A	Fe,Ni metal	2	9	Fe oxide on metal
56	KeyA	C2009,1,56	0.65	A	Roed + Ko-aug + En	3	9	Competent TP
58	Noni	C2009,3,58	0.29	A	Fe-oxide + Ni-oxide + Kool grn	5	8	Smallest track
59	Naomi	C2009,4,59	0.35	A	Pent + Pyrr + Hzlwd + SiO_2 gls	3	7	Fe-sulf + SiO_2 gls
61	Allie	C2009,6,61	1.6	A	Al-sil gls, Fo_{99}	5	10	Only TP studied
130	Bidi	C2061,3,130	1.3	A	Fo_{97}, Aug, An	5	9	Probable Al-rich chond
10	Arinna	C2,7,10	~0.5	B	Pyrr + Sph + Pent	3	–	Track flattened axially
41	Isis	C2044,0,41	11	B	Fe,Ni metal[c]	–	–	Largest track studied
57	Febo	C2009,2,57	>1.4	B	Pyrr + Fo_{97} + En_{98}	8	–	Upper track missing
77	Puki	C2009,20,77	>1.2	B	Kool grn	6	–	Upper track missing
141	Coki	C2061,3,141	0.94	B	Pent + Pyrr + Sph	5	–	Presolar SiC present[d]
80	Tule	C2092,3,80	4.7	C	?	–	–	TP not studied

An = anorthite, Aug = augite, En = enstatite, Fay = fayalite, Fo = forsterite, gls = glass, Hzlwd = heazlewoodite, Ko = kosmochloric, Pent = pentlandite, Pyrr = pyrrhotite, Sph = sphalerite, Roed = roedderite, SiC = silicon carbide, sil = silicate, Diop = diopside, TP = terminal particle, grn = grain.

[a]Hörz et al. (2006), Burchell et al. (2008).

[b]TP mineralogy from Tomeoka et al. (2008).

[c]TP mineralogy from Ogliore et al. (2010).

[d]Messenger et al. (2009).

Table 2. Mineralogy of 87 Wild 2 fragments and estimated MSG abundances in 16 Stardust tracks.

Track number	UW name	Track type	Fragment number	Fragment minerals and rocks		Estimated MSG in track
				Major	Minor	
10	Arinna	B	1(TP)	Pyrr + Sph		Abundant
			2	Pyrr + Pent + Sph		
			3	Kam	Kool grain	
			4,5,6	$Fo_{98–99.4}$	Fe-oxide	
			7,9	Pyrrhotite		
			8	Plag(An_{64}, An_{75})?	Pyrrhotite	
			10	Kool grain		
			11	Fo_{83} + Spnl		
			12	$En_{99.8}$		
			13	Pyrr + Pent		
20	Maya	A	1(TP)	En_{100}		Absent
22	Aton	A	2	Cmpr aero		Absent
			7	$Fo_{67–92}$ + Alb gls		
			8	$Fo_{67–91}$ + Al,Mg gls		
26	Ada	A	1(TP)	Fay + Trid	Chr, Cub	Low
			2	Fay + Trid		
27	Sitara	A	1(TP)	Low-Ca Px + Pent + Pyrr + Ko-aug		Low or absent
38	Tara	A	1(TP)	Taen	Fe-oxide	Abundant
			2	Bulk glass		
41	Isis	B	1	En_{100}	Fo_{100}, silica veins	Abundant
			2	Fo_{92}		
			3	Kool grain		
			4	Crystalline SiO_2		
			5	En_{96}		
			6	$Fo_{79–85}$		
			7	Fo_{89} + alb + Fe-sulf		
			8	LIME Fo		
			9	Bulk glass		
56	Key A	A	1(TP)	Roed + Ko-aug + En + Na,K sil gls	Fe-sulf, Chr	Low
57	Febo	B	1(TP)	Pyrr + Fo_{97} + En_{98} + fg chond.	Mn,Cr Fe-sulf, Na sil gls	Moderate
			2	Pyrr + fg chond		
			3	$Fo_{97–98}$		
			10	Fo_{98}		
			100	En_{98}		
			101	LIME Fo		
			102	Fo_{93} + High-Ca Px(?)		
			103	$Fo_{81–84}$ + $En_{87–89}$ + Mg,Al, Ca,Fe sil gls		
			104	LIME Fo		
			105	En_{98}		
			120	Kam		
58	Noni	A	1(TP)	Hem + Trev + Bun + $Fo_{88–93}$ + Ko-aug + Mg,Al sil gls		Absent
59	Naomi	A	1(TP)	Pent + pyrr + Hzlwd + SiO_2 gls		Absent
			2	Pent + pyrr + Hzlwd + SiO_2 gls		
61	Allie	A	1(TP)	Al-rich sil gls + Fo_{99} + Taen	Fe-oxide	Absent

Table 2. *Continued*. Mineralogy of 87 Wild 2 fragments and estimated MSG abundances in 16 Stardust tracks.

Track number	UW name	Track type	Fragment number	Fragment minerals and rocks: Major	Fragment minerals and rocks: Minor	Estimated MSG in track
77	Puki	B	1(TP)	$Fo_{62–67}$		Moderate
			2	$Fo_{59–60}$ + Kam		
			3	Fo_{52}		
			4	$Fo_{53–61}$		
			5	Kool grain		
			6	LIME Fo		
			7	$Fo_{61–70}$ + Na,Mg,Al,Fe sil gls		
			8	Pyrr		
			9	Mn-rich Augite		
			50	LIME Fo		
			51	Pyrr		
			52	Kool grain		
			53	Fo_{97}	Ko-diopside	
			54	Fo_{100}	Schr, Fo_{97}	
			102	Kool grain	Cr-Spn, Schr	
			103	Fo_{98}	High sil gls, Mg,Al Chr	
			104	LIME Fo	Pent, Fo_{99}, Al sil gls	
			105	Fo_{66}		
			106	Albite		
			107	Fo_{64}		
			108	$En_{99.8}$		
			109	Fo_{91}		
			110	Ko-augite		
			111	En_{95}		
			112	En_{95}		
			113	Kool grain		
			114	$Fo_{86–90}$		
			115	$Fo_{63–67}$		
			116	Fo_{76}		
80	Tule	C	1	Al-diop + Augite + En_{99}	Mn > Fe in En_{99}	Abundant
			2	$En_{99.6}$	Na,Al,K,Cr,Mn sil gls	
			3	$Fo_{41–43}$	Mg,Al,Fe sil gls	
130	Bidi	A	1(TP)	Augite + Fo_{97} + Anorthite	SiO_2 lam in anorth	Absent
141	Coki	B	1(TP)	Pyrr + Pent + Sph + Fo_{79}		Abundant
			2	Fass + Anorth	Kool grain	
			3	Kool grain	Spnl, V + Nb incl	
			6	En_{99}	Chr incl in Oliv	
			7	En_{99}	Pent	
			10	Kool grain		
			11	LIME Fo		

MSG = Metal and sulfides in glass (see text), 1(TP) = terminal particle(fragment 1), Pyrr = pyrrhotite, Sph = sphalerite, Pent = pentlandite, Fo = forsterite, Plag = plagioclase, An = anorthite, Spnl = spinel, En = enstatite, Cmpr aero = compressed aerogel, Alb = albite, gls = glass, Fay = fayalite, Trid = tridymite, Px = pyroxene, Ko-aug = kosmochloric augite, Taen = taenite, sulf = sulfide, Roed = roedderite, sil gls = silicate glass, Chr = chromite, fg chond = fine-grained chondritic material, Kam = kamacite, Hem = hematite, Trev = trevorite, Bun = bunsenite, Hzlwd = heazlewoodite, Amorh = amorphous, Cub = cubanite.

(see Table 1 for references). The minerals located at the ends of the small roots in track 80 remain unknown. Hörz et al. (2006) classified Stardust tracks into three categories depending on the shapes of their cross-sectional profiles. Carrot-shaped type A tracks have monotonically decreasing widths from their entry holes from the top of the track to the terminal particle and are typically thin. These tracks were formed by competent impactors, such as single mineral grains or solid compact rocks, that did not disaggregate or disaggregated minimally during collection in the aerogel. In this study, 10 tracks are classified as type A (Table 1, Fig. 1a). All have width/length ratios $< \sim 0.1$ consistent with type A tracks in Burchell et al. (2008). Tracks composed of

wide, generally distinct, bulbous regions below their entry holes that contain terminal particles in styli below the bulb regions are type B tracks (Table 1, Fig. 1b). These tracks often contain numerous widely dispersed minerals, rock fragments, and MSG, and were probably produced by complex assemblages of coarse- and possibly fine-grained components. Five tracks in this study, which have length/width ratios from 0.15 to 0.31 are type B tracks (Burchell et al. 2008). Type C tracks (Table 1, Fig. 1b) are the most bulbous, and do not contain prominent roots with terminal particles. We examined fragments from a single type C track.

Track lengths varied from 290 μm to 3.9 mm in type A tracks, from ~500 μm to ~11 mm in type B tracks, and 4.7 mm for the single type C track (Table 1, Fig. 1). Apparent TP sizes ranged from 2 to 17 μm for the type A tracks and from 3 to 8 μm for the type B tracks (Table 1). Locations of fragments and their associated numbers, which are discussed throughout the text, are given for each track in Fig. 1. A few fragments are shown in the cross-sectional profiles, but are unlabeled; these correspond to fragments that are still present in the tracks but have not yet been studied. In some of the type B tracks, numerous fragments were extracted from volumetrically small regions; thus, these are shown as clusters or by circled regions with their corresponding fragment numbers listed nearby (Fig. 1).

Masses of Type A Impactors

Using the calibration curve of track volume versus kinetic energy from Burchell et al. (2008), we estimated the masses of the impactors from all ten type A tracks. Track volumes were calculated using our measured track lengths and equation 17 from the Burchell et al. (2008) study. From the volume measurements, impact kinetic energies were calculated using equation 12. Our excavated track volumes fell just slightly off the end of the calibration curve and a slight amount of extrapolation to lower volumes was required. Once the impact kinetic energies were determined for each track, we used the K.E. = 0.5(mass) $(\text{velocity})^2$ relation to calculate impact particle masses. The procedure gave Wild 2 particle masses ranging from 1.0 to 4.8 ng for the 10 type A impactors. As we know the approximate mineral modes and compositions of the impactors (assumed equivalent to the TP particles), we further calculated densities of the impactors (assuming no porosity) to determine equivalent spherical diameters. These results produced diameters for the type A impactors ranging from 7 and 14 μm (Table 1). As the upper portion of track 26 was missing and we did not know its true length, the calculated impactor size of 11 μm was clearly much too low (the TP has an apparent size of 17 μm); thus; we do not provide an estimated impactor size in Table 1 for this track.

MODIFICATION DURING CAPTURE

An important consideration regarding the collection of Wild 2 particles concerns the degree of modification that impacting grains experienced during capture in aerogel. A major difference between bulbous (type B and C) tracks and narrow (type A) tracks relates to the way that energy was deposited during track formation. Tracks with a large bulbous upper cavity had a larger proportion of their projectile's kinetic energy dissipated in this region. The bulbous regions of tracks are voids produced by combined melting and compression of silica aerogel, products of high power generation during particle deceleration. Enhanced power generation and enhanced aerogel melting in the upper regions of bulbous tracks appear to be caused by the presence of small components that decelerate more quickly and deposit their energy higher in the track than larger more deeply penetrating components. One consequence of this is the proportionately higher abundance of melted aerogel in the upper portions of type B and C tracks. Although erosion and melting of the surfaces of larger grains (silicates + sulfides) followed by mixing with silica aerogel melt would be expected to produce MSG material (see Ishii et al. [2008] for a discussion of MSG-like material produced from pyrrhotite), loosely bound fine-grained components present in the original impactor would be most susceptible to modification and production of MSG. Some bulbous tracks could have been produced by single anhydrous mineral projectiles such as pyrrhotite (see Kearsley et al. 2012).

Type A tracks are thin cones and their terminal particles indicate that they are made by competent, weakly fragmenting projectiles. Bulbous tracks are made by fragmenting projectiles and they could have formed in two major ways: (1) from solid projectiles that fractured into many pieces or were otherwise unstable during capture or (2) from fragmentation of aggregates composed of both fine and coarse components. Some bulbous tracks were probably made by projectiles such as fractured chondrule fragments, but we believe that most of the bulbous tracks were formed by aggregates of unrelated components. Like common IDPs and many primitive chondrites, Wild 2 is an aggregation of heterogeneous materials that range in size from the submicron to solid components larger than 100 μm (Tuzzolino et al. 2004; Hörz et al. 2006; Zolensky et al. 2008; Price et al. 2010). The stresses of capture separate the components and the smaller ones stop quickly and generate the bulbous cavities. Our track observations are

consistent with this model and the scenario that comet dust contains weakly adhering fine components is consistent with infrared spectroscopy of comets and the dust impact measurements made by Stardust's dust flux monitor instrument (DFMI) (Green et al. 2004, 2007). The presence of a 10 μm silicate feature in comet IR observations of comets requires the presence of submicron silicates (Hanner and Zolensky 2010) that must have been most delicately attached to larger components, otherwise they could not have been liberated to become free grains. The remarkable pulsed nature of DFMI dust flux measurements at Wild 2, and later at comet Tempel 1, were interpreted as the in-coma break up of highly fragile dust clods (Green et al. 2007). The disintegration of weak particles was also dramatically observed by the EPOXI mission flyby of comet Hartley 2 (A'Hearn 2011). Thus, we believe that an aggregate nature of Wild 2 can explain most of the aerogel collection tracks, and the range of type A to type C tracks reflects the mix of coarse (larger than ~1 or 2 μm) and fine components with type C tracks being notable because of their low content of coarse components.

DETAILED TRACK MINERALOGY

Table 2 provides a summary of the mineralogy of the fragments from each track that we studied. All major minerals and bulk glasses as well as all minor minerals that were deemed primary (not produced by collection in silica aerogel) are given in columns 5 and 6. In addition, estimates of the degree of MSG abundance in each track are provided. The estimates were obtained simply from optical examination of flattened tracks, microtome sections, and potted butts, as well as TEM observations of microtome slices. In this section, we provide mineralogical details, largely from TEM examination, of the coarse fragments in each track. We describe each of the 16 tracks in detail, and the discussion and synthesis will be at the end of the article.

Track 10 (Arinna)

Track 10 is a type B track containing a large cavity laterally offset above two roots of nearly similar length (Fig. 1b). The track was in a small irregular aerogel fragment that was dislodged from its original aerogel cell and found loose in the collector. Unlike other tracks, track 10 was flattened in its long direction before embedding in acrylic. The lower portion of the track showed a "vapor trail" of fine sulfide beads leading to the terminal particle. We studied 13 distinct fragments along the track including olivines, pyroxenes, and sulfides. An optically opaque terminal particle (fragment 1) at the terminus of the longer root is a >2 μm polycrystalline Fe-Ni sulfide dominated by pyrrhotite (Fig. 3a) with variable Ni content (Table 5, ref 255). On one end of the fragment, we observed a 0.5 μm-wide Fe-Zn sulfide, probably sphalerite, with Zn/(Fe + Zn) = 0.49 (atomic). This phase is in sharp contact with the pyrrhotite (Fig. 3a) suggesting mutual growth of these two minerals. EDX measurements indicate up to 2.5 wt% Mn is present in the sphalerite (Table 5, ref 256). An assemblage of submicron FeO-rich olivine ($Fo_{88–93}$) and kosmochloric augite (Ko-augite), a Na + Cr-rich high-Ca pyroxene, is attached at the opposite end of the pyrrhotite. These latter phases are part of an assemblage called a Kool grain (Kool = kosmochloric high-Ca pyroxene + FeO-rich olivine) and are observed isolated or attached to fragments elsewhere in the track and in other tracks (Joswiak et al. 2009). We found a number of additional large sulfide fragments (fragments 2, 7, 9, and 13) (Figs. 3b–e), but do not have specific track locations for them. Ni concentrations of the pyrrhotites from these fragments vary from below detection limits to above 5 wt%. Most sulfide fragments were free or nearly free of aerogel melt and MSG. Pentlandite was observed in fragments 2, 9, and 13 (Table 5, ref 266), modally varying from minor in fragments 9 and 13 to comprising approximately one-third of the microtome section of fragment 2. Most of the sulfide fragments have partial to complete rounded shapes indicative of surface abrasion during capture. The various sulfide fragments may have been part of a much larger sulfide grain in the original impactor that was composed of pyrrhotite + sphalerite + pentlandite, which disaggregated into smaller pieces during aerogel capture. We have observed similar three-sulfide assemblages in IDPs as well as in track 141 (see below). Microtome sections of the TP from track 10 were studied by Berger et al. (2008) who concluded that the pyrrhotite and sphalerite were part of a nonequilibrium assemblage that formed at a temperature of <340°C. In the Berger et al. (2008) study, superstructure reflections in the pyrrhotite imaged in electron diffraction patterns were suggestive of low temperature formation. One implication of this result is that the sulfide fragment may have links to phyllosilicate-bearing materials as these low temperature minerals are commonly associated with hydrated phases in unequilibrated chondrites. A second implication is that the fragment was not subjected to flash heating at high enough temperatures for a long enough duration during capture to have been thermally modified to more stable high temperature phases.

A large fragment (fragment 5; Fig. 3j) present at the terminus of the shorter root (Fig. 1b) was found to be MgO-rich olivine ($Fo_{98.8}$). EDX measurements show that

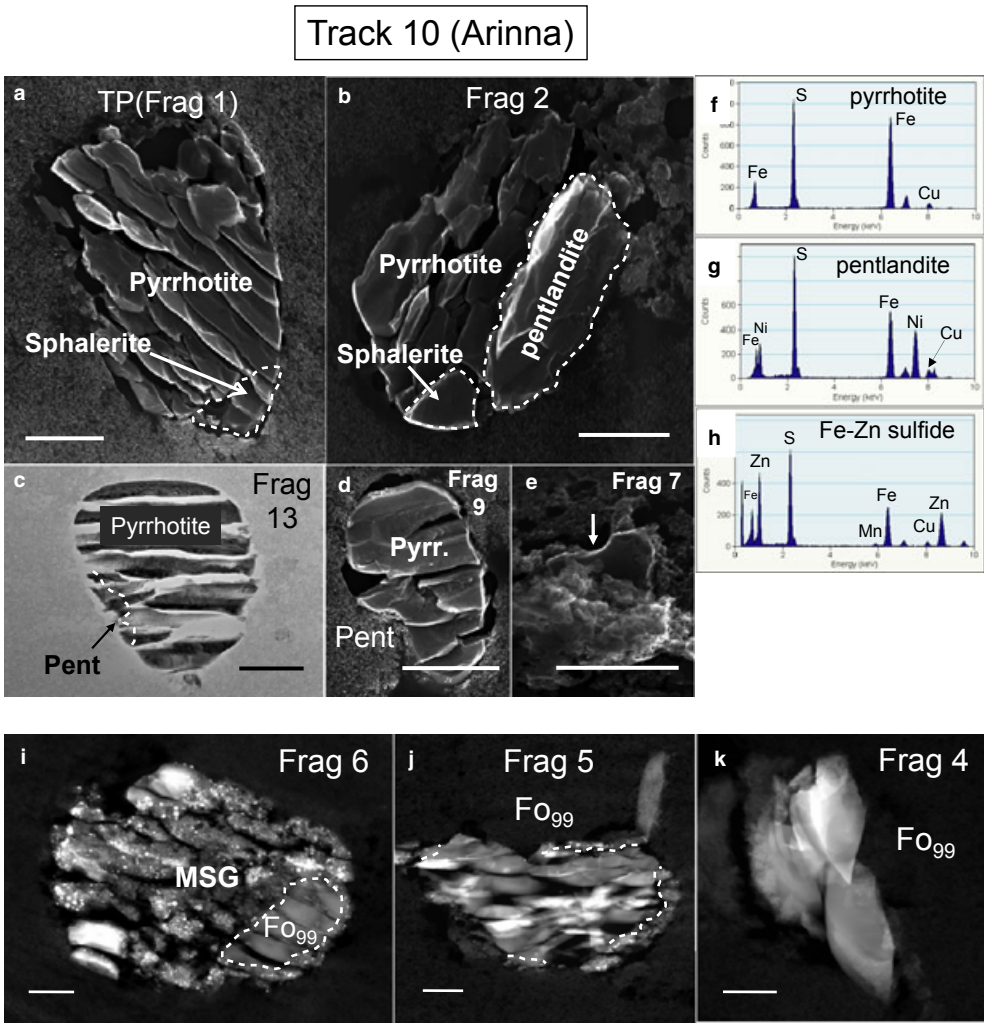

Fig. 3. TEM images of microtome slices of Fe-sulfide and forsterite fragments observed in track 10 (Arinna). a) SE image of terminal particle (frag 1). The fragment is largely composed of pyrrhotite with a small tip of Fe-rich Zn-sulfide, probably sphalerite (dotted region). b) SE image of fragment 2 showing three-sulfide assemblage of pyrrhotite + pentlandite + sphalerite. c) BF image of rounded fragment 13 composed of pyrrhotite with a sliver of pentlandite on lower left-hand side. d) SE image of fragment 9 composed of pyrrhotite with a small amount of pentlandite. e) SE image of pyrrhotite (fragment 7) protruding above aerogel. Compressed aerogel is present above the fragment on the lower side. The curved grain boundary indicated by the arrow may indicate attachment to another fragment prior to capture in aerogel. f–g) Typical EDX spectra of the Fe-sulfide phases shown in (a)–(e). Cu peaks are system peaks. The pyrrhotite fragments are somewhat variable in Ni, although most analyses showed only minor to no measurable Ni abundances. i–j) HAADF images of microtome slices of three forsterite fragments (frags 4, 5, and 6) observed in the track. Dotted lines in (i) and (j) show contacts between the olivine and attached MSG. All scale bars = 0.5 μm.

it is relatively homogeneous in Fe and Mg and contains moderate amounts of Al_2O_3 (0.20 wt%) and CaO (0.27 wt%), high Cr_2O_3 (0.71 wt%), but is low in MnO (< 0.1 wt%) (Table 3, ref 481). Various olivine fragments of similar composition were found in other locations in the track (fragments 4 and 6; Figs. 3k and 3i) indicating possible fragmentation of a larger olivine during collection in aerogel. Significant amounts of MSG were associated with the olivine and are present as rims and as attached bulk material. Unfortunately, due to the axial compression of the track during preparation for ultramicrotomy, it is unknown what the exact locations of the fragments were, except for the TP (fragment 1) and sub-terminal particle (fragment 5).

A 0.6 μm Kool grain (fragment 10, not shown), believed to be from the bulb region of the track, consists of numerous subhedral crystals of FeO-bearing olivine, kosmochloric, augite and aluminosilicate glass. The fragment has an igneous texture similar to some porphyritic igneous rocks. See Joswiak et al. (2009) for additional details regarding this fragment. Other fragments that were found in the track, but not studied

Table 3. Representative chemical compositions of Wild 2 olivines (normalized oxide wt%).

Track #	10	22	22	25	41	41	41	57	57	57	61	77	77
Name	Arinna	Aton center	Aton rim	Ada	Isis	Isis	Isis	Febo	Febo	Febo	Allie	Puki	Puki
Frag	5	7	7	1(TP)	8	2	3	1(TP)	3	103	1(TP)	1(TP)	5
Ref	481	142[a]	141	187	161	345	159[c]	172	193	570	561	122	402[d]
SiO_2	44.51	35.72	36.79	28.59	42.27	40.38	36.55	41.08	41.00	39.60	42.70	37.36	37.93
Al_2O_3	0.20	0.15	0.25	0.50	0.34	0.08	0.16	0.11	0.17	b.d.	0.41	0.15	0.06
Cr_2O_3	0.71	0.10	0.14	0.27	0.26	0.44	b.d.	0.34	0.41	0.15	0.07	0.08	0.02
FeO	1.19	28.02	17.73	62.23	0.24	7.76	27.02	3.31	2.98	15.29	1.08	27.47	29.22
MnO	0.08	0.89	0.76	6.58	0.64	0.34	0.72	1.09	0.78	0.51	0.10	0.42	0.66
MgO	53.03	34.17	43.52	1.29	56.18	50.74	34.76	53.92	54.62	44.26	55.64	34.31	31.45
CaO	0.27	0.31	0.27	0.03	0.04	0.26	0.17	0.15	0.05	0.19	b.d.	0.21	0.26
P_2O_5	b.d.	b.d.	0.54	0.52	0.04	b.d.	0.23	b.d.	b.d.	b.d.	b.d.	b.d	0.29
Cation formulas based on 4 oxygens													
Si	1.043	0.970	0.944	0.961	0.994	0.984	0.981	0.984	0.980	0.998	1.004	0.998	1.021
Al	0.006	0.005	0.007	0.020	0.009	0.002	0.005	0.003	0.005	0.000	0.011	0.005	0.002
Cr	0.013	0.002	0.003	0.007	0.005	0.008	0.000	0.006	0.008	0.003	0.001	0.002	0.000
Fe	0.023	0.636	0.380	1.748	0.005	0.158	0.606	0.066	0.060	0.322	0.021	0.613	0.658
Mn	0.002	0.020	0.017	0.187	0.013	0.007	0.016	0.022	0.016	0.011	0.002	0.010	0.015
Mg	1.853	1.383	1.664	0.065	1.970	1.844	1.390	1.926	1.946	1.662	1.950	1.366	1.263
Ca	0.007	0.009	0.007	0.001	0.001	0.007	0.005	0.004	0.001	0.005	0.000	0.006	0.007
P	0.000	0.000	0.012	0.015	0.001	0.000	0.005	0.000	0.000	0.000	0.000	0.000	0.003
Total	2.947	3.026	3.034	3.004	2.997	3.010	3.009	3.011	3.014	3.001	2.990	2.999	2.970
Fa	1.2	31.5	18.6	96.4[b]	0.2	7.9	30.4	3.3	3.0	16.2	1.1	31.0	34.3

Track	77	77	77	77	80	130	141	141	141
Name	Puki	Puki	Puki	Puki	Tule	Bidi	Coki	Coki	Coki
Frag	2	3	4	50	3	1(TP)	1(TP)	3	11
Ref	554	254[e]	704	485	200	374	547	313	710
SiO_2	37.26	33.90	36.93	41.54	32.18	42.93	40.33	36.76	42.43
Al_2O_3	0.34	b.d.	b.d.	0.12	b.d.	0.20	0.18	0.57	b.d.
Cr_2O_3	0.27	0.14	0.18	0.31	0.27	0.53	b.d.	b.d.	0.24
FeO	32.49	37.61	33.86	0.18	46.96	1.88	18.73	16.19	0.14
MnO	0.80	0.64	0.73	0.46	0.71	0.17	0.62	0.53	0.50
MgO	28.48	26.93	27.89	57.37	19.55	54.07	39.97	45.90	56.67
CaO	0.36	0.61	0.42	0.03	0.32	0.23	0.17	0.04	0.03
P_2O_5	b.d.	b.d.	b.d.	b.d.	b.d.	b.d.	b.d.	b.d.	b.d.
Cation formulas based on 4 oxygens									
Si	1.020	0.962	1.019	0.979	0.960	1.014	1.028	0.937	0.997
Al	0.011	0.000	0.000	0.003	0.000	0.005	0.006	0.017	0.000
Cr	0.006	0.003	0.004	0.006	0.006	0.010	0.000	0.000	0.004
Fe	0.744	0.893	0.781	0.003	1.172	0.037	0.399	0.345	0.003
Mn	0.018	0.015	0.017	0.009	0.018	0.003	0.013	0.011	0.010
Mg	1.162	1.140	1.147	2.015	0.870	1.903	1.519	1.743	1.986
Ca	0.011	0.019	0.012	0.001	0.010	0.006	0.005	0.001	0.002
P	0.000	0.000	0.000	0.000	0.000	0.000	0.000	0.000	0.000
Total	2.972	3.032	2.979	3.017	3.036	2.979	2.969	3.055	3.001
Fa	39.0	43.9	40.5	0.2	57.4	1.9	20.8	16.5	0.1

TP = terminal particle, Fa = fayalite, b.d. = below detection

[a]0.6 wt% Na_2O measured but not listed.

[b]Tephroite component included in end-member calculation.

[c]0.39 wt% Na_2O measured but not listed.

[d]0.12 wt% NiO measured but not listed.

[e]0.16 wt% NiO measured but not listed.

in detail, include kamacite (fragment 3), a possible plagioclase feldspar ($\sim An_{64–75}$, fragment 8), Fe + Mg + Al + Cr-rich spinel (associated with FeO-rich olivine; fragment 11), and nearly FeO-free enstatite (fragment 12). Identification of the feldspar is tenuous as the fragment was very unstable under the electron beam and

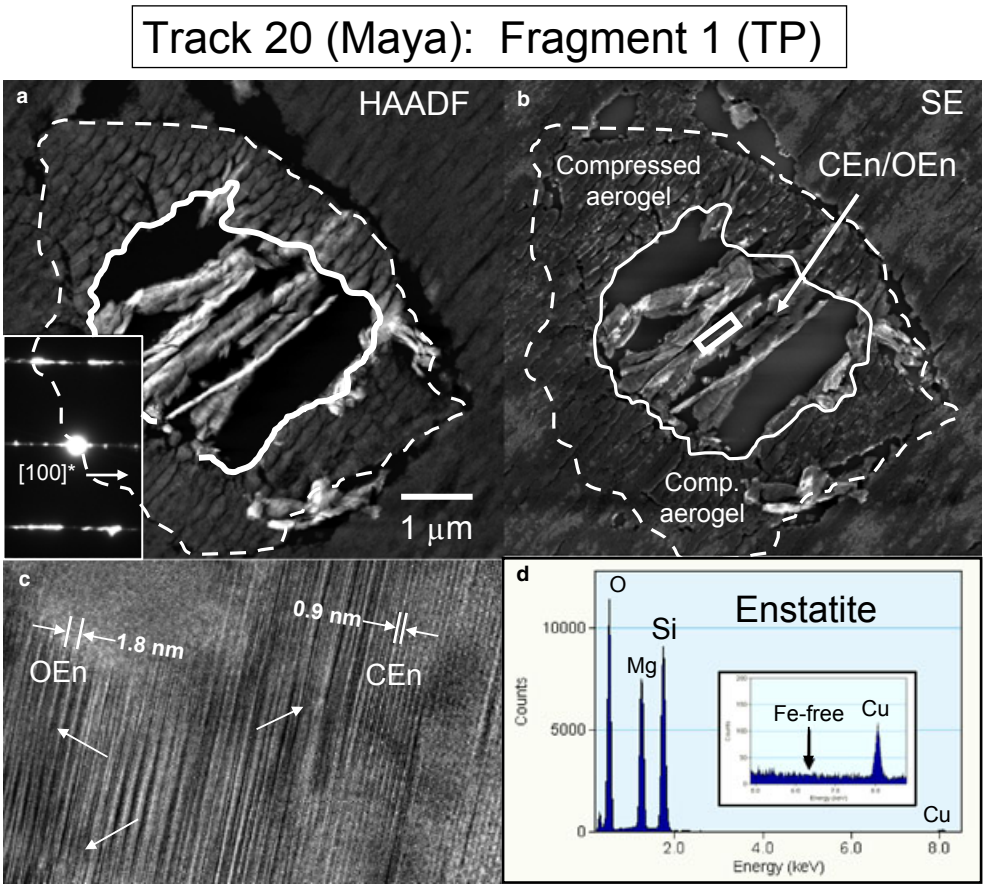

Fig. 4. a) HAADF image of microtomed slice of track 20 terminal particle, an FeO-free enstatite. Solid white line shows outline of grain and plucked regions. Dotted white line defines perimeter of shell of compressed aerogel surrounding fragment. Bright regions in compressed aerogel are shards of terminal particle that were displaced during microtoming. Inset shows streaking in the [100]* direction. b) SE image corresponding to HAADF image in (a). c) High-resolution image taken from interior region of grain showing 0.9 and 1.8 nm lattice fringes corresponding to (100) clinoenstatite and orthoenstatite atomic planes, respectively. Three white arrows indicate regions of stacking faults. d) EDX spectrum taken from outlined rectangular region in (b) showing that Fe is at or below background levels. Inset shows energy region around the $Fe_{K\alpha}$ edge. Cu peak is a system peak. CEn = clinoenstatite, OEn = orthoenstatite.

we could not precisely determine a composition or crystal structure.

In summary, track 10, the shortest type B track in this study, contains a mixture of coarse mineral and rock fragments and significant amounts of MSG. Forsteritic olivines and Fe sulfide fragments consisting of pyrrhotite ± pentlandite ± sphalerite comprise the largest proportions of the coarse grains. Additional coarse fragments observed include Fe,Ni metal, a Kool grain, Fe-poor enstatite, and possibly plagioclase feldspar.

Track 20 (Maya)

Track 20 is a 0.9 mm long type A track (Fig. 1a) whose terminal particle is composed of pure enstatite (Fig. 4). Little to no MSG and no large fragments are present along the track walls indicating the impactor consisted solely of a competent single pyroxene grain. A 1 μm-wide mantle of compressed aerogel surrounds the exterior of the fragment. No observable phases were present in the aerogel mantle. A small amount of Mg-bearing silicate glass, 400 × 100 nm in size was observed in sharp contact in one region on its exterior (not shown).

The composition of the pyroxene is uncharacteristically pure enstatite (En_{100}) (Table 4, ref 186). We were unable to measure the presence of Fe or any other elements in any EDX spectra even after long integration times (Fig. 4d). No inclusions in the pyroxene were observed. Electron diffraction patterns and high-resolution images show that the atomic structure of portions of the pyroxene consists of intergrowths of coexisting clino- and orthoenstatite. These phases are evident from smearing along the [100]* direction in the DP (Fig. 4a inset) and as distinct alternating regions of 1.8 nm

Table 4. Representative chemical compositions of Wild 2 pyroxenes (normalized oxide wt%).

Track #	20	27	27	41	41	41	41	56	56	57	57	58
Name	Maya	Sitara	Sitara	Isis	Isis	Isis	Isis	Key A	Key A	Febo	Febo	Noni
Frag	1 (TP)	1 (TP)	1 (TP)	1 (TP)	1 (TP)	3	5	1 (TP)	1 (TP)	1 (TP)	103	1 (TP)
Ref	186	153	150	357	358	160	592	359	207	170	572	686
SiO_2	61.11	54.94	52.96	57.71	57.10	52.73	58.44	54.60	59.63	56.32	55.45	59.55
TiO_2	b.d	0.36	0.96	b.d.	b.d.	0.56	0.12	0.00	0.52	b.d.	0.21	0.28
Al_2O_3	0.19	0.23	0.62	1.81	1.83	0.79	0.84	0.06	0.30	2.74	1.52	1.33
Cr_2O_3	b.d	0.69	10.28	1.01	0.32	1.84	0.99	7.26	0.49	1.19	1.69	3.00
FeO	b.d	11.44	2.47	0.33	0.51	8.63	2.50	13.60	0.11	1.51	7.48	2.73
MnO	0.02	0.97	0.17	b.d.	b.d.	0.47	1.43	1.73	0.11	0.76	0.47	0.30
MgO	38.57	28.79	12.97	37.01	36.65	15.49	33.88	11.82	38.67	35.05	32.32	15.58
CaO	0.10	3.30	14.01	2.13	3.59	18.38	1.73	7.16	0.16	2.44	0.86	14.95
Na_2O	b.d	0.28	5.54	b.d.	b.d.	1.12	b.d.	2.90	b.d.	b.d.	b.d.	1.90
K_2O	b.d	b.d.	b.d.	b.d.	b.d.	b.d.	b.d.	0.86	b.d.	b.d.	b.d.	b.d.
Cation formulas based on 6 oxygens												
Si	2.035	1.972	2.022	1.950	1.939	1.961	1.998	2.067	1.997	1.924	1.938	2.104
Ti	0.000	0.007	0.019	0.000	0.000	0.016	0.003	0.003	0.013	0.000	0.005	0.008
Al	0.008	0.014	0.019	0.072	0.073	0.035	0.034	0.000	0.012	0.110	0.063	0.055
Cr	0.000	0.020	0.282	0.027	0.009	0.054	0.027	0.196	0.013	0.032	0.047	0.084
Fe	0.000	0.340	0.055	0.009	0.014	0.268	0.071	0.382	0.003	0.043	0.219	0.081
Mn	0.001	0.027	0.007	0.000	0.000	0.015	0.041	0.052	0.003	0.022	0.014	0.009
Mg	1.914	1.531	0.704	1.865	1.855	0.858	1.727	0.737	1.931	1.785	1.684	0.821
Ca	0.004	0.082	0.539	0.077	0.131	0.732	0.063	0.267	0.006	0.089	0.032	0.566
Na	0.000	0.022	0.322	0.000	0.000	0.080	0.000	0.224	0.000	0.000	0.000	0.130
K	0.000	0.002	0.000	0.000	0.000	0.000	0.000	0.036	0.000	0.000	0.000	0.000
Total	3.961	4.016	3.969	4.000	4.020	4.019	3.966	3.962	3.978	4.005	4.002	3.867
Fs	0.0	17.4	4.3	0.5	0.8	14.4	3.8	27.6	0.2	2.2	11.3	5.5
Wo	0.2	4.2	41.5	3.9	6.5	39.4	3.4	19.3	0.3	4.7	1.7	38.6
En	99.8	78.4	54.2	95.6	92.7	46.2	92.8	53.2	99.5	93.1	87.0	55.9

Track/IDP	77	77	77	77	77	80	80	80	130	141	141
Name	Puki	Puki	Puki	Puki	Puki	Tule	Tule	Tule	Bidi	Coki	Coki
Frag	5	9	108	110	112	1	1	2	TP	3	6
Ref	557	477	581	583	592	194[a]	196	204	468	365	290
SiO_2	4.74	55.32	60.43	58.05	56.74	46.20	56.08	59.41	55.12	53.50	57.74
TiO_2	0.36	0.26	b.d.	0.31	0.18	1.18	0.14	b.d.	0.95	0.59	b.d.
Al_2O_3	1.19	4.78	b.d.	1.52	1.24	7.80	0.23	0.22	5.10	1.84	1.14
Cr_2O_3	8.70	2.62	0.14	4.86	0.75	0.04	0.41	0.17	1.65	1.55	0.82
FeO	5.17	1.75	0.20	6.66	3.41	0.06	0.51	0.12	1.59	4.35	1.22
MnO	0.14	7.95	0.09	0.14	0.23	b.d.	0.50	b.d.	b.d.	0.52	0.85
MgO	9.62	22.24	39.10	11.22	36.23	15.41	26.61	39.96	22.13	18.17	36.38
CaO	14.73	3.77	0.04	13.77	1.23	28.62	15.38	0.11	13.47	18.81	1.85
Na_2O	4.74	0.62	b.d.	3.47	b.d.	b.d.	b.d.	b.d.	b.d.	0.68	b.d.
K_2O	b.d.	0.22	b.d.	b.d.	b.d.	b.d.	b.d.	b.d.	b.d.	b.d.	b.d.
Cation formulas based on 6 oxygens											
Si	2.030	1.967	2.019	2.104	1.943	1.703	1.974	1.989	1.930	1.934	1.964
Ti	0.010	0.007	0.000	0.008	0.005	0.033	0.004	0.000	0.025	0.020	0.000
Al	0.052	0.200	0.000	0.065	0.050	0.339	0.010	0.009	0.210	0.061	0.046
Cr	0.254	0.074	0.004	0.139	0.020	0.001	0.011	0.005	0.505	0.047	0.022
Fe	0.159	0.052	0.006	0.202	0.098	0.002	0.015	0.003	0.047	0.136	0.035
Mn	0.004	0.239	0.002	0.004	0.007	0.000	0.015	0.000	0.000	0.016	0.025
Mg	0.529	1.179	1.947	0.606	1.850	0.847	1.396	1.994	1.155	0.995	1.845
Ca	0.582	.144	0.001	0.535	0.045	1.130	0.580	0.004	0.505	0.747	0.067
Na	0.339	0.043	0.000	0.244	0.000	0.000	0.000	0.000	0.000	0.075	0.000
K	0.000	0.010	0.000	0.000	0.000	0.000	0.000	0.000	0.000	0.000	0.000
Total	3.966	3.915	3.979	3.907	4.017	4.070	4.007	4.004	3.917	4.030	4.004

Table 4. *Continued*. Representative chemical compositions of Wild 2 pyroxenes (normalized oxide wt%).

Track/IDP	77	77	77	77	77	80	80	80	130	141	141
Name	Puki	Puki	Puki	Puki	Puki	Tule	Tule	Tule	Bidi	Coki	Coki
Frag	5	9	108	110	112	1	1	2	TP	3	6
Fs	12.5	3.8	0.3	15.0	4.9	0.1	0.8	0.2	2.7	7.1	1.8
Wo	45.8	10.4	0.1	39.8	2.3	57.1	29.1	0.2	29.6	39.6	3.5
En	41.7	85.8	99.6	45.2	92.9	42.8	70.1	99.6	67.7	53.2	94.8

Fs = ferrosilite, Wo = wollastonite, En = enstatite, b.d. = below detection.
[a]0.15 atom% V (V_2O_5 = 0.67 wt%) not shown in table.

orthoenstatite and 0.9 nm clinoenstatite lamellae (Fig. 4c). Domains of pure clinoenstatite were also observed. Numerous crystal defects, believed to be edge dislocations (white arrows, Fig. 4c), are present in the grain. The defects in the high-resolution image are visible in areas of higher diffraction contrast resulting from high localized strain fields.

In summary, track 20 was produced by the impact of a single 9 μm enstatite grain The lack of other large fragments in the track indicates that the pyroxene did not fragment during capture.

Track 22 (Aton)

Track 22 is a 3.9-mm-long type A conical track with at least 5 visible short side tracks extending off the main branch, each of which housed an optically visible particle at its terminus (Fig. 1a). In the entire track network, at least eleven large mineral fragments were present including the terminal particle and fragments at the end of side tracks lodged along the main track wall. Thus, this track was unusual in its large number of coarse fragments compared with the other type A tracks. We studied three fragments from the short side tracks, all of which were located in the middle portion of the track. We did not study the terminal particle because it was not present in the keystone we received. The locations of the three fragments (numbers 2, 7, and 8) that we examined are shown in Fig. 1a.

Fragment 2, located approximately 2.5 mm from the terminal particle location, was present at the end of its own ~0.5-mm-long side track. STEM imaging and EDX analysis show that this fragment is arcuate in shape and approximately 2 × 7 μm in size and composed of nearly pure SiO_2. Its texture is very similar to compressed aerogel that was frequently observed along track walls, and we believe that this fragment is compressed aerogel that was accelerated to high speed and then made its own side track. We did not observe large compressed aerogel fragments at the termini of roots in any other tracks indicating that this process is rare.

A backscatter image of the potted butt of fragment 7 is shown in Fig. 5a. The grain has an apparent size of 4 × 6 μm and is composed of a mixture of FeO-rich olivine and silica-rich glass, which is visible in the figure as dark irregular patches. North-south trending chatter marks, formed during microtoming, are also visible on the grain surface. A prominent compressed aerogel rim can be seen surrounding the fragment. A moat located between the particle and the compressed aerogel rim, which is most prominent on the lower right side, is a result of aerogel/acrylic shrinkage after electron bombardment in the FESEM. An HAADF image of a microtome slice cut approximately 3 microns above the potted butt is shown in Fig. 5b. The microtome section is composed of shards typical of the conchoidal fracturing of silicate minerals from microtoming, but is otherwise relatively complete showing little to no grain plucking. EDX analyses indicate that this fragment is largely composed of FeO-rich olivine of variable compositions ranging from Fo_{67} to Fo_{91}. A 15 point EDX transect across the grain shows variable Fe/Mg ratios, suggesting that the grain may have either oscillatory or reverse zoning (Zolensky et al. 2006). Minor element concentrations of 0.25 wt% Al_2O_3, 0.3 wt% CaO, and 0.9 wt% MnO were measured. Compositions from the center and rim of the grain are given in Table 3 (refs 141, 142). Electron

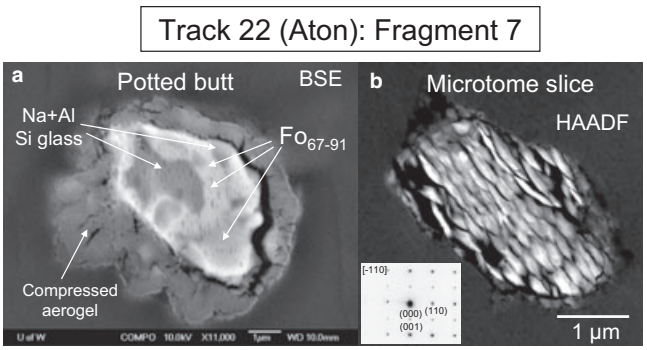

Fig. 5. a) Potted butt BSE image of fragment 7 from track 22. FeO-rich olivine (bright regions) is easily delineated from Na + Al silicate-rich glass (dark gray). A pronounced compressed aerogel rim is visible around the periphery of the fragment. Dark moat between fragment and compressed aerogel rim is from acrylic shrinkage during FESEM imaging. b) HAADF image of microtomed slice, which was cut ~3 microns above potted butt. [-110] zone axis diffraction pattern consistent with olivine structure (Bayliss et al. 1980).

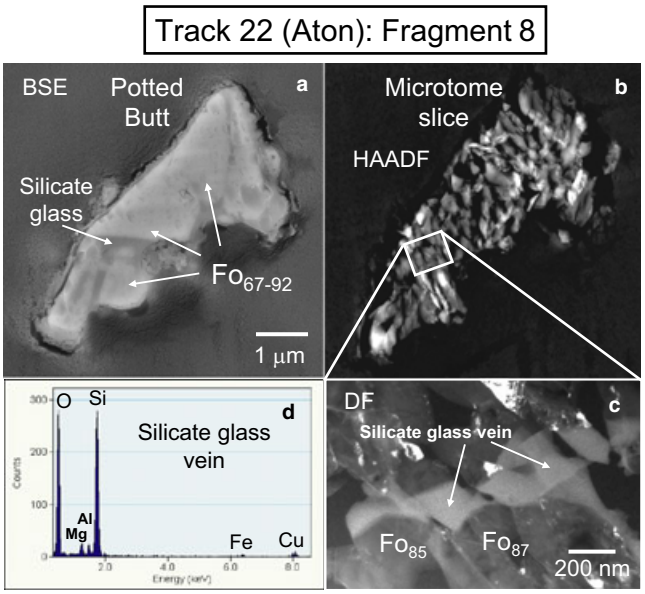

Fig. 6. a) Potted butt BSE image of fragment 8 from Track 22. Mineralogy is similar to fragment 7 and consists of FeO-rich olivine and silicate glass. b) Oriented HAADF image of microtome slice cut within 0.5 μm of potted butt surface. c) Dark-field image showing detail of silicate glass vein in sharp contact with FeO-rich olivine. d) EDX spectrum of Mg + Al-bearing silicate glass vein (minor Fe).

diffraction patterns taken from the fragment are consistent with olivine (Fig. 5b inset).

Al-rich silicate glass ± Na, ± Mg, often in sharp contact with the FeO-rich olivine, occurs in interior locations and along the exterior margins of fragment 7. EDX spectra from the potted butt show the presence of a prominent Na peak (in addition to Mg and Al); however, we did not observe Na in the glass in the microtome sections. Rather, Mg and Al were prominent with minor amounts of P, K, Ca, and Fe (Table 6, ref 167). The glass is apparently heterogeneous in the fragment. A single 200 nm euhedral Fe-Zn sulfide inclusion with 23.6 wt% Zn and 0.9 wt% Mn was found embedded in the glass, which was present in the interior of the microtome slice sandwiched between olivine shards.

A third fragment (fragment 8), 5 × 2.5 μm in size, was extracted from a side track 2.5 mm above the terminal particle (Figs. 1a and 6). TEM EDX analyses show that this grain is largely composed of unequilibrated $Fo_{67–92}$ olivine and contains small quantities of silicate glass. BSE and dark field TEM images (Figs. 6a and 6c) show that a prominent 0.2 μm-wide glass vein is sandwiched between a 1 μm blocky olivine and the interior of the main fragment. The glass composition (Table 6, ref 290) in the vein is similar to the Al + Mg-rich silicate glass of fragment 7 (Fig. 5).

The TP from track 22 was studied by TEM by Tomeoka et al. (2007, 2008). Microtome sections revealed

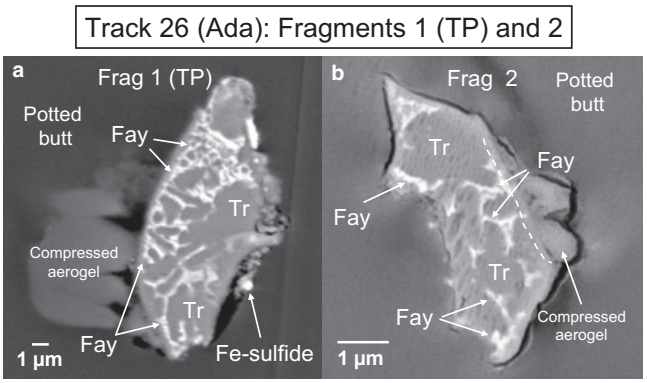

Fig. 7. Potted butt BSE images of terminal particle (fragment 1) and sub-terminal particle (fragment 2) from track 26. Dark gray rounded interior regions are composed of tridymite, while bright surrounding rims are Mn-bearing fayalite. "Sails" of compressed aerogel are visible on each fragment. Dotted line in (b) delineates fragment from compressed aerogel. Fay = fayalite, Tr = tridymite.

anhedral- to lath-shaped grains of $Fo_{64–93}$ olivine with sizes between 0.2 and 2.0 μm, polycrystalline FeO-bearing diopside ($Fs_{9–12}$), and an Al-rich silicate glass in grains up to 1.0 μm in size. Fe-Ni sulfides and metal were absent.

In summary, we observed three large fragments in track 22, a type A track, including two assemblages composed of FeO-rich olivines + Al-rich silicate glass (± a few minor elements) and a large silica fragment believed to be compressed aerogel. The TP, studied by Tomeoka et al. (2008), is also composed of a FeO-rich olivine ($Fo_{64–93}$) and Al-silicate glass, but a small quantity of diopside was also present. The unusually large number of discrete fragments present in the track suggests that the impactor was not a structurally strong particle.

Track 26 (Ada)

Track 26 is a > 2-mm-long type A track which is composed of a ~0.75-mm-long cavity and two bifurcated main branches each of which contains a large fragment (Fig. 1a). At least six smaller fragments are present at the termini of short side tracks or along track walls (not shown). We studied only the terminal and sub-terminal particles (fragments 1 and 2, respectively). The upper portion of the track, closest to the entry hole, was not present in the aerogel keystone.

Optical examination showed that the terminal particle (fragment 1) was approximately 10 × 20 μm in size and that fragment 2 was marginally smaller. BSE images of the potted butts of the TP and fragment 2 are shown in Fig. 7. The fragments are texturally similar and consist of essentially identical but unusual mineralogy,

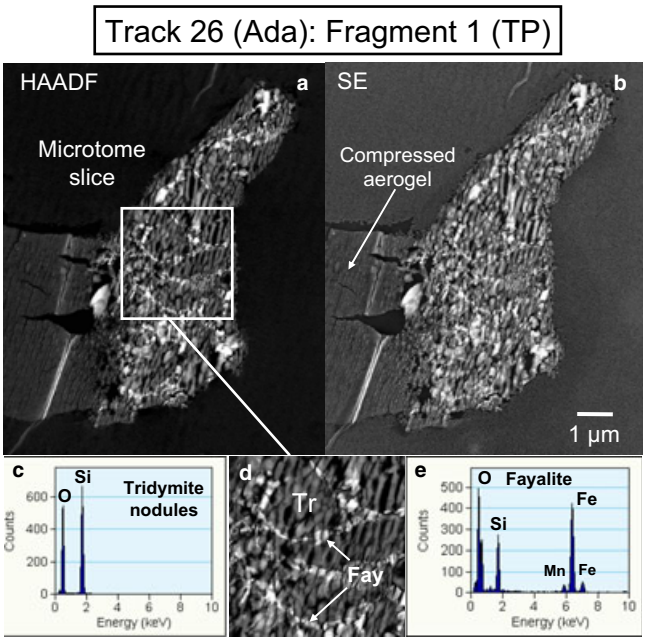

Fig. 8. Complementary HAADF and SE images of a microtomed slice from the terminal particle from track 26 (Ada). Nodules of tridymite (dark gray) surrounded by rims of fayalite (white) are clearly visible in the HAADF image. c, e) EDX spectra of a tridymite nodule and fayalite rim. d) Magnified view of interior of HAADF image showing tridymite (dark gray) and fayalite (white) phases. TP = terminal particle, Tr = tridymite, Fay = fayalite.

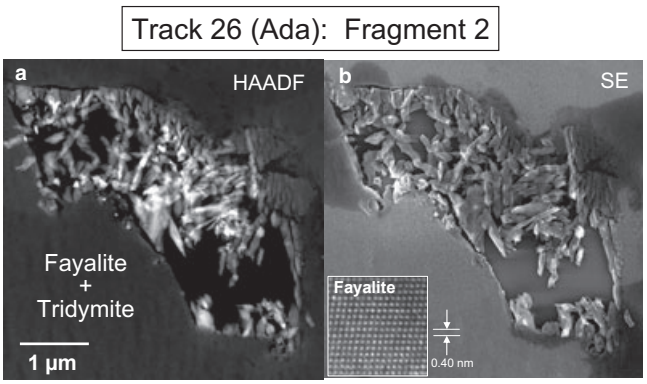

Fig. 9. Complementary HAADF and SE images of a microtomed slice of the sub-terminal particle (fragment 2) from track 26. Shards are composed of tridymite and fayalite similar to the TP. High-resolution BF image of fayalite (inset figure b) on minor zone axis [-31-2] confirming fayalite atomic structure.

indicating that fragments 1 and 2 were probably joined together prior to capture. In Fig. 7, the 0.5–3 μm elongate to rounded dark gray nodules are composed of nearly pure SiO_2 (tridymite) and have bright fayalite rims around major portions of their perimeters. Significant "sails" of compressed aerogel are attached to the outer portions of each fragment.

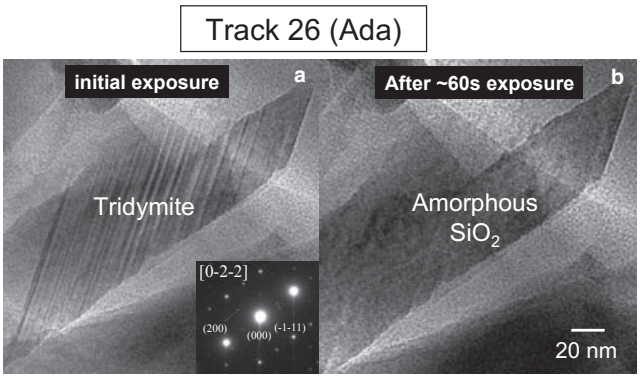

Fig. 10. a) TEM image of shard showing crystalline nature of track 26 SiO_2 phase during initial exposure to electron beam. Minor zone-axis difraction pattern, taken during initial exposure of SiO_2 phase, is consistent with tridymite (Graetsch and Topalovic-Dierdorf 1996). b) Same shard showing conversion to amorphous state after moderate exposure to electron beam.

HAADF and SE STEM images of both fragments are shown in Figs. 8 and 9. The SiO_2 nodules, which are easily visible in Figs. 8a and 8d, appear to be cemented together with ~100 nm wide fayalite rims, thus forming the larger aggregate TP. EDX spectra taken from the interiors of the nodules show that they are typically composed of nearly pure SiO_2 (Fig. 8c; Table 7, ref 187), although up to 1 wt% Al_2O_3 has been measured in some nodules. TEM bright field observations coupled with tilting experiments of this phase have shown that it is a crystalline SiO_2 material which rapidly decomposes to amorphous SiO_2 with exposure to the electron beam, often in less than 30–60 s under typical imaging conditions (Figs. 10a and 10b).

EDX spectra taken from the bright rims on the tridymite nodules indicate that this phase is fayalite (Fig. 8e). We measured Fe/(Fe + Mg) = 0.96 (atomic), with very little variation between rims. The fayalite is compositionally distinct by its high Mn content with MnO values often greater than 6 wt% (Table 3, ref 187). Minor quantities of Al, P, and Cr were also observed in the fayalite. Electron diffraction patterns and HRTEM images (Fig. 9b, inset) confirm the olivine structure.

Although composed principally of crystalline SiO_2 and FeO-rich olivine, a few minor phases were found along the periphery of the fragments. Chromite was noted in 20 nm-wide veins and as inclusions up to 50 nm in size in a single localized region in the TP, while rare round inclusions of Fe sulfide and a Cu-Fe sulfide, believed to be cubanite, were also observed in other locations. We cannot be sure whether these phases are primary or were produced during capture.

In summary, track 26 contains two large fragments (plus several smaller fragments that we did not study)

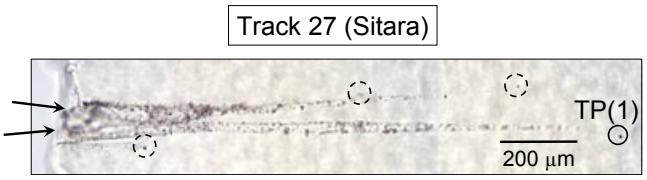

Fig. 11. Transmitted light image of flattened track 27 (Sitara) showing the two main roots. We examined the TP, but not the other large fragments (dotted circles). It is unclear whether the two roots resulted from a single impacting particle that split into two fragments at entry, or whether two independent particles from Wild 2 entered side-by-side into the aerogel cell (arrows).

composed of clusters of compact tridymite nodules with MnO-rich fayalite rims. This track has the only fayalite reported in SD tracks and is much more FeO-rich than olivines from all other observed tracks (Track 80 contains the second highest FeO-rich olivines: $Fo_{41–43}$). The unique mineralogy and texture of the two fragments studied in the track suggest that they were part of a single larger grain before capture.

Track 27 (Sitara)

Track 27 is a 1.3-mm-long type A track consisting of two carrot-shaped roots with large fragments at each termini (Fig. 1a). At least two smaller fragments are located at the ends of short side tracks (not shown), and only small amounts of fine-grained debris are present outlining the track walls. Close inspection of the entry region shows subtle linear features in the interior of the cavity, which appear to be the outlines of the walls of two separate tracks (Fig. 11, black arrows), showing that the impactor separated into two fragments very near its entry point. We studied only the TP (fragment 1) which was present at the terminus of the longest root.

A BSE image of the potted butt and oriented HAADF image of a microtome slice of the TP are shown in Figs. 12a and 12b. The microtome slice shown in the figure was cut approximately 1 μm above the potted butt. The terminal particle is composed of four distinct minerals: a 3 × 5 μm low-Ca pyroxene, which dominates the bulk of the fragment and is easily visible by the large microtome-produced chatter marks, two sulfides (pentlandite and pyrrhotite) present at opposite ends of the fragment, and kosmochloric augite, which occupies an L-shaped region between the low-Ca pyroxene and pyrrhotite and a smaller region bordering pentlandite.

Several EDX analyses (Table 4, ref 153) obtained from different portions of the low-Ca pyroxene show that it has a limited range in Wo and En contents (Wo = 3.2–4.5 mol%; En = 77.5–82.1 mol%). Measured abundances of Al_2O_3, Cr_2O_3, and MnO range from 0.1–0.6 wt%, 0.5–0.8 wt%, and 0.7–1.0 wt%, respectively. A HRTEM image obtained from a minor zone axis is consistent with the low temperature polymorph clinoenstatite.

Ko-augite is in intimate contact between enstatite and pyrrhotite. In the BSE image, sharp, straight grain boundaries are evident between the Ko-augite and pentlandite, while grain boundary contacts with pyrrhotite are sharp, but curvilinear (Fig. 12a). A small Ko-augite grain attached to pentlandite on the opposite end of the fragment is also present, suggesting that Ko-augite was continuous along the left-hand edge of the enstatite (Fig. 12a). EDX analyses of the augite have shown that Ca/(Ca + Fe + Mg) = 0.40–0.41 (atomic) and that the pyroxene contains very high Na_2O and Cr_2O_3 contents (Fig. 12c), which range from 4.5–5.5 to 7.8–13.0 wt% (Table 4, ref 150), respectively. Diffraction patterns are consistent with the augite crystal structure (Fig. 12c). Unlike most other tracks where Ko-augite has been observed, the Ko-augite in this track is not associated with FeO-rich olivine.

The bright Fe sulfide grains are striking features in the BSE and HAADF images. In the latter image (Fig. 12b), the large euhedral pentlandite visible near the right hand side of the fragment was displaced from its original location near the upper left-hand side in the figure during microtoming. Compositional analyses of the pyrrhotite show that Fe/(Fe + S) = 0.97 with a Ni concentration of 0.6–0.7 wt% (Table 5, ref 232). Co abundances from 0.0 to 0.34 wt% were measured. In textural contrast to the pyrrhotite, pentlandite is distinctly euhedral and displays sharp straight grain boundaries between enstatite and Ko-augite. Diffraction patterns confirmed the pentlandite crystal structure (Bayliss et al. 1980). We measured Fe/(Fe + Ni) = 0.43 (atomic) with concentrations up to 0.9 wt% Co (Table 5, ref 610).

In summary, the impactor that produced track 27 was approximately 9 μm in size and was composed of a compact assemblage of 4 minerals including FeO-rich enstatite, pyrrhotite, pentlandite, and kosmochloric augite. It is unknown whether a second fragment (unstudied), which is present at the end of a second root, is related to the TP or not.

Track 38 (Tara)

Track 38 (Tara) is a classic carrot-shaped type A track (Fig. 1a) narrowing monotonically from a maximum width of approximately 40 μm (after flattening between glass slides) just below the entry hole to its terminal particle lodged 3.2 mm below. No significant short side tracks are present, indicating that the impactor was predominantly composed of a single competent coarse-grained fragment.

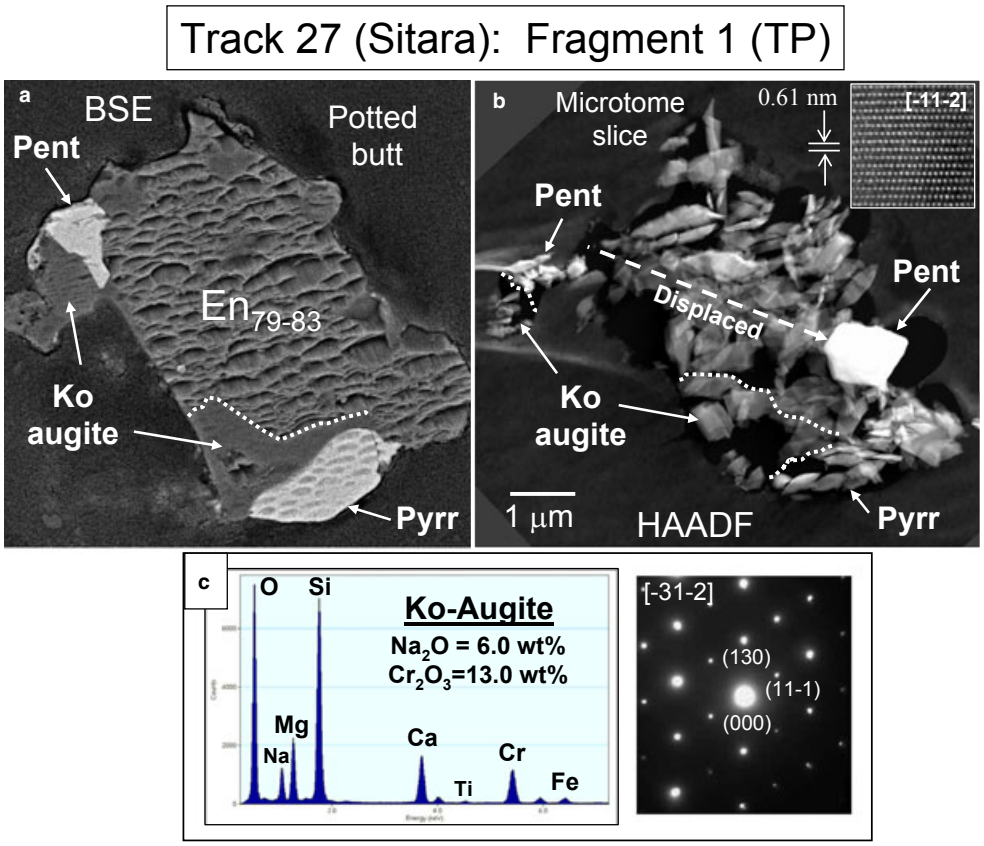

Fig. 12. a) Backscatter FESEM image of fragment 1 (TP) from track 27 (Sitara) consisting of FeO-rich low-Ca pyroxene ($En_{79–83}$), Ko-augite, and the two sulfides pentlandite and pyrrhotite. Variable scalloped textures present in all phases are a result of surface plucking from microtoming. Dotted line shows contact between Ko-augite and low-Ca pyroxene. b) HAADF image of microtome slice of TP oriented to BSE image. Dotted lines delineate phases visible in (a). Large prominent euhedral pentlandite was displaced across slice during microtoming (dashed line). High-resolution BF image shown in inset is taken from low-Ca pyroxene and matches clinoenstatite. c) EDX spectrum of Ko-augite and minor zone axis diffraction pattern [-31-2] is consistent with augite crystal structure.

Table 5. Representative chemical compositions of Wild 2 Fe-Ni sulfides.

Track	10	10	10	27	27	57	59	77	77	141	141	141
Name	Arinna	Arinna	Arinna	Sitara	Sitara	Febo	Naomi	Puki	Puki	Coki	Coki	Coki
Frag no.	1 (TP)	1 (TP)	13	1 (TP)	1 (TP)	1 (TP)	1 (TP)	8	51	1 (TP)	1 (TP)	1 (TP)
Phase	Pyrr	Sph	Pent	Pent	Pyrr	Pyrr	Pent	Pyrr	Pyrr	Pyrr	Pent	Sph
Ref	255	256	266	610	232	174	281	551	527	545	541	543
					Element weight % (normalized to 100%)							
O	5.33	4.30	b.d.	0.23	0.84	2.43	n.a.	n.a.	n.a.	3.05	0.83	16.06
Si	0.54	0.86	0.34	1.16	1.26	0.22	4.66	n.a.	b.d.	2.33	2.28	5.38
S	35.38	35.48	34.65	35.03	36.44	36.66	33.99	36.61	35.93	34.65	33.61	27.87
Cr	b.d.	b.d.	b.d.	0.11	b.d.	0.03	b.d.	b.d.	b.d.	b.d.	b.d.	b.d.
Mn	b.d.	2.46	b.d.	0.20	b.d.	0.30	b.d.	b.d.	b.d.	0.33	b.d.	0.87
Fe	58.60	26.43	35.11	25.80	60.89	59.46	33.54	62.11	63.22	58.30	36.11	19.54
Co	b.d.	0.26	1.84	0.80	b.d.	b.d.	1.25	b.d.	b.d.	0.49	1.39	0.27
Ni	0.15	0.15	28.07	36.68	0.57	0.89	25.56	1.26	0.85	0.85	25.81	0.13
Cu	b.d.	b.d.	b.d.	b.d.	b.d.	b.d.	b.d.	b.d.	b.d.	b.d.	b.d.	b.d.
Zn	b.d.	30.07	b.d.	b.d.	b.d.	b.d.	b.d.	b.d.	b.d.	b.d.	b.d.	29.88

Pent = pentlandite, Pyrr = pyrrhotite, Sph = sphalerite, TP = terminal particle, b.d. = below detection, n.a. = not analyzed.

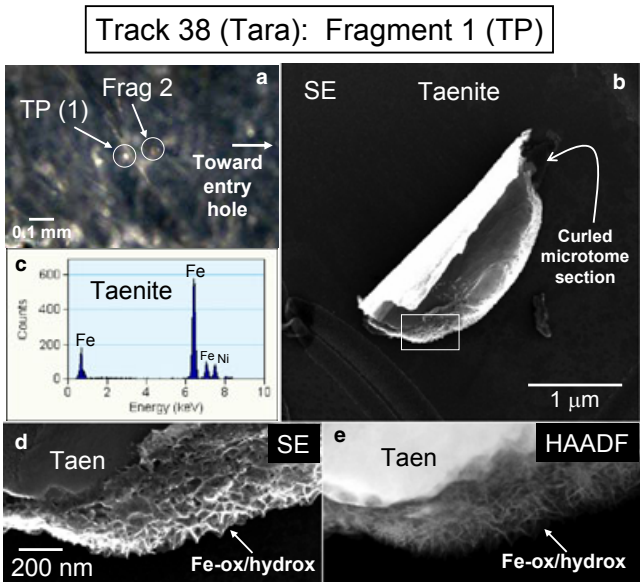

Fig. 13. a) Optical image of the relative locations of TP and fragment 2 (Fig. 14) in track 38 (Tara). b) SE image of the curled terminal particle, taenite, after microtoming. c) EDX spectrum of taenite. The metal grain contains 10.1 wt% Ni. d) SE image of Fe-oxide or Fe-hydroxide present on exterior of taenite. Dotted line shows contact between taenite and Fe-oxide/hydroxide. e) Comparable HAADF image to SE image in (d) showing both taenite and coating of Fe-oxide/hydroxide. Fe-ox/hydrox = Fe-oxide/Fe-hydroxide, taen = taenite, TP = terminal particle.

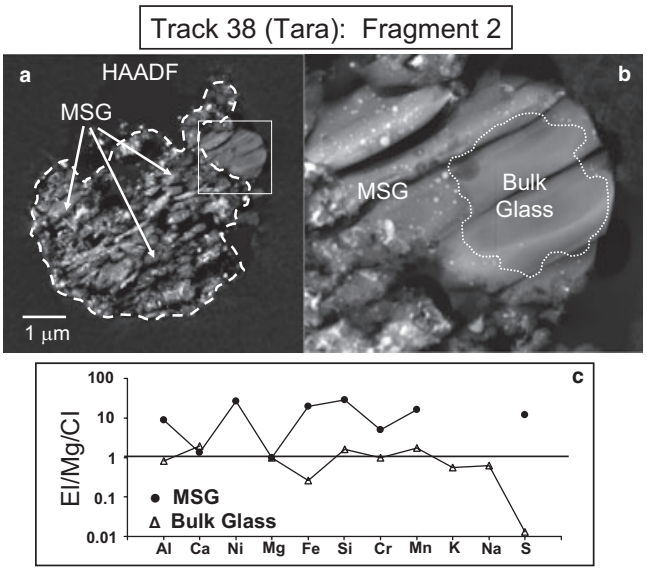

Fig. 14. Fragment 2 from track 38 (Tara) located approximately 100 μm from the TP. a) HAADF image of microtomed section showing that fragment 2 is composed of a mixture of MSG (metal + sulfide + glass), which may have formed from mixing of projectile components and aerogel during capture and an inclusion-free bulk glass of different composition. b) Magnified HAADF image of outlined square in (a) showing bulk glass (Table 6, ref 216) and relatively sharp contact (dotted outline) with MSG. c) El/Mg/CI-normalized plot of respresentative MSG and bulk glass showing that significant compositional differences exist between these two components. The bulk glass may represent the core of primary indigenous glass from comet Wild 2.

The terminal particle (fragment 1) and a 6 μm fragment (fragment 2; Fig. 13a), located ~100 μm uptrack, were examined. A third fragment is present along the track and located approximately one quarter of the distance to the TP (not shown). We did not study this fragment by TEM, but it has been examined by X-ray absorption near-edge structure (XANES) and was identified as a FeO-bearing olivine (unpublished data). The TP is composed of a rounded Fe,Ni metal grain with a diameter of ~3 μm (Fig. 13b). The apparent circular shape of the fragment is presumably due to abrasion during track deceleration. This is supported by the observation that sub-micrometer metal debris of similar composition was found elsewhere in the track. In the SE STEM image (Fig. 13b), the TP is visible in a tightly curled shape, thus only EDX analyses along the extreme edge were possible. An additional complication was the presence of numerous poorly crystalline Fe-oxide or Fe-hydroxide crystals along the edge of the fragment, presumably due to oxidation/hydration during sample preparation (Figs. 13d and 13e). EDX analyses obtained from "clean" locations along the edge of the metal grain (Fig. 13c) show that the Fe/(Fe + Ni) ratio is 0.9, indicative of γFe,Ni, i.e., the face-centered cubic high temperature polytype taenite (Table 8, ref 54). Due to our inability to probe the entire fragment, we were unable to determine whether kamacite coexists with the taenite. Approximately 0.3 wt% Co was present in the metal.

A microtome section of fragment 2 is shown in Fig. 14. The HAADF image (Fig. 14a) shows that this fragment is composed of two texturally distinct regions, one dominated by MSG and the other a smaller inclusion-free bulk glass located on the upper right side. The MSG is a product of mixing of probable fine-grained components in the impactor with silica aerogel during collection (Leroux et al. 2008b; Velbel and Harvey 2009; Stodolna et al. 2011). The bulk glass is compositionally distinct (Table 6, ref 216) from the MSG and may represent a primary glass. Except for the element S, which is low by a factor of 100, the measured major elements in the bulk glass are chondritic within a factor of two (Fig. 14c). In the El/Mg/CI plot, the elements Al, Fe, Si, Cr, and Mn in the MSG are all ~10× greater than the bulk glass. The textures evident in Fig. 14b indicate that the bulk glass did mix with MSG along its periphery, but apparently, the central core was preserved. The bulk glass that is present in fragment 2 is

Table 6. Representative chemical compositions of silicate glasses (normalized oxide wt%).

Track	22	22	38	38	41	41	56	57	58	59	61	80
Name	Aton	Aton	Tara	Tara	Isis	Isis	Key A	Febo	Noni	Naomi	Allie	Tule
Frag #	7	8	2	2	3	9	1 (TP)	103	1 (TP)	1 (TP)	1 (TP)	2
Ref	167	290	216	219[a]	162	610	215[b]	571	226	559	560	205
SiO_2	82.50	83.71	57.90	55.56	76.73	64.85	80.30	60.66	75.50	99.81	75.83	63.11
TiO_2	0.00	0.54	0.00	0.00	0.00	0.30	0.29	0.54	0.00	0.00	0.00	0.00
Al_2O_3	2.68	3.89	1.79	1.04	10.68	2.90	1.11	9.38	17.93	0.00	16.51	5.83
Cr_2O_3	0.00	0.00	0.60	0.22	0.00	0.94	0.17	0.23	0.00	0.00	5.43	2.37
FeO	2.02	2.52	9.49	41.03	4.55	1.11	2.23	11.11	0.38	0.19	2.24	5.32
MnO	0.43	0.37	0.67	0.40	0.30	0.00	0.33	0.52	0.00	0.00	0.00	0.48
MgO	10.20	7.41	24.90	1.36	4.58	28.31	13.72	9.24	5.63	0.00	0.00	13.29
CaO	0.57	0.24	3.94	0.34	1.56	1.59	0.16	8.32	0.13	0.00	0.00	6.12
Na_2O	0.00	0.00	0.65	0.00	0.28	0.00	0.95	0.00	0.00	0.00	0.00	1.51
K_2O	0.48	0.17	0.06	0.05	0.50	0.00	0.74	0.00	0.43	0.00	0.00	0.52
P_2O_5	1.14	1.16	0.00	0.00	0.81	0.00	0.00	0.00	0.00	0.00	0.00	1.44
CIPW normative minerals (wt%)												
Q	63.61	70.28	4.94	23.06	61.79	18.91	53.18	24.54	64.91	99.68	78.78	22.81
C	2.16	3.71	0.00	0.37	8.78	0.02	0.00	0.00	17.23	0.00	17.45	0.00
Or	2.84	1.00	0.35	0.30	2.95	0.00	4.37	0.00	2.54	0.00	0.00	3.13
Ab	0.00	0.00	5.50	0.00	2.37	0.00	1.59	0.00	0.00	0.00	0.00	13.12
An	0.00	0.00	1.82	1.69	2.45	7.94	0.00	25.62	0.64	0.00	0.00	7.77
Di	0.00	0.00	14.21	0.00	0.00	0.00	0.62	12.87	0.00	0.00	0.00	10.96
Hy	29.37	22.19	71.60	67.99	19.06	72.33	37.54	34.13	14.61	0.30	3.01	37.78
Mt	0.32	0.41	1.53	6.60	0.74	0.17	0.00	1.80	0.06	0.03	0.38	0.88
Chr	0.00	0.00	0.13	0.04	0.00	0.21	0.37	0.04	0.00	0.00	1.16	0.52
Il	0.00	1.02	0.00	0.00	0.00	0.57	0.55	1.03	0.00	0.00	0.00	0.00
Ap	2.64	2.69	0.00	0.00	1.88	0.00	0.00	0.00	0.00	0.00	0.00	3.41

[a]Bulk MSG composition. 13.5 wt% SO_3 present in analysis (ref 219), but not shown in table.
[b]1.31 wt% Na_2SiO_3 and 0.72 wt% acmite components not shown in "Norm".

similar to inclusion-free glass regions in MSG material from bulbous Stardust tracks that have been discussed by other researchers (Leroux et al. 2008b; Roskosz et al. 2008; Stodolna et al. 2009). These authors have argued that the Mg-rich inclusion-free glassy regions observed with MSG resulted from low-Fe, Mg-rich precursor minerals, which melted during capture heating and mixed with silica aerogel. However, because the bulk glass composition in fragment 2 is ~chondritic for nearly all elements measured, it is uncertain whether this explanation can account for its origin. The issue of whether primary glasses exist in comet Wild 2 is important, as sources for this material can be either nebular or interstellar (Wooden 2008).

In summary, the ~9 μm captured particle that formed track 38 was apparently dominated by a Fe,Ni metal grain, which forms the TP. A ~chondritic (most major elements, except S) inclusion-free glass located near the TP and largely encased in MSG may represent the remnant core of a primary glass from Wild 2. Alternatively, this glass could be a modified capture product from a crystalline silicate. An MgO-rich olivine located ~2mm from the TP was also present in the impactor.

Track 41 (Isis)

Track 41 is an 11-mm-long type B track composed of a large bulbous cavity residing above a long and progressively narrowing stylus, which contains the TP ~2 mm below the bulb base (Fig. 1b). By far, this is the longest and volumetrically largest track in this study. A second fragment is located at the terminus of a shorter root approximately halfway between the main bulb and the TP. Fe XANES analyses have shown that both the TP and the sub-terminal particle are Fe,Ni metal grains (Ogliore et al. 2010). In a Fe XANES study of a random selection of 33 Fe-bearing fragments from the bulb region of the track, Ogliore et al. (2010) showed that the fraction of Fe in Fe^0, Fe sulfide, and oxidized Fe phases is 0.30:0.52:0.18, respectively. The size and shape of the cavity suggest that significant fine-grained debris could have been present in the Wild 2 impactor. We did not study the terminal or sub-terminal particle, but examined 9 fragments from the bulb wall, which ranged in apparent size from 1 to 5 μm (Figs. 15–17).

BSE and HAADF images of the potted butt and a microtome slice of the largest fragment (fragment 1), which has an apparent size of 3.5 × 5 μm is shown in

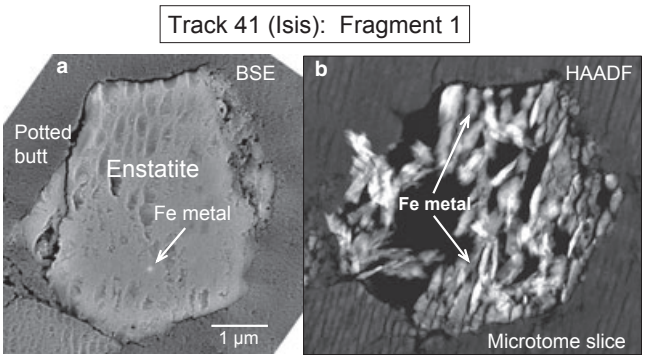

Fig. 15. a) BSE image of potted butt of fragment 1 from the bulb region of Track 41 (Isis). Submicron bright grain indicated by arrow shows Fe metal bead. The "divots" visible along much of the surface of the grain are artifacts from plucking during microtoming. b) HAADF image of a microtome slice of fragment 1 oriented to potted butt image shown in (a). TEM examination has shown that this fragment is mineralogically and texturally complex, but is dominated by nearly Fe-free enstatite, which may have experienced moderate levels of shock.

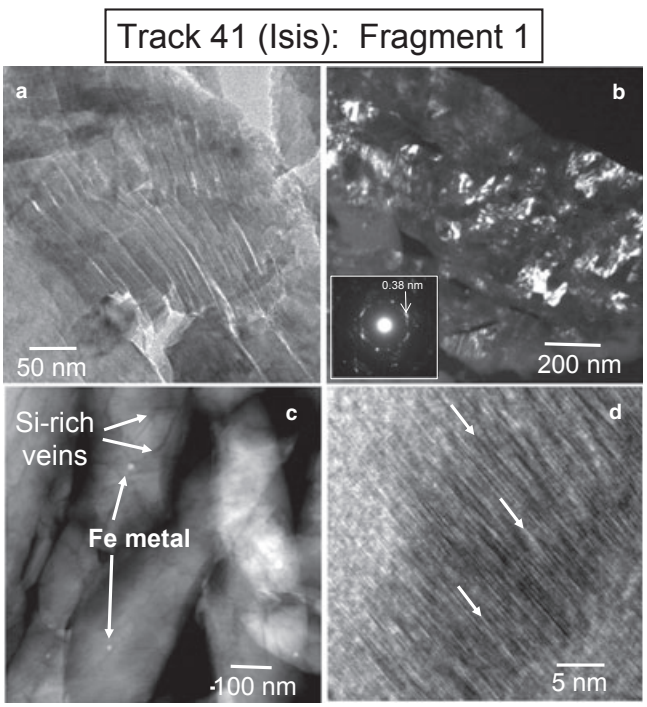

Fig. 16. Images from the interior of track 41 fragment 1 (Fig. 15) showing textures consistent with low-to-moderate levels of shock. a) Enstatite grain with crystal curvature and cleavage delaminations. b) Dark-field image showing rounded and highly embayed subgrains. Polycrystallinity confirmed by electron diffraction pattern (inset). c) HAADF image of nanophase Ni-free Fe metal beads present in enstatite and dark anastomosing veins composed of Si-rich glass (determined from high-resolution element maps, not shown). d) High-resolution image showing numerous edge dislocations (arrows) in enstatite.

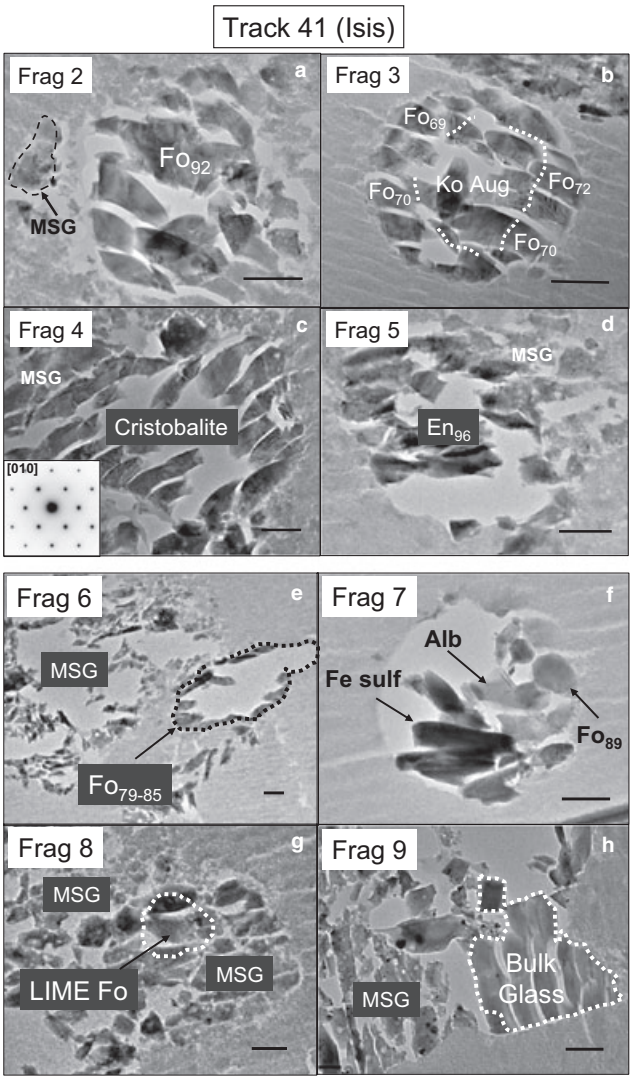

Fig. 17. Large mineral and rock fragments studied from the bulb area of track 41 (Isis). a) Fragment 2 is a rounded Fo_{92} grain with minor amount of MSG melt. b) Fragment 3 is a rounded Kool grain composed of FeO-rich olivine concentrically surrounding kosmochloric augite. Rounded nature of this fragment and fragment 2 is likely due to abrasion of the fragment during track deceleration in aerogel and not a result of melting. c) Fragment 4 is a crystalline SiO_2 grain of the high-temperature polymorph cristobalite. Diffraction pattern in inset consistent with cristobalite. MSG surrounds the fragment. d) Fragment 5 is a FeO-bearing enstatite, which is unlikely to be genetically related to fragment 1 (Fig. 15). e) Fragment 6 is a heavily plucked FeO-rich olivine (dotted lines) attached to abundant MSG. Only a few shards located around the perimeter of the plucked region remain of the original fragment. f) Fragment 7 is a albite + olivine + Fe sulfide rock. All three phases have nonstoichiometric compositions. g) LIME forsterite (dotted region) immersed in a significant quantity of MSG. The Mn content is approximately 3× the Fe content (atom%). h) Fragment 9 is bulk silicate glass with associated MSG. The bulk glass contains nearly chondritic refractory elements Ca, Al, and Ti when normalized to Mg. All scale bars = 0.5 μm.

Table 7. Representative chemical compositions of Wild 2 tridymite and roedderite (normalized oxide wt%).

Track	26	41	56
Name	Ada	Isis	Key A
Frag	1(TP)	4	1 (TP)
ID	Trid	Trid	Roed
Ref	187	353	206
SiO_2	98.91	100.00	67.66
TiO_2	b.d.	b.d.	n.d.
Al_2O_3	1.03	b.d.	0.66
Cr_2O_3	b.d.	b.d.	0.24
FeO	0.06	b.d.	2.34
MnO	b.d.	b.d.	0.40
MgO	b.d.	b.d.	14.83
CaO	b.d.	b.d.	0.30
Na_2O	b.d.	b.d.	9.29
K_2O	b.d.	b.d.	4.28
P_2O_5	b.d.	b.d.	n.d.
		Cation formulas	
Si	0.991	1.000	11.717
Al	0.012	0.000	0.135
Cr	0.000	0.000	0.033
Fe	0.001	0.000	0.339
Mn	0.000	0.000	0.059
Mg	0.000	0.000	3.829
Ca	0.000	0.000	0.056
Na	0.000	0.000	3.119
K	0.000	0.000	0.946
P	0.000	0.000	0.000
Total	1.003	1.000	20.232

Cation formulas based on 2 and 30 oxygens for tridymite and roedderite, respectively.
Trid = tridymite, Roed = roedderite, b.d. = below detection.

Fig. 15. Analytical EDX measurements have indicated that this fragment is composed of nearly Fe-free enstatite, but contains considerable Al, Ca, and Cr abundances with measured values ranging up 1.8 wt% Al_2O_3, 3.6 wt% CaO, and 1.0 wt% Cr_2O_3 (Table 4, ref 357). Numerous sub-100 nm spherical Ni-free Fe inclusions dispersed within the enstatite are believed to be metallic Fe (Fig. 15), although wüstite is also possible. Electron diffraction patterns and darkfield- and HRTEM-imaging show that the grain apparently experienced moderate levels of shock as numerous kink bands, cleavage delaminations, curvature of crystal lattices, polycrystallinity, fractured grains, and edge dislocations are present (Fig. 16). It is possible that some of these features (i.e., cleavage delaminations, fractured grains) were a result of ultramicrotomy (Jacob et al. 2009). High-resolution element mapping of microtome slices (not shown) has also confirmed the presence of numerous anatomizing silica veins. Much of the fragment is composed of <200 nm subgrains, which are easily observed in dark field images (Fig. 16b). EDX analyses taken from these regions are consistent with a low-Ca pyroxene composition. In two analyses, however, the Ca contents were marginally high enough for classification as pigeonite (Wo = 6.5 mol%, Table 4, ref 358). Electron diffraction patterns obtained from these regions as well as other locations in the fragment confirm orthoenstatite. EDX measurements in some regions in the fragment suggest the presence of forsterite. Although not quite stoichiometric, we measured Mg/Si ratios >1.5 (atomic) and at least one diffraction pattern confirmed a forsterite crystal structure.

Three fragments (fragments 2, 6, and 8) were found to be single olivine grains (Figs. 17a, 17e, and 17g); significant MSG was associated with fragments 6 and 8. Fragment 2 (Fo_{92}) (Table 3, ref 345) and fragment 6 ($Fo_{79–85}$) have approximately similar Fe/Mg ratios and characteristically low Ca, Mn, and Cr contents and may represent two pieces of a previously larger zoned olivine, which was split into smaller fragments during impact into aerogel. Fragment 8, a LIME (low-Fe, Mn-enriched) olivine (Fig. 17g) has a very low Fe content (FeO = 0.24 wt% and contains $\sim$3$\times$ more Mn than Fe (atom%) (Table 3, ref 161). It is unlikely to be genetically linked to fragments 2 or 6. LIME olivines have previously been reported in IDPs and some meteorites (Klöck et al. 1989).

Fragment 5 is a 2 μm FeO-bearing enstatite (En_{96}) attached to a moderate amount of MSG (Fig. 17d). Up to 1.9 wt% MnO was measured in this grain (Table 4, ref 592). High-resolution images indicate mixed clino- and orthoenstatite with large regions of the grain dominated by clinoenstatite. TEM observations of microtextures and larger-scale morphological features suggest that the grain did not experience shocks like fragment 1, although a few internal fractures were observed. No Fe metal inclusions are present. Compositionally and texturally, this fragment is dissimilar from fragment 1 and therefore the two appear to have no genetic links.

Fragment 3 is a 2 μm-wide round Kool grain (Fig. 17b) and was discussed by Joswiak et al. (2009). The olivine (Table 3, ref 159) and pyroxene (Table 4, ref 160) are in sharp contact and may have an origin by thermal metamorphism in a nebular setting. The round external morphology of the fragment is not a product of melting, but rather is due to abrasion of the exterior surface during capture in aerogel.

Fragment 7 is a round polycrystalline fragment about 2 μm in size (Fig. 17f) and was observed without adhering MSG. It is composed of an assemblage consisting of subhedral Fo_{89} olivine, albite, and Fe-Ni sulfide. Measurements obtained from EDX spectra indicate that all three phases are slightly to moderately nonstoichiometric. Low Na concentrations in the albite, however, may have resulted from Na volatilization during analyses or capture heating, and may not be

inherent to the feldspar, but low measured Si in the olivine and higher than expected S in the Fe sulfide are not likely due to TEM examination or capture effects and are not readily explained.

In addition, we observed crystalline SiO_2 fragments in the microtome sections with apparent sizes up to nearly 3 μm (Fig. 17c, fragment 4). We did not observe this phase with other minerals in the track, although it is associated with MSG. Although generally pure, up to 1.1 wt% Al_2O_3 was measured in some locations (Table 7, ref 353). Diffraction patterns have shown that this phase is very likely to be low cristobalite (Fig. 17c, inset), although one minor zone axis pattern was consistent with tridymite (Graetsch and Topalovic-Dierdorf 1996). Cristobalite and tridymite are low pressure, high temperature polymorphs of crystalline SiO_2. Given its size, it seems unlikely that this fragment could have formed from capture heating.

Finally, we observed conspicuous bulk silicate glass in regions ranging up to 2 μm in extent (fragment 9, Fig. 17h). This glass occurs with MSG, but generally sharp contacts delineate the two components. EDX analyses (Table 6, ref 610) show that the bulk glass is essentially chondritic in the refractory elements Al, Ca, and Ti when normalized to Mg. This is in contrast to the bulk MSG, which is enriched 3–5× in these same elements. Both, however, have Na, K, and Mn below detection limits. The bulk glass from fragment 9 could represent a core of primary silicate glass from the impactor that did not mix with melted projectile components (presumably fine-grained) during capture heating. Alternatively, the glass could be a remnant from mixing during collection between a silicate mineral in the original impactor and hot silica aerogel similar to some glassy regions discussed by Roskosz et al. (2008) and Leroux et al. (2008b) (see above, track 38-fragment 2).

In summary, the impacting particle that produced track 41 was composed of a large mixture of coarse mineral and rock fragments including enstatite; three or more compositionally dissimilar olivines, cristobalite, silicate glass; and at least one Kool grain. Abundant MSG is also present in the track. The captured Wild 2 particle was apparently composed of an unequilibrated assemblage of coarse fragments and possibly fine-grained matrix materials.

Track 56 (Key A)

Track 56 is a short (650 μm) carrot-shaped type A track (Fig. 1a) that contains an optically transparent TP < 5 μm in diameter. The TP is composed of a mixture of an unusual assemblage of roedderite, kosmochloric augite, enstatite, and alkali silicate glass (Fig. 18). In addition, minor quantities of Fe-Ni sulfide,

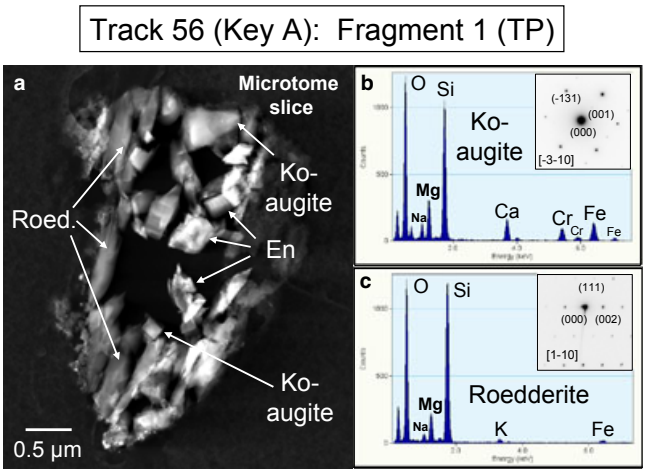

Fig. 18. a) HAADF image of a microtome slice of track 56 (Key A) fragment 1 (TP) consisting of roedderite, kosmochloric augite, and enstatite. Dark interior regions show the absence of grains due to plucking during microtoming. b, c) EDX spectra and corresponding electron diffraction patterns of Ko-augite and roedderite. Roed = roedderite, Ko-augite = kosmochloric augite, En = enstatite.

stoichiometrically equivalent to troilite, and a 300 nm round chromite were observed. Small amounts of compressed aerogel are present on the exterior and little to no additional debris is present in the remainder of the track, indicating that the impactor was a strong competent grain with little to no attached fine-grained material.

The most widespread phase, roedderite, is a low-Al, Mg-bearing alkali silicate that was first described in 1966 in the enstatite chondrite Indarch (Fuchs 1966). In Key A, it is observed as broken shards and fragments (a result of microtoming) up to 1 μm long. Roedderite belongs to the osumulite group of minerals and is the Mg end-member of the solid-solution series roedderite-eifelite: $(Na,K)_2(Mg,Fe)_5Si_{12}O_{30}$-$KNa_3Mg_4Si_{12}O_{30}$ (Abraham et al. 1983). In the microtomed sections that we examined, the phase exhibits a narrow range in composition with $Na/(Na+K)$ = 0.83–0.87 (atomic) and $Mg/(Mg+Fe)$ ~0.9 (atomic) and compositionally is closer to eifelite (Table 7, ref 206). However, following the usage of Krot and Wasson (1994), we use the term roedderite on the basis of Si/Al > 7.0, Na > K, and Mg > Fe. High-resolution imaging and electron diffraction patterns confirm the atomic structure as roedderite/eifelite (Fig. 18c, inset). In places, the roedderite occurs with alkali-bearing silicate glass (Table 6, ref 215), suggesting that conversion to a glass from the crystalline mineral may have occurred during capture heating and cooling. Alternatively, roedderite may have formed from devitrification of the alkali-rich glass, presumably prior to incorporation into comet Wild 2.

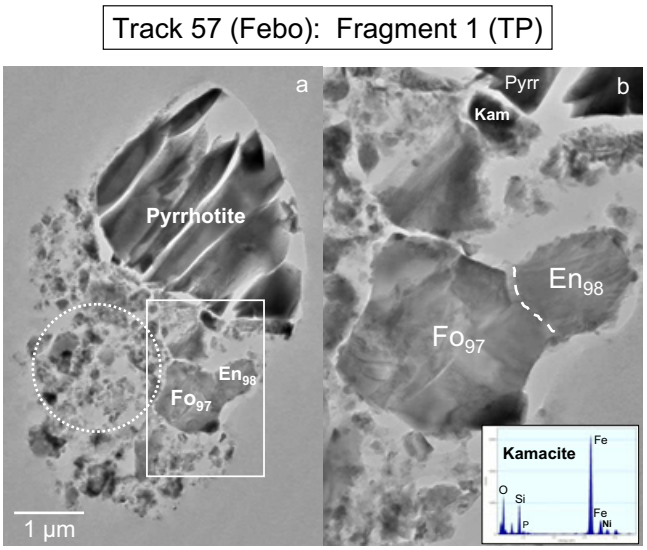

Fig. 19. a) Bright-field image of large pyrrhotite, fine-grained region, and large Fo_{97} and En_{98} grains. Dotted circle shows area where bulk composition from fine-grained region was obtained (see text). b) Detail showing sharp contact between Fo_{97} and En_{98}, fine-grained material and kamacite juxtaposed on edge of large pyrrhotite. EDX spectrum from kamacite grain and minor amount of attached SiO_2 glass.

Two pyroxenes, one a Na- and Cr-rich high-Ca pyroxene with Fe/(Fe + Mg) = 0.34 (atomic) and the other a low-Fe enstatite (Table 4, ref 207) are present in smaller quantities. In the kosmochloric pyroxene, measured Na_2O and Cr_2O_3 oxides range up to 2.9 and 7.3 wt%, respectively (Table 4, ref 359), while Wo contents span the pigeonite field and are transitional to augite. Zone axis patterns (Fig. 18b, inset) are consistent with the augite crystal structure (Bayliss et al. 1980). In some microtome sections, the kosmochloric augite/pigeonite was observed sharply in contact with roedderite, suggesting a possible reaction relationship.

In summary, Wild 2 particle that excavated track 56 was a single competent ~9 μm impactor composed of an assemblage of roedderite, kosmochloric augite, and enstatite ± alkali silicate glass. Little to no MSG was observed in the track.

Track 57 (Febo)

Track 57 (Febo) is a >1.4-mm-long type B track containing a large optically opaque TP, smaller fragments nested at the termini of shorter side tracks, and a considerable number of small fragments dispersed throughout the bulb. We studied the TP (fragment 1), fragment 2 located at the end of the longest side track, and 9 fragments located within the bulb or along the styli (Fig. 1b). The upper portion of the track was not available for examination.

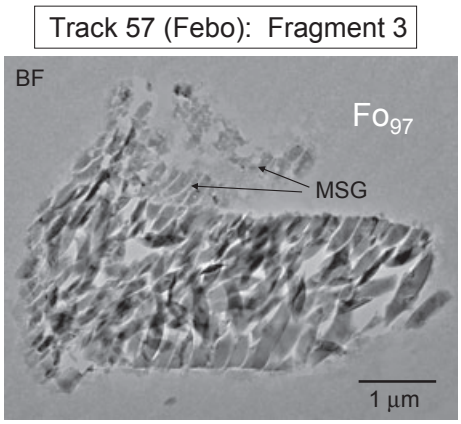

Fig. 20. Bright-field image of microtome slice of fragment 3 (Fo_{97}) from bulb region of track 57 (Febo). The rounded edges are likely due to abrasion from contact with silica aerogel during capture.

Fragment 1, the terminal particle, is a mineralogically complex fragment composed of a large single Fe-Ni sulfide grain, an equivalent volume of attached fine-grained material of roughly chondritic bulk composition, and single micron-sized olivine and enstatite grains (Fig. 19). Several EDX analyses of the large Fe sulfide show that the (Fe + Ni)/S ratio ranges from 0.89 to ~1.0, stoichiometrically consistent with pyrrhotite; measured Ni abundances range from 0.5 to 1.1 wt% (Table 5, ref 174), although a very high Ni content of 10.6 wt% was obtained from one EDX analysis. No diffraction patterns were taken. Small quantities of submicron kamacite and fibrous pyrrhotite, presumably from a different generation than the large pyrrhotite, were also observed wedged between the fine-grained region and the large Fe sulfide. Olivine (Fo_{97}) (Table 3, ref 172) and enstatite (Mg/(Mg + Fe) = 0.98; Table 4, ref 170) up to ~2 μm in size occur sandwiched between the large Fe sulfide and the fine-grained material (Fig. 19b). A distinct common boundary can be observed between the olivine and pyroxene. This observation along with similar Fe/Mg ratios of the olivine and pyroxene may suggest a genetic relationship between these two phases. Discrete olivine fragments (fragments 3 [Table 3, ref 193] and 10 = $Fo_{97–98}$; fragment 3 shown in Fig. 20) and enstatite fragments (fragments 100 and 105 = En_{98}; fragment 100 shown in Fig. 21) found in the bulb of the track are of essentially identical composition to the olivine and enstatite observed in the TP (fragment 1). This suggests that fragmentation of a much larger particle containing olivine, enstatite, and Fe-Ni sulfide occurred during capture.

Closer examination of the fine-grained fraction shows that this material is composed of submicron Fe-Ni sulfide grains, SiO_2-rich glass, and occasional Fe-Mg

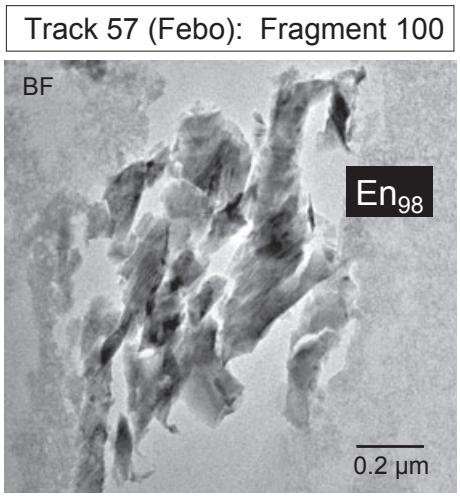

Fig. 21. Isolated En_{98} grain (fragment 100) observed in smaller root of track 57. Other pyroxenes of nearly identical composition were found in the TP and in the bulb region of the track.

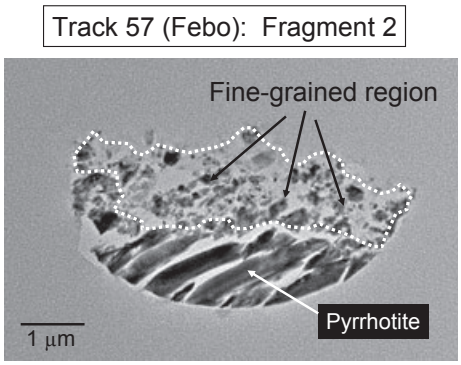

Fig. 22. Bright-field image of large pyrrhotite (fragment 2) and fine-grained region (dotted line) composed largely of submicron Fe-sulfides and silica glass. The large Fe-sulfide and fine-grained region are mineralogically and texturally similar to the TP, suggesting that both fragments were connected into a single larger fragment prior to impact into aerogel. Olivine and pyroxene, unlike fragment 1, were not observed associated with this sulfide fragment.

silicates. Measurement of the bulk composition (dotted circular region in Fig. 19a) indicates that the elements Al, P, K, Ca, Cr, Mn, Fe, and Ni are within ~3× chondritic when normalized to Mg (Si and S are higher and Na is lower). This fine-grained region does not appear to be primary unmelted fine-grained material from the original particle and its origin is unclear.

In a coordinated TEM, NanoSIMS, and XANES study, Matrajt et al. (2008) reported small quantities of organic carbon in microtome sections from this fragment. Occurring as small submicron grains located along the outer edge of the pyrrhotite and within the fine-grained region, the carbonaceous grains were enriched in ^{15}N similar to organic matter observed in primitive carbonaceous chondrites and cometary IDPs (Busemann et al. 2006).

Fragment 2, present at the terminus of a ~300 μm-long side track, is a >5 μm optically opaque fragment, which is composed of a large pyrrhotite with a subequal volume of fine-grained roughly chondritic material (Fig. 22) and is similar to the TP. Because of their textural and mineralogical similarities, fragments 1 and 2 were likely conjoined prior to impact into the aerogel. Unlike fragment 1, however, no olivine or enstatite grains in fragment 2 were present; this may simply be due to shallow microtoming of the fragment.

Two fragments were composed of very low-Fe olivine (fragments 101 and 104; fragment 104 shown in Fig. 23, fragment 101 not shown). These fragments were observed in the bulb region and along the wall of the longest styli. They have Mg/(Fe + Mg) ratios >0.99 and contain MnO > FeO, therefore are LIME olivines. Both contain significant MSG around their peripheries. No

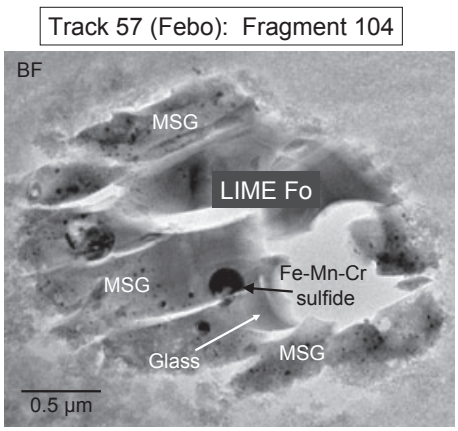

Fig. 23. Bright-field image of fragment 104 from the lower middle portion of bulb of track 57. The $Fo_{99.7}$ fragment, has Mn > Fe (LIME Fo) and is surrounded by MSG. A round 200 nm Fe-Mn-Cr sulfide and enclosing Mg-bearing silicate glass were probably produced during capture.

additional primary phases were associated with these fragments. Fragment 104 contains a 0.25 μm Mn + Cr-rich Fe sulfide and Na-bearing Mg-silicate glass (Fig. 23). Both the Fe sulfide and the silicate glass may be secondary (produced by impact into aerogel) due to their small sizes and intimate association with MSG. It is unlikely that these LIME olivines are genetically related to the Fo_{97} olivines discussed above.

Fragment 103 (Fig. 24) is a ~2 μm wide spherical object (apparent width) composed of a number of ~equilibrated FeO-bearing olivine ($Fo_{81–86}$) grains (Table 3, ref 570), a single En_{87} pyroxene (Table 4, ref 572) and silicate glass rich in Fe, Mg, Ca, and Al (Table 6, ref 571). The fragment was found near the top

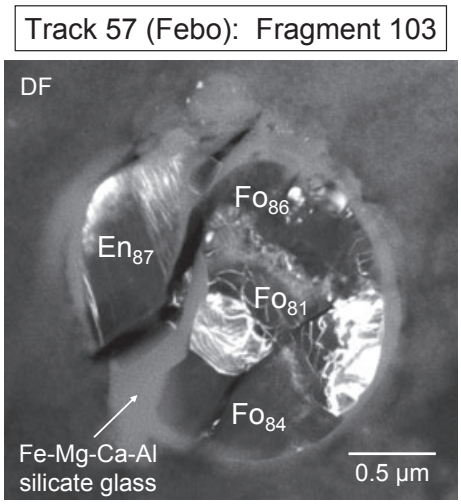

Fig. 24. Dark-field image of fragment 103 in track 57. The fragment is composed of multiple grains of olivine ($Fo_{81–86}$), a single En_{87} grain, and Fe-Mg-Ca-Al-rich silicate glass. Note sharp contacts between pyroxene and olivine grains with silicate glass, suggesting that all three phases formed contemporaneously. It is possible that this fragment is a microchondrule, although its round shape may also be due to abrasion during capture.

of the root containing the TP (Fig. 1b). The olivine grains appear rounded on the exterior of the fragment, but are subhedral to euhedral where they jut into the glass, suggesting their growth during or prior to glass crystallization. The glass is rich in Ca and Al (CaO = 8.3 wt%; Al_2O_3 = 9.4 wt%) and occurs sandwiched between the olivine subgrains and the enstatite crystal and as a thin mantle surrounding the olivine. The calculated Fe-Mg distribution coefficient between olivine and silicate glass from EDX data is 0.31, a value very close to that predicted from equilibrium experiments on mafic silicate liquids (Roeder and Emslie 1970). The calculated Mn distribution coefficient between olivine and glass is 1.01, which is very similar to that obtained between olivine and liquid from mafic silicate liquids at a temperature near 1250°C (Duke 1976). The high Ca and Al contents of the glass indicate that it could not have formed from melting of the olivine. The fracture that bisects the left portion of the fragment is believed to be a result of ultramicrotomy. It is unclear whether its round morphology is a result of abrasion during deceleration into aerogel during capture or is a result of crystallization from a liquid droplet. It is possible that this fragment is a legitimate microchondrule (see discussion below); however, it is also likely that at least some rounding of the fragment occurred during capture similar to what is observed in other SD fragments.

Finally, fragment 120 (not shown), with an apparent size of 1.5 μm, was observed in the walls of the root

Table 8. Representative chemical compositions of Wild 2 metal and schreibersite.

Track no.	38	57	77	77
Name	Tara	Febo	Puki	Puki
Frag	1 (TP)	120	2	3
Phase	Kam	Kam	Kam	Schr
Ref	54	563[a]	553	57
		Normalized el. wt%		
O	b.d.	2.94	b.d.	b.d.
Mg	b.d.	b.d.	b.d.	b.d.
Al	b.d.	b.d.	b.d.	b.d.
Si	0.21	9.48	b.d.	b.d.
S	b.d.	0.47	b.d.	b.d.
P	b.d.	b.d.	0.17	15.29
Ca	b.d.	b.d.	b.d.	b.d.
Cr	b.d.	b.d.	b.d.	b.d.
Mn	b.d.	b.d.	b.d.	b.d.
Fe	89.38	84.36	93.50	45.72
Co	0.28	b.d.	b.d.	b.d.
Ni	10.13	5.61	6.34	38.99

Kam = kamacite, Schr = schreibersite, b.d. = below detection.
[a]Overlaps silicate.

containing the TP. Unfortunately, most of the fragment was plucked out of the acrylic during ultramicrotoming. However, a 0.5 μm remnant observed in one microtome section was composed of kamacite (Table 8, ref 563) with Fe/(Fe + Ni) = 0.95 (atomic). Optical examination of this fragment prior to microtoming indicated that it was opaque. Therefore it is likely that the entire grain was also composed of Fe,Ni metal. Significant loss of material (plucking) during ultramicrotomy is common with cutting of metals.

In summary, track 57 is a mixture of MgO-rich olivines and pyroxenes and mineral assemblages composed of pyrrhotites + fine-grained materials ± $Fo_{97–98}$ + En_{98}. The presence of LIME forsterite, kamacite, and a possible microchondrule attest to the variety of other coarse materials in the impactor.

Track 58 (Noni)

Track 58 is a short 290-μm-long type A track that contains only a single 5 μm TP (Fig. 1a). The TP is a mineralogically unusual fragment composed of a central core of Fe and Ni-oxides with a 0.5 μm-wide rim of submicron olivine; pyroxene; and Mg, Al-silicate glass (Fig. 25). Little to no fine-grained debris was observed along the track. An EDX raster obtained from a microtome slice of the TP shows that its bulk composition is ~chondritic (to within a factor of ~3×) when normalized to Mg for the elements Al, Si, P, K, Ca, Cr, Mn, Fe, and Ni. Detailed imaging, EDX analyses, and diffraction patterns have shown that the core is composed of three minerals: hematite, Fe-Ni

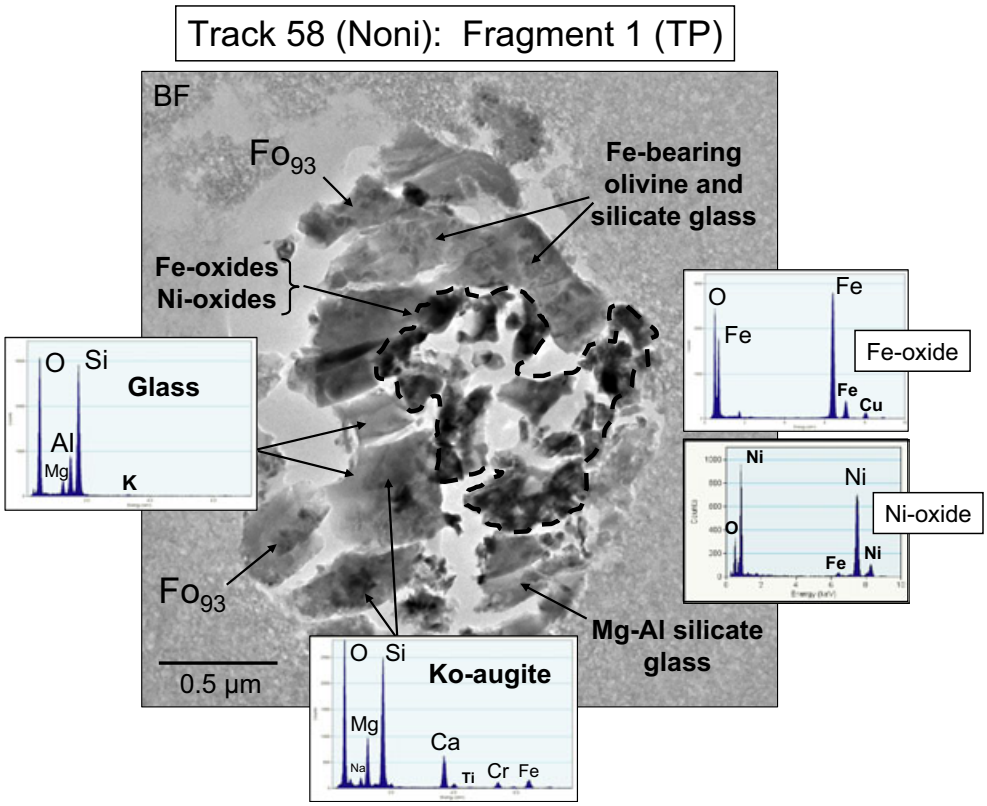

Fig. 25. Bright-field image of microtome slice of terminal particle from track 58 (Noni). This fragment consists of a core of Fe- and Ni-oxides surrounded by a shell of sub-100 nm sized grains of FeO-bearing olivine, Mg-Al silicate glass, and occasional kosmochloric augite (Ko-augite). The TP was present in the second-shortest (0.29 mm) type A track studied.

spinel, and the Ni-oxide bunsenite. Of these oxides, hematite is the modally dominant phase and forms platy Ni-free crystals up to 200 nm in size, which are in sharp contact with the FeO-bearing olivine and silicate glass. The phase is a very pure Fe-oxide (Table 9, ref 687), although a trace amount of S and P was noted in a few analyses. Measurements of several reflections from a minor zone axis diffraction pattern are very close to those given for hematite from the JCPDS pattern 13-534 (Bayliss et al. 1980). Also present in the core region is a Fe,Ni-oxide, which typically occurs as equant crystals less than 100 nm in size. Careful EDX measurements show that its Fe/(Fe + Ni) ratio varies from 0.67 to 0.71. Up to 6.2 wt% CoO was measured in this phase. Diffraction patterns are consistent with a spinel crystalline structure confirming the mineral trevorite ($FeNi_2O_4$) (Table 9, ref 693). Subsolidus equilibrium experiments in the Fe-Ni-O system indicate that hematite and trevorite are expected equilibrium phases during cooling between 1000 and 1200°C at oxygen partial pressures above pO_2 of 10^{-8} (Rhamdhani et al. 2008). We also observed the Ni-oxide bunsensite (Table 9, ref 696) occurring as small crystals (< 50 nm) typically associated with the exterior of the core region and often decorating FeO-bearing olivine. No diffraction patterns were taken from this phase. Bunsenite, in association with trevorite spinel, is an expected assemblage in Fe-Ni-O systems in the temperature range of 1000–1200°C, with oxygen partial pressures $>10^{-8}$ and Ni/(Ni + Fe) ratios $>\sim$0.3 (Rhamdhani et al. 2008). The presence of Fe and Fe,Ni oxides is very unusual and we are unsure of their origin in this fragment. It is possible that laboratory weathering or exposure of the microtome slices to water during ultramicrotomy produced at least some of these oxides.

The shell of the TP contains a mixture of FeO-bearing olivines, Mg + Al-silicate glass (Table 6, ref 226), and occasional Ko-augite grains (Fig. 25). Although we were unable to obtain pure olivine compositions due to its intimate association with the glass, EDX spectra largely obtained on olivine show that the olivine grains are approximately $Fo_{88–93}$ in composition. Occasional kosmochloric augites are also observed (Fig. 25; Table 4, ref 686).

In summary, track 58, the shortest track in this study, was produced by a ~8 µm impactor that did not fragment during collection. The TP is composed of a core of Fe- and Ni-oxides encased in a shell of silicates,

Table 9. Representative chemical compositions of Wild 2 oxides (normalized oxide wt%).

Track no.	58	58	58	77	141
Name	Noni	Noni	Noni	Puki	Coki
Frag	1(TP)	1(TP)	1(TP)	3	3
Phase	Hem[a]	Trev	Bun	Spn	Spn
Ref	687	693[a]	696	253	331
SiO_2	0.52	12.78	2.90	1.52	3.12
TiO_2	b.d.	b.d.	b.d.	2.70	0.76
Al_2O_3	b.d.	b.d.	b.d.	25.52	8.84
Fe_2O_3	99.12	56.96	–	–	–
FeO	–	–	2.12	38.03	24.25
MgO	b.d.	1.40	1.71	3.76	6.99
MnO	b.d.	b.d.	b.d.	b.d.	b.d.
CaO	b.d.	b.d.	b.d.	b.d.	0.14
NiO	b.d.	22.08	92.12.	b.d.	b.d.
CoO	b.d.	6.17	b.d.	b.d.	b.d.
P_2O_5	0.35	0.49	0.74	b.d.	b.d.
			Cation formulas		
Si	0.014	0.442	0.034	0.049	0.449
Ti	b.d.	b.d.	b.d.	0.066	0.019
Al	b.d.	b.d.	b.d.	0.973	0.346
Fe^{3+}	1.968	1.482	–	–	–
Fe^{2+}	–	–	0.021	1.029	0.673
Mg	b.d.	0.072	0.030	0.181	0.346
Mn	b.d.	b.d.	b.d.	0.002	b.d.
Ca	b.d.	b.d.	b.d.	b.d.	0.005
Ni	b.d.	0.614	0.864	b.d.	b.d.
Co	b.d.	0.171	b.d.	b.d.	b.d.
P	0.008	0.014	0.007	b.d.	b.d.
Total	1.990	2.796	0.955	3.024	2.958

Cation formulas based on 1, 3, or 4 oxygens for bunsenite, hematite, and trevorite/spinel, respectively.

Hem = hematite, Trev = trevorite, Bun = bunsenite, Spn = spinel, b.d = below detection.

[a]Ferric iron assumed. All analyses include small to moderate amounts of silicate. 0.04 atom% S not included in ref 687, 0.19 atom% S not included in ref 693.

which are dominated by MgO-rich olivines with Mg-rich silicate glass and occasional augite. The observed minerals in the TP are unusual and the nature of the fragment is unclear.

Track 59 (Naomi)

Track 59 is a short 350-μm-long type A track—marginally transitional to type B—containing two distinct optically opaque fragments (fragments 1 and 2) with moderate amounts of SiO_2 phases (glass and compressed aerogel) distributed along most of the track length (Fig. 1a). A third fragment (fragment 3, not shown in Fig. 1a) is present at the end of a 120 μm-long parallel track located 50 μm from the center of the main track. We studied fragments 1 and 2 from the main track, but have not yet extracted fragment 3.

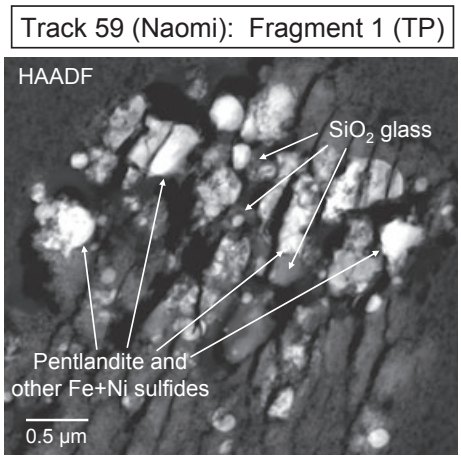

Fig. 26. HAADF image of a microtome slice of the terminal particle from track 59 (Naomi) showing physical disaggregation of fragment during capture. The bright angular to round grains are Fe,Ni sulfides (largely pentlandite), while interstitial and surrounding medium gray regions are pure SiO_2 glass believed to be derived from silica aerogel melt during capture. Pronounced dark fractured regions running NE-SW are likely from microtoming.

The TP (fragment 1) with an apparent size of ~3 μm is composed of a mixture of Fe-Ni sulfides of variable Fe/Ni ratios intimately mixed with pure silica glass (Table 6, ref 559), believed to be aerogel melt (Fig. 26). The Fe-Ni sulfides form discrete grains ranging from sub-spherical to nearly rectangular in shape. Many have a composition consistent with the mineral pentlandite (Table 5, ref 281) although the range of Fe/(Fe + Ni) ratios is highly variable and spans values from 0.32 to 0.92 (Joswiak et al. 2009). The bulk composition of the sulfide obtained from summing EDX spectra from element maps is consistent with pentlandite. Fragment 2 is present in a short side track approximately halfway between the entrance hole and the TP, and is composed of grains with similar textures and mineralogy to the TP, indicating separation of the original impactor into two discrete fragments. The rounded morphologies of the Fe-Ni sulfides; their large range of Fe/Ni ratios; their bulk composition, which is consistent with pentlandite; and the pure SiO_2 glass surrounding the sulfide grains suggest melting of an impacting pentlandite particle followed by separation of sulfide melt globules. The immiscibility of sulfide and silicate melts is evident from the texture visible in the microtome slices. In summary, the projectile that produced track 59 appears to have been composed of a 7 μm Fe-Ni sulfide (probably pentlandite) that melted during impact and recrystallized into subgrains of Fe-Ni sulfides of variable Fe and Ni compositions. This track and its fragments will be discussed further in a future publication.

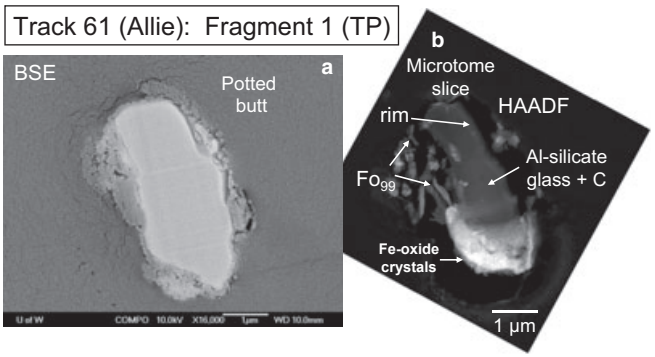

Fig. 27. a) BSE image of potted butt of TP from track 61 (Allie). Bright central core is composed of Al-silicate glass (minor Cr and Fe) and is surrounded by grains of forsterite, taenite, Fe-oxides, and unidentified Mg- and Al-bearing silicates. b) HAADF image of microtome slice from Allie showing silicate glass core and other phases on exterior. Bright region at the bottom of TP is composed of acicular Fe-oxide crystals believed to have formed during preparation in the laboratory. The origin of this fragment is unclear.

Track 61 (Allie)

Track 61 is a 1.6-mm-long classic carrot-shaped type A track with an optically opaque TP (Fig. 1a). Two small but distinct fragments are located in short side tracks at approximately one quarter and one half of the distance to the TP (Fig. 1a). Optical examination of the track suggests that tiny amounts of fine-grained debris may be present along its length. We embedded the lower portion of the track containing the TP, but have not yet studied the other fragments or the fine-grained material.

The TP is an elongate largely amorphous fragment approximately 5 µm long and 3 µm wide (Fig. 27). Imaging combined with EDX spectra shows that the fragment core is composed of an Al-rich silica glass with smaller quantities of Cr and Fe (Table 6, ref 560). A distinct 200 nm wide bright rim surrounding the glass, visible in HAADF images, is enriched in Fe. Surrounding the amorphous core is a complex mixture of smaller grains including Fo_{99} olivine (Table 3, ref 561) and probable Fe-Ni metal (taenite). The morphology of the olivine crystals suggests that they were in direct contact with the central core prior to microtoming. A distinct envelope of Fe-oxide crystals is present along one end of the fragment (Fig. 27b) and may be a product of oxidation from contact with water during microtoming. Small Fe-oxide crystals observed in other portions of the rim may also be oxidation products or pieces from the large Fe-oxide envelope that were displaced during cutting. We do not yet understand the nature of this fragment.

Track 77 (Puki)

Track 77 is a type B track >1.2 mm in length containing >54 discrete fragments distributed throughout the bulb region, along the main track and in 3 short side tracks (Fig. 1b). The track was extracted from the side of an aerogel tile and is incomplete because a portion of the aerogel containing the bulb of the track was missing and may have been lost. Other than the TP, the largest fragments were generally found at the ends of side tracks, although some large fragments were also present in the bulb region. Significant MSG, often observed as optically dark clumps, occurs throughout the track particularly near the base of the bulb and in the upper half of the main root. Most of the large fragments have partial or complete rims composed of silica aerogel melt and/or MSG. From a study of 53 random fragments from the roots and the bulb portions of the track, Ogliore et al. (2010), using Fe-XANES, measured the total fractional abundances of oxidized and nonoxidized Fe. These results indicate that the ratios of Fe^0:Fe sulfide:oxidized Fe phases are 0.16:0.36:0.48, suggesting that nearly half of the Fe in the track is in oxidized Fe phases.

We studied the TP and 28 additional fragments. Microtome slice and potted butt images of 13 representative fragments are shown in Fig. 28. Single mineral fragments were the dominant fragment type in the track with 15 consisting of the mineral olivine. The olivine fragments have a wide range in Fe/Mg ratios (see Table 3 for compositions of representative olivines from the track). Fragments 3, 4, and 107 have the most FeO-rich compositions (fragment 3 = Fo_{52}, Figs. 28e–f; fragment 4 = $Fo_{58–61}$, Fig. 28j; fragment 107 = Fo_{54}; no figure shown), whilst fragments 6, 50, and 104 are all nearly Fe-free. In these latter olivines, MnO is >FeO and therefore they are LIME olivines (See Fig. 28i, fragment 104). All three LIME olivines are collinearly aligned in the track, suggesting their derivation from a single larger grain which fragmented during capture. A single 200 nm Al-rich chromite spinel was found in sharp contact with the olivine in fragment 3 (Table 9, ref 253). EDX measurements of the remaining olivine fragments show that they are more intermediate in their Fe/Mg ratios. Fragments 7, 114 (Fig. 28o), and 116 are composed of single $Fo_{61–72}$, $Fo_{86–90}$, and Fo_{76} olivine grains, respectively. In track 77, MgO-rich olivines were commonly found in the bulb region rather than lower portions of the track, i.e., the roots. It is not clear if this is significant to the impactor morphology or simply fortuitous.

Five fragments in track 77 are composed of monomineralic pyroxenes of which three (fragments 108, 111, and 112 [Fig. 28p]) are low-Ca pyroxenes (Table 4, refs 581 and 592). Fragment 108 ($En_{99.6}Wo_{0.1}$) has a

Track 77 (Puki): Fragment 1 (TP)

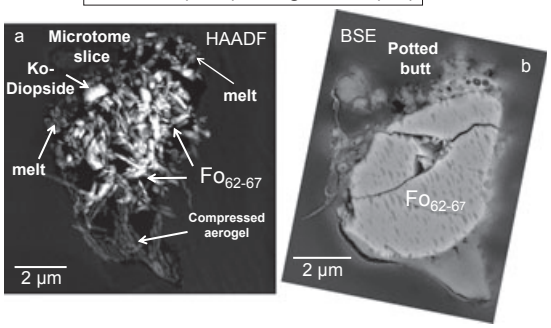

Track 77 (Puki): Fragment 2

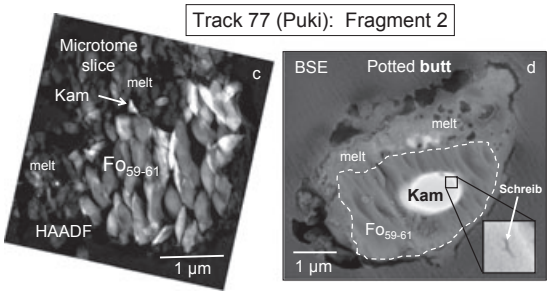

Track 77 (Puki): Fragment 3

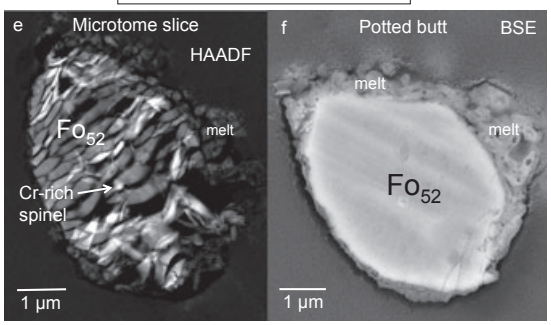

Track 77 (Puki): Fragment 5

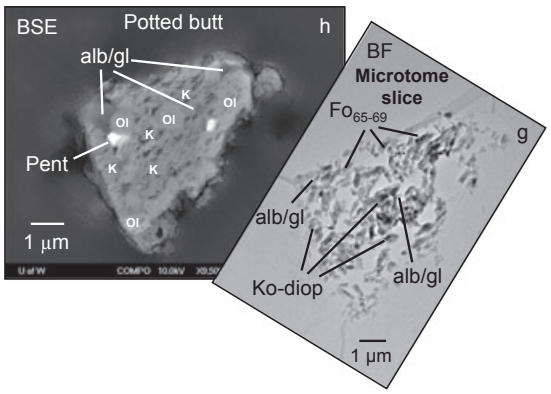

Track 77 (Puki): Fragments 4, 8, 9 and 104

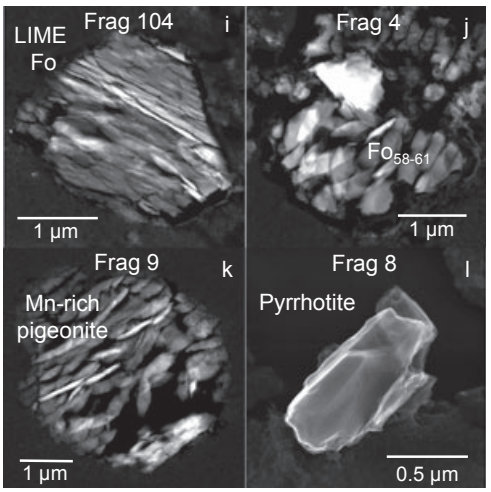

Track 77 (Puki): Frags. 51, 53, 112 and 114

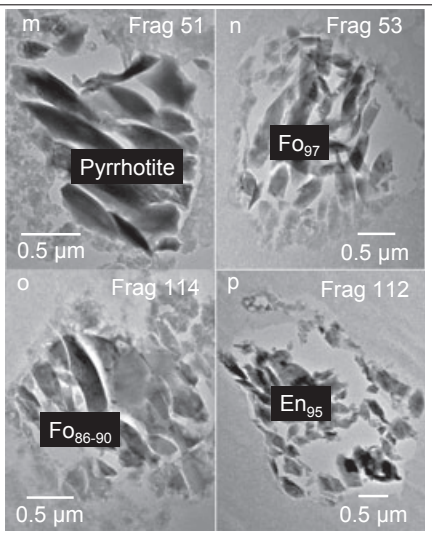

Track 77 (Puki): Fragment 113

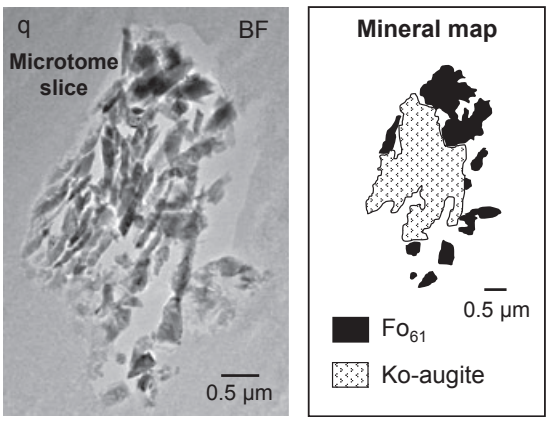

Fig. 28. Images of 13 fragments studied in track 77 (Puki). a, b) Oriented HAADF and BSE images of microtome slice and potted butt of TP, which is largely composed of $Fo_{62–67}$. A single kosmochloric diopside is also visible. Significant aerogel melt surrounding the periphery is visible in both images. Fractures in BSE image are likely due to microtoming. c, d) HAADF and BSE images of microtome slice and potted butt of fragment 2. The fragment is composed of equilibrated Fo_{60} containing a single large egg-shaped kamacite grain. A small ribbon of schreibersite is visible in the interior of the kamacite (inset). A small piece of kamacite, apparently displaced from its original location, is visible in the HAADF image. Significant vesicular aerogel melt can be seen surrounding large portions of the perimeter. e, f) Oriented HAADF and BSE images of microtome slice and potted butt of a large single grain of equilibrated Fo_{52}. A small Cr-rich spinel is present in the center of the grain. Vesicular silica melt surrounds most of the fragment. g, h) Oriented bright-field and BSE images from the microtome slice and potted butt of fragment 5. The fragment is dominated by a mixture of FeO-rich olivine and kosmochloric diopside with smaller amounts of albitic feldspar, which is transitional to feldspathic glass. Single occurrences of pentlandite and a Ni-bearing Fe-sulfide are visible in the potted butt image. i–l) Single grain of LIME forsterite (fragment 104), equilibrated $Fo_{58–61}$(fragment 104), Mn-rich pigeonite (fragment 9), and a single pyrrhotite crystal (fragment 8) found as isolated grains in the track bulb. All are HAADF images except (l) which is a SE image. m–p) Small Fe-sulfide (fragment 51), olivine (fragments 53 and 114), and enstatite (fragment 112) fragments from the bulb region of the track. q) Bright-field microtome slice and mineral map of a Kool grain (fragment 113) found in the bulb region. Fragment is composed of FeO-rich olivine and kosmochloric augite. Locations of all fragments in the track are shown in Fig. 1b. Ko-diopside = kosmochloric diopside, kam = kamacite, schreib = schreibersite, Fo = forsterite, En = enstatite, alb/gl = albite/glass, pent = pentlandite, LIME = low-Fe, manganese-enriched, melt = silica aerogel melt.

higher Mg content, but lower Ca contents than fragments 111 and 112, which are compositionally similar to one another ($En_{92.8}$, $Wo_{2.1}$; $En_{92.9}$, $Wo_{2.3}$, respectively). It is possible that fragments 111 and 112 were siblings that were derived from a single larger parent as suggested by their close physical proximity in the track and their similar chemical compositions. All the pyroxene fragments were present in the middle to lower portion of the bulb. One Na + Cr-bearing augite (fragment 110, not shown) was observed as an isolated grain with apparent size of 0.6 μm in the middle portion of the bulb. An EDX analysis showed that it contains 3.5 wt% Na_2O and 4.9 wt% Cr_2O_3 and has an atomic Mg/(Mg + Fe) ratio of 0.75 (Table 4, ref 583). Finally, a fifth fragment (fragment 9; Fig. 28k) is a compositionally unusual Ca-bearing pyroxene (Table 4, ref 477) composed of Mn-rich pigeonite (transitional to augite). Containing up to 12.3 wt% MnO, this grain appears to have been shocked based on a high density of fractures, subgrains, possible mosaicism, and disarticulated diffraction ring patterns. No other fragments studied in track 77 display similar features. Its round shape is likely a result of abrasion during capture and not from melting. Up to ~1 wt% Na_2O and K_2O were measured in the fragment.

Two discrete Fe-Ni sulfide fragments were found in the track. The first, fragment 8 (Fig. 28l), is a euhedral grain with crystal faces approximately 1 μm in length. This fragment was present near the top of the main root and is associated with significant amounts of fine-grained debris. The second Fe-Ni sulfide fragment (fragment 51; Fig. 28m) is morphologically distinct from fragment 8. It is relatively round on one end, at least 2 μm in size, and does not have the obvious crystal faces present in fragment 8. Compositionally, however, both grains have atomic (Fe + Ni)/S ratios close to 1.0 (see Table 5 for analyses of fragment 8, ref 551 and fragment 51, ref 527) and relatively high Ni contents (fragment 8 = 1.3 wt% Ni; fragment 51 = 0.85 wt% Ni). No diffraction patterns were obtained to confirm particular Fe sulfide crystal structures.

Although most fragments in Track 77 are single mineral grains, at least five are composed of two or more phases. Four fragments are Kool grains. Of these, fragment 5, a relatively large (> 5 μm) sub-terminal particle from the second longest root, contains a mixture of $Fo_{65–69}$ (Table 3, ref 402), Ko-diopside or augite, poorly crystalline albite, and single occurrences of pentlandite and another Ni-bearing Fe sulfide (Figs. 28g and 28h). Up to 4.7 wt% Na_2O and 8.7 wt% Cr_2O_3 were observed in the high-Ca pyroxene (Table 4, ref 557). Three additional Kool grains (fragments 52, 102, and 113) smaller in size were observed in the bulb (fragment 113 is shown in Fig. 28q). It is uncertain whether the latter fragments were previously attached to fragment 5 or were distinct separate grains in the original particle. Finally, fragment 2, an FeO-rich olivine ($Fo_{52–61}$) with a prominent kamacite core was lodged in the main root halfway between the base of the bulb and the TP (Fig. 28d). The fragment is embedded in a significant amount of vesicular silica aerogel melt and MSG. The oval-shaped kamacite inclusion is at least 1 μm long and itself contains an inclusion of schreibersite. We did not find the kamacite present in the interior of the olivine in any of the prepared microtome sections; however, a 0.5 μm shard of kamacite near the exterior of a microtome section was found. It is not clear whether the shard was a small piece of the interior kamacite that was displaced during microtoming or part of a different metal grain located near the fragment rim. An EDX analysis of this metal shard is given in Table 8 (ref 553). Likewise, we did not observe schreibersite in any microtome sections of fragment 2. However, a single broken shard of schreibersite was observed in fragment 3 and analyzed by EDX (Table 8, ref 57). A diffraction

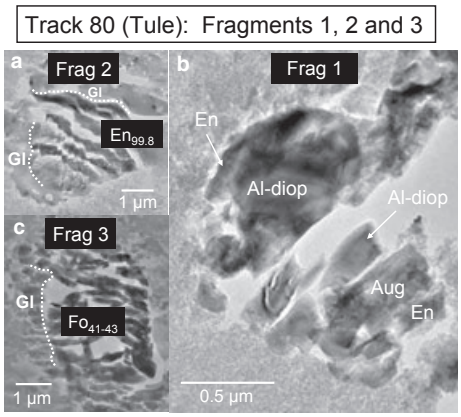

Fig. 29. Microtome slices of three fragments from Track 80 (Tule). a) Isolated enstatite grain in bulb region of track. Dotted lines on exterior delineate sharp edge of enstatite with Fe-Mg-Al-Ca silicate glass (minor Cr and alkalies). b) Refractory fragment composed of Ti-bearing aluminous diopside, augite, and En_{99}. c) FeO-rich olivine grain with moderate amounts of Fe-Mg-Al-bearing silicate glass. Gl = silicate glass, diop = diopside, Aug = augite, En = enstatite, Fo = forsterite.

pattern taken on the [001] zone axis is consistent with the schreibersite crystal structure. Fragments 2 and 3 were in close proximity to one another in the main root; therefore, these fragments are believed to formerly have been part of a single larger grain.

In summary, track 77 contains a diverse mixture of mineral (olivine, enstatite, high-Ca pyroxene, pyrrhotite, Na-rich feldspar) and rock fragments (Kool grains, olivine + Fe,Ni metal) and MSG. The wide dispersal of fragments observed throughout the bulb region and in the multiple roots, along with the abundant MSG, suggests that the impactor that produced track 77 was a loosely bound unequilibrated aggregate of coarse grains possibly with significant fine-grained matrix.

Track 80 (Tule)

Tule is a classic type C track expressing a wide bulbous cavity above two narrow and relatively short roots (Fig. 1b). The track bulb has the greatest width/length ratio and second longest overall length (4.7 mm) of all the tracks in this study. We observed three large fragments from the track bulb located approximately midway between the entry hole and the bulb base. We did not examine any of the fragments present at the ends of the roots.

Images of microtome sections from the three fragments we observed are shown in Fig. 29. Fragment 1 is composed of several pyroxenes including a refractory aluminous diopside, a low-Al augite and enstatite (En_{99}), which appears to form rims on both of the high-Ca pyroxenes. EDX measurements of the aluminous diopside show that it contains up to 7.8 wt% Al_2O_3 (Table 4, ref 194). The phase has a very low Fe content (Fe/(Fe + Mg) = 0.002) and relatively high concentrations of Ti (TiO_2 = 1.2 wt%) and V (V_2O_5 = 0.67 wt%), indicating its refractory nature. Juxtaposed onto the aluminous diopside is augitic pyroxene of variable Wo content and low Al_2O_3 concentration (Table 4, ref 196). Small amounts of Mn and Cr were detected.

Fragment 2 is a discrete >1 μm very pure enstatite ($En_{99.6}$). Concentrations of the elements Al, Ca, Cr, and Fe are all very low while Ti and Mn are below detection limits (Table 4, ref 204). The composition of enstatite in this fragment is similar to the enstatite that partially rims fragment 1, suggesting that these fragments may have previously been attached to one another prior to collection. A distinct glass rim, approximately 200 nm-wide surrounds much of the fragment (Table 6, ref 205). Moderate amounts of Na, Al, K, Cr, and Mn imply a more complex origin for the glass than simple interaction between the enstatite and silica aerogel during capture heating.

Fragment 3, a 3×4.5 μm olivine, is the largest fragment we studied in track 80 (Fig. 29c). Consisting of $Fo_{41–43}$, this olivine was one of the most FeO-rich olivines we found in this study (Table 3, ref 200). It is relatively rich in the minor elements Ca (CaO = 0.32 wt%) and Mn (MnO = 0.71 wt%). A 0.75μm-wide glass rim with moderate abundances of Mg, Al, and Fe is present on one side of the fragment.

Several microtome sections containing coarse fragments from the bulb area of track 80 were examined by Stodolna et al. (2010) who reported large compositional ranges in both olivine ($Fo_{40–100}$) and pyroxene ($En_{50–98}$, $Wo_{0–45}$) fragments, which together constituted 85% of the total coarse fraction. Magnetite, cristobalite, Fe-Ni sulfides, and other phases were also reported.

In summary, track 80 is composed of a mineralogically heterogeneous mixture of unequilibrated coarse grains and abundant MSG. The high width/length ratio of the track and lack of a dominant central main root suggest that the impactor did not contain unusually large and structurally competent fragments. Instead, the morphology and mineralogical characteristics of track 80 are consistent with an impactor composed of diverse subequal-sized coarse grains and possible fine-grained matrix.

Track 130 (Bidi)

Track 130 is a narrow type A carrot-shaped track 1.3 mm in length with maximum width of 60 μm (Fig. 1a). The track is remarkably free of debris and only

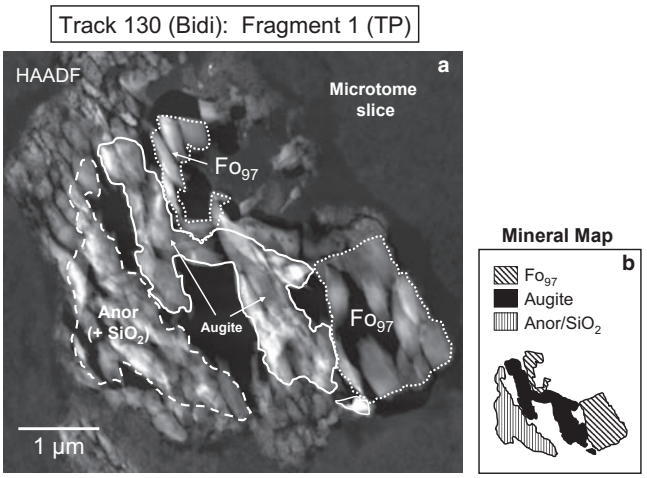

Fig. 30. a) HAADF image of a microtome slice from track 130 (Bidi) TP. Fragment is composed of (apparently) layered Fo_{97}, Al- and Ti-rich augite, and anorthite (with domains of SiO_2 glass) and is likely an Al-rich chondrule fragment. Significant vesicular aerogel melt is present around the exterior of the particle. b) Simplified map of (a) showing possible layer texture. Fo = forsterite, Anor = anorthite. White regions in interior of mineral map are void spaces where minerals where plucked during microtoming.

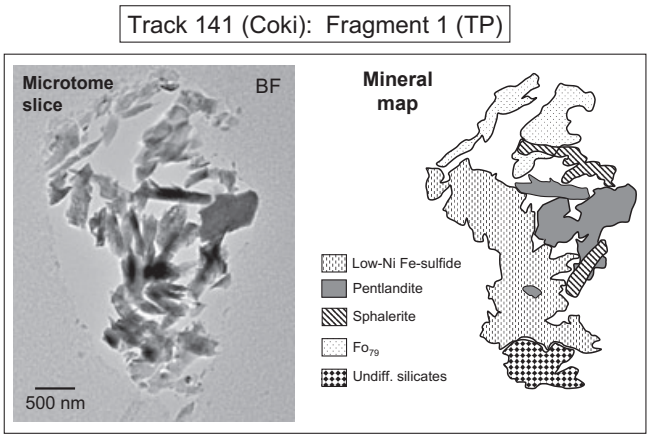

Fig. 31. BF image and mineral map of a microtome slice of the TP from track 141 (Coki), which is dominated by the three sulfides pentlandite; sphalerite; and low-Ni, Fe-sulfide. A large olivine grain (Fo_{79}) is present at the top of the TP, while a mixture of submicron FeO-rich olivine, Ko-augite, and Al-Mg+/-Ca silicate glass is present at the bottom. Interior white regions in the mineral map represent void spaces where minerals were plucked during microtoming.

the 5 μm TP and a few submicron- to micron-sized grains, located ~0.3 mm from the entry hole, are present. TEM analyses show that the TP is an assemblage composed of olivine, high-Ca pyroxene (augite), and anorthite (Fig. 30). A vesicular SiO_2 glass, presumed to be melted aerogel, surrounds much of the fragment. No MSG was observed. The measured forsterite contents of the olivine fall within the narrow range of $Fo_{97–98}$, suggesting that this phase is equilibrated with respect to Fe and Mg (Table 3, ref 374). Measured minor element abundances in the olivine indicate that the average Cr_2O_3 content is high (average Cr_2O_3 = 0.64 wt%) while MnO is unusually low (average MnO = 0.06 wt%). Electron diffraction patterns confirmed the olivine crystal structure (not shown). In microtome section and potted butt images, the augite appears to be sandwiched between olivine and anorthite. EDX measurements of the high-Ca pyroxene show a significant range of CaO contents (5.5–21.4 wt%), which spans the range from pigeonite to diopside, although the vast majority are augites. The spread in Fe/Mg ratios is, however, narrower with an average Fe/(Fe + Mg) = 0.03 (atomic) and standard deviation of 0.005 (Table 4, ref 468). Moderately high Al_2O_3 (1.7–8.0 wt%) and TiO_2 (0.8–1.7 wt%) contents in the augite indicate that this phase is relatively refractory. Up to 0.13 wt% V_2O_5 concentrations were also measured. The third phase, anorthite, is texturally unusual. In microtome sections, it was observed to always occur interlayered with an SiO_2 glass, which was up to 100 nm in width. In addition, rounded sub-50 nm Fe-rich inclusions, believed to be Fe metal, were found in the feldspar. The anorthite contents of the plagioclase range from An_{94} to An_{100}. The anorthite structure was confirmed by electron diffraction. Preliminary oxygen isotopic analyses showed that the TP may be an Al-rich chondrule fragment or altered amoeboid olivine aggregate (AOA) (Joswiak et al. 2010). More recent results, however, indicate that the fragment is more likely to be an Al-rich chondrule fragment than an AOA (in preparation).

In summary, track 130 was produced by a 9 μm Wild 2 particle composed of sub-equal amounts of Fo_{97} olivine, augite, and anorthite feldspar. These minerals along with oxygen isotopic compositions obtained on the TP suggest that it is an Al-rich chondrule fragment.

Track 141 (Coki)

Track 141 is a 1.8-mm-long classic type B track with an axially symmetric wide bulb above a single narrow root (Fig. 1b). Extending beneath the bulb, a 0.6-mm-long stylus contains an optically opaque TP and a large fragment (fragment 2) approximately one-third of the distance between the bulb base and the TP. A significant quantity of MSG is present in the track and was observed in most microtome sections. We studied the TP, and six additional large fragments located in the root and in the lower portion of the bulb.

The TP is dominated by a three-sulfide assemblage consisting of pyrrhotite, pentlandite, and Fe-bearing sphalerite (Fig. 31). The fragment is at least 3.5 μm in size

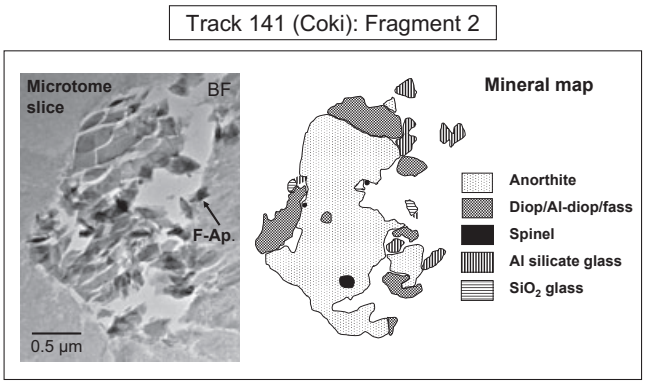

Fig. 32. BF image and mineral map of microtome slice of CAI-like fragment 2 from track 141. The fragment is dominated by anorthite and appears to have a discontinuous rim of diopside, Al-rich diopside, and fassaite. A small shard of fluorine-rich apatite (F-Ap) is indicated in the BF image, but not shown in the mineral map. White regions in the mineral map are void spaces where no minerals exist. This fragment is also discussed by Matzel et al. (2010). Diop = diopside, fass = fassaite.

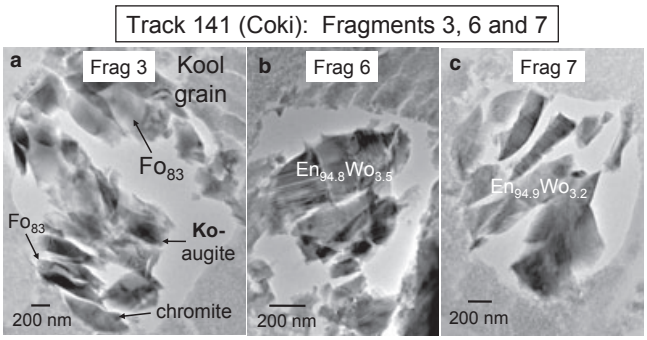

Fig. 33. BF images of fragments 3, 6, and 7 found in separate regions in the bulb of track 141. a) Fragment 3 is composed of a Kool grain and is discussed in the text and in Joswiak et al. (2009). b, c) Fragments 6 and 7 are single mineral grains composed of clino/orthoenstatite with minor amounts of Al, Ca, Cr, Mn, and Fe (see Table 4, ref 290 for an analysis of fragment 6). Similar major and minor element abundances suggest that fragments 6 and 7 were originally part of a single larger pyroxene grain prior to impact into aerogel.

and contains very little MSG around its perimeter. Typical EDX analyses of the pyrrhotite, pentlandite, and sphalerite are given in Table 5 (refs 541, 543, and 545). We note that a nearly identical 3-sulfide assemblage was also observed in track 10 (Arinna). A ~1 μm grain of olivine (Fo_{79}) (Table 3, ref 547) is present along one end of the fragment. EDX analyses of several shards (microtome produced) indicate that the olivine is uniform in composition. On the opposite end of the fragment, a population of submicron olivines ($Fo_{85–88}$) + kosmochloric augite + Mg,Al ± Ca silicate glass was found. These phases have a characteristic igneous texture.

Fragment 2 (Fig. 32) is the second refractory inclusion found in a Stardust track (see Simon et al. [2008] for details on Inti the first CAI fragment discovered). Suggested to be most closely associated with type C CAI's (Matzel et al. 2010), the fragment is composed of near end-member anorthitic plagioclase feldspar and smaller quantities of Al, Ti-rich diopside, which forms a partial rim around its exterior. The texture suggests that the pyroxene may have once surrounded much or all of the anorthite. It is possible that a significant portion of the pyroxene was stripped from the fragment during capture in aerogel. We did not observe pyroxenes with similar composition in other portions of the bulb, however. Two types of inclusions were observed in the anorthite, but were absent in the pyroxene. The first type is a relatively ubiquitous Cr-bearing spinel, which was often rounded and typically less than 100 nm in size. Rare 15–25 nm V,Nb-bearing inclusions were also observed. EDX spectra taken on the latter inclusions (+ host) contain Ca, Al, and higher than expected Si peaks for stoichiometric feldspar, suggesting that the inclusions were associated with a silica-rich phase in addition to the anorthite. A single ~0.5 μm fluorine-bearing apatite was found on the edge of one microtome slice. The nature of this grain and its relationship with fragment 2 is unclear. Mineral compositions of this fragment can be found in the online supporting material in Matzel et al. (2010).

Three fragments were studied from the very bottom portion of the bulb. Fragment 3, a 2 × 3 μm rounded Kool grain consists of FeO-rich olivine ($Fo_{83–85}$), Ko-augite, and poorly crystalline albite (Fig. 33a). EDX analyses of the olivine and pyroxene are provided in Table 3 (ref 313) and Table 4 (ref 365), respectively. This fragment is also discussed in Joswiak et al. (2009). Occasional Mg,Al-bearing chromite inclusions (Table 9, ref 331) were observed in the olivine. Fragments 6 (Fig. 33b) (Table 4, ref 290) and 7 (Fig. 33c) are relatively small isolated enstatite grains, both with Mg/(Mg + Fe) = 0.98. The fragments have partial platelet morphologies typical of low-Ca pyroxene, and were probably part of a single larger enstatite grain in the original impacting particle. Streaking along the [100]* direction shows that the pyroxenes are mixtures of ortho- and clino-enstatite.

To date, the only SiC observed in SD was found in this track (Messenger et al. 2009). Located in MSG melt in the base of the Coki bulb near fragment 6, the SiC has a triangular shape and is about 0.3 μm in size. Diffraction patterns indicate a cubic 3C β-SiC polytype. Isotopic work on the SiC grain by NanoSIMS indicates that it is rich in ^{13}C consistent with mainstream SiC grains typical of red giant and asymptotic giant branch stars (Messenger et al. 2009).

Table 10. Summary of coarse minerals and rock fragments observed in 16 SD tracks.

Total number of fragments	Assemblage	Number of fragments	
		Type A	Type B/C
Single mineral/phase fragments			
27	Olivine ($Fo_{41–100}$)	0	5
12	Enstatite ($En_{95–100}$)	1	6
4	Pyrrhotite	0	3
3	Fe,Ni metal	1	2
2	Feldspar	0	2
2	Augite	0	2
1	Cristobalite	0	1
2	Bulk glass	1	0
Rock fragments			
10	Chondrule fragment	5	2
1	Refractory inclusion	0	1
8	Kool grain[a]	1	4
1	Pyrrhotite + Fo_{97} + En_{97}	0	1
4	2 or 3 sulfide assemblage	1	2
11	Miscellaneous	5	4

Type A = type A track, Type B/C = type B or C track.
[a]Kool grain = kosmocholoric high-Ca pyroxene + FeO-rich olivine ± albite or glass ± spinel (Joswiak et al. 2009).

A small LIME forsterite (fragment 11, not shown) was observed in the lower portion of the bulb. EDX measurements on the fragment show that it has a MnO abundance greater than 3× its FeO content (Table 3, ref 710). Ca and Al concentrations in the olivine were near or below detection limits; however, a Cr_2O_3 abundance of 0.24 wt% was measured in one grain.

The last fragment we studied in track 141 was fragment 10 (not shown). Composed of the polycrystalline assemblage FeO-rich olivine ($Fo_{66–69}$), Ko-augite, and Al-silicate glass (minor Mg), the fragment is a Kool grain. Measured Na_2O and Cr_2O_3 contents of the Ko-augite were 2.3 and 3.3 wt%, respectively. Unlike fragment 3, a Kool grain located lower in the track (see above), the olivine in fragment 10 is richer in Fe, and does not appear to have albitic feldspar, but rather aluminosilicate glass. It is unknown whether fragments 3 and 10 were previously part of a single larger Kool grain or formed independently. A small 0.25 μm shard of pentlandite in direct grain boundary contact with Fo_{67} was observed in one microtome section. We note that FeO-rich olivine and pentlandite in close physical proximity were observed in the TP. It is not clear, however, whether fragment 10 has genetic links with the TP.

In summary, track 141 is composed of a diverse mixture of rock and mineral fragments and abundant MSG. The coarse-grained fraction, found distributed throughout the track, consists of a 3-sulfide assemblage, refractory inclusion, Kool grain, LIME forsterite, and En_{99} pyroxenes. The mineralogical diversity of the coarse fragments suggests that the Wild 2 particle was composed of unequilibrated rock and mineral grains. The large quantity of MSG may indicate that significant fine-grained materials were also present in the impactor.

DISCUSSION OF FRAGMENT TYPES

A summary of the number and types of mineral (and rock) fragments from all 16 tracks is provided in Table 10. Fifty-three of the 87 coarse fragments that we examined were composed of single mineral grains (or bulk glass), all others are polymineralic (rock) assemblages. The single mineral coarse fragments include 27 olivines (51%), 12 low-Ca pyroxenes (23%), 2 high-Ca pyroxenes (4%), 4 Fe sulfides (pyrrhotite or troilite) (8%), 3 Fe,Ni metal grains (6%), 2 feldspars (4%), and a single occurrence of crystalline SiO_2 (2%). It is likely that all these phases are primary materials that originated in Wild 2. Two fragments consisting of bulk silicate glass were also studied.

Single Mineral Fragments

An important question concerns the genetic relationships, if any, that exist between mineral fragments in individual tracks and between tracks. Were the various fragments in a particular track part of a single larger parent fragment or were they unrelated fragments simply residing near one another in their host particle or a mixture of the two? Shedding light on this question is important for reconstruction of the primary mineralogy of the Wild 2 particles and for improving our understanding of the materials that accreted into Wild 2 relative to those found in bodies that produced meteoritic samples. Major and minor element comparisons can provide evidence whether they were parts of single larger grains or were simply unrelated fragments.

Olivine

Olivine was observed as isolated single mineral fragments and in polyphase assemblages (rock fragments) in half of the type A and all type B and C tracks. In most of the type B and C tracks, single mineral olivine fragments were common, while in rock fragments, olivine was only infrequently observed. In type A tracks, olivine was always present in assemblages with other minerals and was never observed as single mineral fragments. The number of single mineral olivines that we studied ranged from a single occurrence in track 80 to 15 discrete fragments in track 77.

In some tracks, links between individual olivine fragments seem quite probable. In track 57, for instance,

olivine fragments 3 (Fig. 20) and 10 are single mineral olivine grains with Fo contents of Fo_{97} and Fo_{98}, respectively, and have similar Al_2O_3 and Cr_2O_3 abundances. Both are compositionally similar to the large olivine that is present in the terminal particle (fragment 1), which is part of an assemblage composed of pyrrhotite + Fo_{97} + En_{98} + fine-grained material (Fig. 19). It seems likely that these olivine fragments (fragments 1[TP], 3, and 10) were originally part of a single larger homogenous olivine grain.

In track 10, the three olivine fragments studied (fragments 4, 5, and 6; Figs. 3i–k) all have nearly identical Fe/Mg ratios, similar MnO and Cr_2O_3 contents, but somewhat different CaO abundances (0.0–0.35 wt%). Does this suggest that these fragments were once part of a single olivine grain zoned in CaO or perhaps part of two or three unrelated grains? In this track, the relationship between the olivine grains is not entirely clear. Likewise, the relationships between the olivine fragments in other tracks can be even more complex. In track 77, for example, 15 olivine fragments display a wide range in FeO abundances, with Fo contents ranging from Fo_{52} to Fo_{100}. It is unlikely that all fragments from this track were part of a single larger (zoned) parent grain as the large range in Fe/Mg ratios in a single grain is untenable. In fact, the FeO contents of the track 77 olivines appear to cluster in three regions: FeO < 3.3 wt%, 8 wt% < FeO < 18 wt% and FeO > 23 wt% (Fig. 34). In addition, some of the low FeO olivines in this track have high MnO contents (LIME forsterites) suggesting a fourth population. This may indicate that four or more discrete olivine fragments were present in the original Wild 2 particle. It is clear, however, that some of the olivine fragments in track 77 did separate from larger parent grains. Fragments 53 and 103, for instance, located in the middle and lower portions of the bulb, respectively, have identical Fo contents and comparable Ca, Cr, and Mn abundances. Similarly, fragments 2 and 4 have similar major and minor element compositions. Another example is track 41, where the three olivine fragments studied (fragments 2, 6, and 8) all have different Fe/Mg ratios and display widely ranging minor element abundances (Fig. 34), and thus appear to be genetically unrelated. The relationships between olivine fragments within individual tracks are complex; in some tracks, these minerals appear to have been derived from a single parent grain, while in other tracks, they appear to be unrelated.

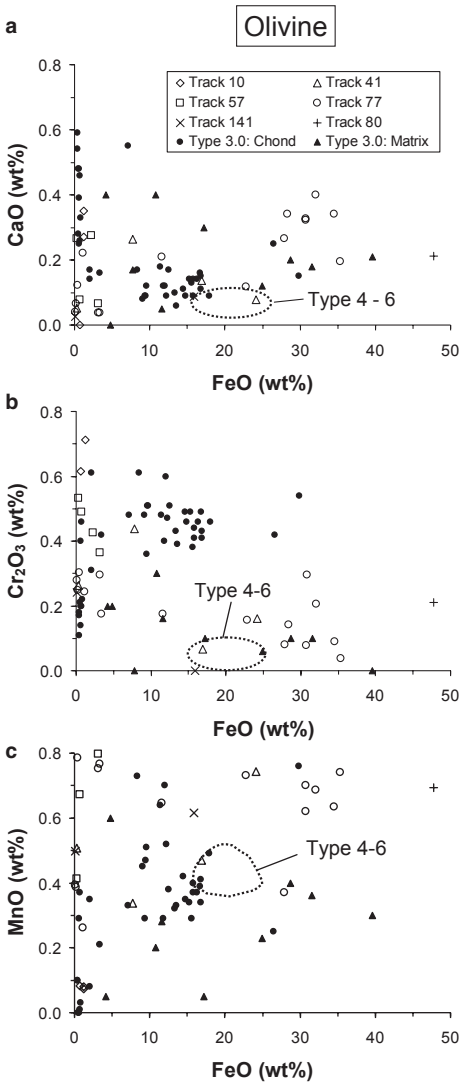

Fig. 34. Variation diagrams showing minor element compositions of Stardust olivine fragments versus FeO contents from the single type C and all type B tracks. Symbols shown in the legend in (a) apply to all three plots. Also plotted are olivines from chondrules from type 3.0 chondrites. Dotted outlines show compositions from olivines from equilibrated type 4–6 chondrites. The plots show that a large range of CaO, MnO, and Cr_2O_3 values are present in the SD olivines similar to olivines from chondrules and matrix in unequilibrated chondrites. Chondrule olivine data from Jones (1996), Huang et al. (1996) and Brearley and Jones (1998). Matrix olivine from Matsunami et al. (1990), Weisberg et al. (1997), and Alexander et al. (1989a).

LIME Forsterites

Four tracks (tracks 41, 57, 77, and 141) contain isolated monomineralic forsteritic olivine fragments with MnO > FeO, so called LIME olivines (Klöck et al. 1989), which may have formed directly from gas in the solar nebula (see condensate section, discussed later). A MnO versus FeO variation diagram of 8 fragments from the four tracks is shown in Fig. 35. Single fragments were found in tracks 41 and 141, and two tracks (tracks 57 and 77) contained 2 and 4 LIME olivine fragments, respectively. For comparison, LIME olivine compositions from CP IDPs and unequilibrated ordinary chondrites

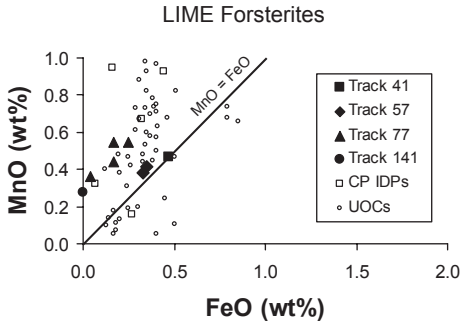

Fig. 35. MnO versus FeO plot for 8 individual LIME forsterite fragments studied in four SD tracks compared with LIME forsterites from CP IDPs and unequilibrated ordinary chondrites (Klöck et al. 1989). The plot shows that MnO > FeO for the SD olivines and that they directly overlap the central portions of the CP IDP and UOC fields. LIME forsterites are believed to be nebular condensates. Several of the SD olivine data points are averages from two to four analyses. CP IDP = chondritic porous interplanetary dust partice, UOCs = unequilibrated ordinary chondrites.

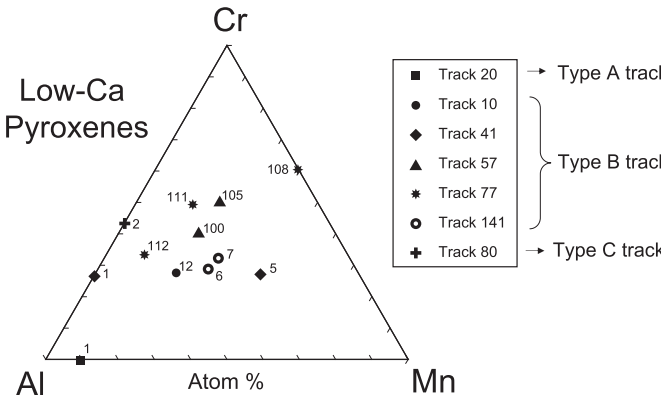

Fig. 36. Al-Cr-Mn ternary plot of 12 enstatite fragments from 7 SD tracks. The coarse enstatite fragments were observed in all three track types. The large scatter in the minor elements suggests different origins for the pyroxenes within tracks and also between tracks. Numbers next to symbols refer to individual fragment numbers from tracks (see Table 2).

(UOC), principally Semarkona (Klöck et al. 1989) are also shown in Fig. 35. The figure indicates that LIME olivines from the SD tracks have MnO abundances that fall midrange when compared with CP IDPs, and UOCs. Notably, we did not observe high abundances of Al, Ca, and Cr in the SD LIME olivine fragments. Measured average Al_2O_3, CaO, and Cr_2O_3 contents are 0.23, 0.08, and 0.30 wt%, respectively, from the 8 fragments. Multiple LIME olivine fragments may have separated from a single larger grain during collection in tracks 57 and 77. In track 77, this conclusion is supported by approximate physical co-linearity of the four observed fragments in the track. We also note that in all cases, the LIME olivines were observed as isolated single mineral fragments in their tracks.

Pyroxenes

Fragments composed solely of low-Ca pyroxenes comprise the second largest population of fragments (14%) observed in the tracks. This includes 11 monomineralic enstatite fragments from 6 type B/C tracks and a single enstatite from one type A track. Of these, five are Fe-poor with Mg/(Mg + Fe) > 0.99. Each is from a separate track. The remainder have Mg/(Mg + Fe) between 0.95 and 0.99. This is in contrast to the olivine fragments, which have much wider Mg/(Mg + Fe) ratios (see above). With the exception of track 20, all of the Mg-rich enstatite fragments occur in bulbous tracks, possibly indicating their association with fine-grained matrix in Wild 2 particles. The two low-Ca pyroxene fragments observed in track 141 (fragments 6 and 7) have nearly identical FeO, MgO, and CaO contents, and were both found near the base of the bulb, indicating a possible sibling relationship. Similarly, fragments 111 and 112 in track 77 have major element compositions that are nearly identical. Whether sibling relationships exist between low-Ca pyroxene fragments in tracks 41, 57, and 77 is less clear as their comparative FeO, MgO, and CaO abundances show larger variations.

An Al-Cr-Mn ternary plot of the 12 enstatite fragments is provided in Fig. 36. The figure shows that significant relative minor element scatter occurs between most of the enstatite fragments, even those from the same tracks. An exception is the two fragments from track 141 (fragments 6 and 7) whose minor element contents are very similar (Fig. 37). Interestingly, fragments 111 and 112 from track 77, which have nearly identical major element compositions, show relatively large differences in their minor element concentrations. In general, it appears that the different low-Ca pyroxene fragments within single tracks have widely varying minor element abundances, reflecting the unequilibrated nature of the pyroxenes that were present in the Wild 2 particles. In Fig. 37, we show low-Ca pyroxene abundance plots of the Al_2O_3, Cr_2O_3, and MnO oxides confirming these wide variations.

Correlations between Mn and Fe in some of the pyroxene fragments are observed. A plot of MnO versus FeO is shown in Fig. 38. The plot shows that the SD pyroxenes may plot along two distinct trends of different MnO/FeO ratios, shown by the dotted lines. The low MnO/FeO trend is defined by two relatively high FeO pyroxenes from tracks 27 (labeled 1 in the figure) and 57 (labeled 4), two pyroxene fragments from track 77 (numbers 6 and 7), and other low MnO and FeO pyroxene fragments that plot near the origin. A second more weakly defined trend is suggested by points with moderate-to-high MnO contents trending along a higher

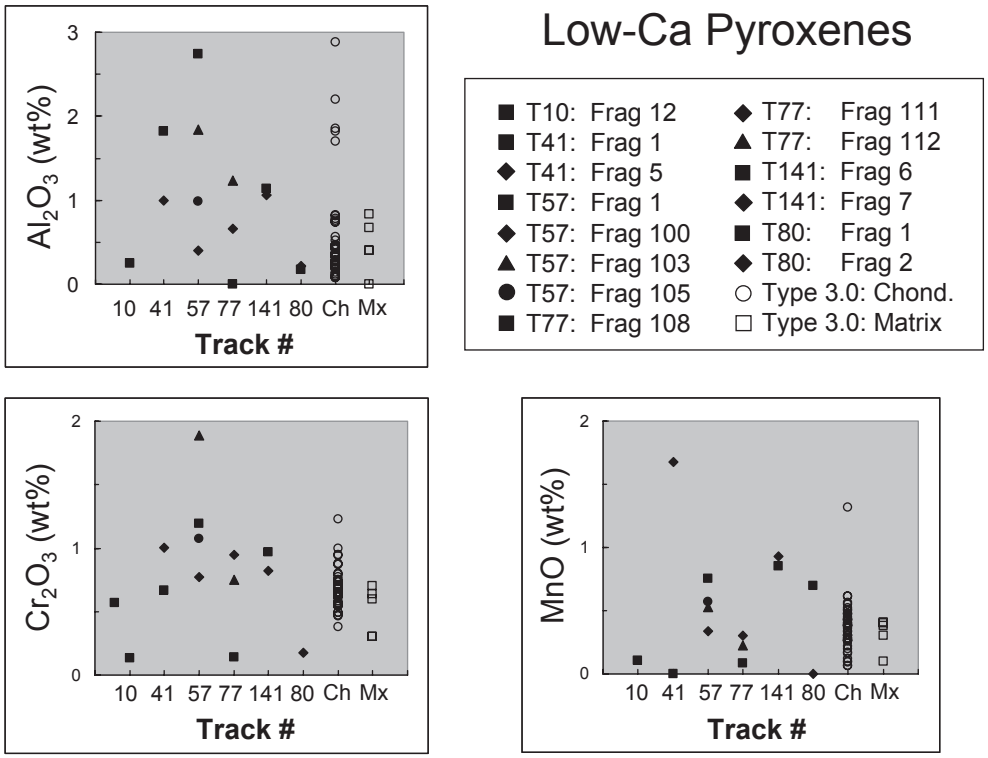

Fig. 37. Al_2O_3, Cr_2O_3, and MnO wt% of low-Ca pyroxenes from coarse fragments from five type B tracks and one type C track (track 80) compared with low-Ca pyroxenes from chondrules and matrix clasts in type 3.0 chondrites. The plots show large minor element variations between pyroxenes within individual tracks and between tracks and are similar to the range exhibited by the low-Ca pyroxenes from chondrules in Semarkona (LL3.0), indicating their overall unequilibrated compositions. Semarkona chondrule low-Ca pyroxene data from Huang et al. (1996), Jones (1994, 1996). Matrix clast low-Ca pyroxene compositions from Alexander et al. (1989). Ch, Chond = chondrules, Mx = matrix.

slope, which is largely defined by pyroxenes from three tracks. Also plotted in the figure are low-Ca pyroxenes from type I and II chondrules from Semarkona (LL 3.0) (Jones 1994, 1996) and matrix clast enstatites from chondrites of low petrologic types 3.0–3.2 (Alexander et al. 1989; Matsunami et al. 1990). The plot shows that the SD pyroxenes with low MnO/FeO ratios, the chondrule pyroxenes from Semarkona, and some matrix pyroxene clasts may follow a similar trend.

Only two fragments consisting solely of high-Ca pyroxene were present in all 16 tracks. Both fragments occur in track 77 and consist of unusual composition. Fragment 9 is an apparently shocked MnO-rich pigeonite/augite and fragment 110 consists of augite that is rich in the elements Na and Cr. High-Ca pyroxenes, however, are relatively common in the tracks in association with other minerals (rock fragments). A plot of the En-Fs-Wo components and all measured high-Ca pyroxene (as well enstatite) compositions is shown in Fig. 39.

Fe Sulfides

Wild 2 Fe sulfides are present in 14 fragments from 7 individual tracks (2 type A, 5 type B) and are plotted in the Fe-S-Ni + Co ternary diagram in Fig. 40. The figure indicates that the Wild 2 sulfides fall only in the pyrrhotite/troilite, pentlandite, or Fe sphalerite fields. Similar results for pyrrhotite/troilite and pentlandite were reported in Zolensky et al. (2008). Four Wild 2 coarse fragments are composed of monomineralic sulfides and six are mixtures of one or more sulfides including pyrrhotite (or troilite), pentlandite, and sphalerite. In addition, four fragments are composed of mixtures of Fe-Ni sulfides + silicate minerals. Ni concentrations amongst the sulfides vary widely within and between different fragments. Ni abundances in two EDX analyses, one from the TP in Arinna (track 10) and one from the TP in Coki (track 141), were below detection limits; all other Fe sulfides were Ni-bearing. The element Co was detected in about half of the Wild 2 pyrrhotites (average Co = 0.2 wt%), but was present in all measured pentlandites (average Co = 1.3 wt%). Thus, the Fe sulfides in Wild 2 are mineralogically, texturally, and compositionally diverse, which suggests that these minerals may have multiple origins. Pentlandite and pyrrhotite, for instance, are known to be low temperature products of hydration/oxidation

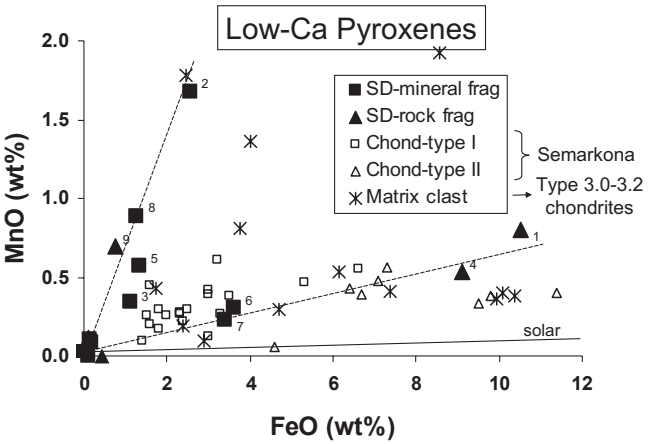

Fig. 38. MnO versus FeO wt% of low-Ca pyroxenes from 14 coarse fragments from nine SD tracks compared with low-Ca pyroxenes from Semarkona (type 3.0 chondrite) chondrules and matrix clasts from type 3.0–3.2 chondrites. The low MnO/FeO trend (dashed line) exhibited by the SD pyroxenes follows the trend observed in the chondrule and matrix pyroxenes. A high MnO/FeO trend (dashed line) may also be present in the SD pyroxenes. Numbers next to SD symbols refer to track and fragment numbers: 1 = track 27, frag 1; 2 = track 41, frag 5; 3 = track 57, frag 100; 4 = track 57, frag 103,; 5 = track 57, frag 105; 6 = track 77, frag 111; 7 = track 77, frag 112; 8 = track 141, frag 7; 9 = track 80, frag 9. Six SD symbols near the origin are: track 20, frag 1; track 56, frag 1; track 10, frag 12; track 41, frag 1; track 77; frag 108; track 80, frag 2. Type I and II chondrule pyroxene compositions from Jones (1994, 1996) and matrix pyroxene compositions from Alexander et al. (1989) and Matsunami et al. (1990).

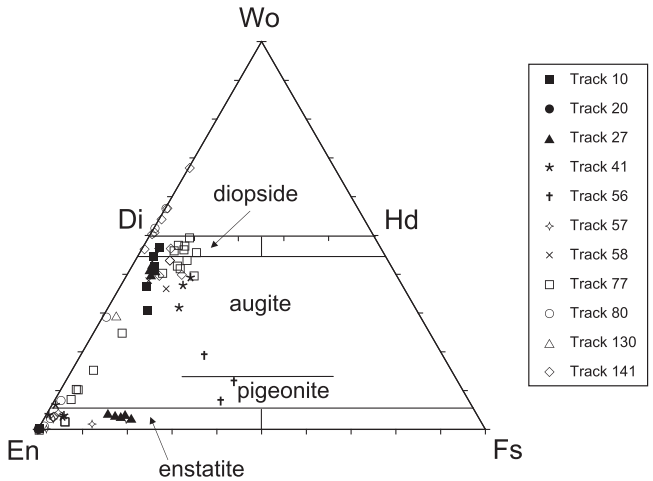

Fig. 39. Compositions of high- and low-Ca pyroxenes from 11 SD tracks. Some of the pyroxenes from tracks 80 and 141 plot above the quadrilateral due to their high concentrations of Al in octahedral sites.

reactions on CI parent bodies (Bullock et al. 2005). However, Fe-Ni sulfides are also observed associated with chondrules (Jones 1994), which formed at elevated

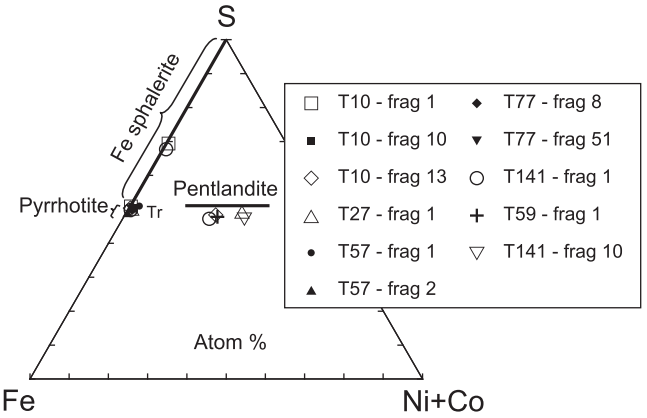

Fig. 40. Fe-S-Ni + Co ternary diagram showing compositions of the dominant sulfides observed in the SD tracks. These include pyrrhotite, probable troilite, pentlandite, and Fe-rich sphalerite. Overlapping data points that plot near troilite/pyrrhotite include track 10 – fragments 1, 10 and 13, track 27 – fragment 1, track 57 – fragments 1 and 2, track 77 – fragments 8 and 51, and track 141 – fragment 1.

temperatures and are nebular in origin. Thus, the origins of Wild 2 sulfides, which often lack critical context information (i.e., associations with other minerals), cannot unambiguously be determined.

Rock Fragments

Slightly more than one-third of all large fragments in the SD tracks are composed of more than a single mineral. Of the 35 rock fragments examined, 8 are Kool grains, 10 are possible chondrule fragments, and 4 are composed of mixtures of Fe-Ni sulfide minerals.

Possible Chondrule Fragments and Comparison to "Normal" Chondrules

A summary of 10 possible chondrule fragments that we found in 7 different tracks (5 type A, 2 type B) is provided in Table 11. Our chondrule fragment interpretation is based on mineralogical and textural similarities between the SD fragments and meteoritic chondrules. We suggest that ferromagnesian chondrules (both the Fe-poor type 1 and Fe-rich type 2), Si-rich chondrules, and Al-rich chondrules are all represented in Wild 2. Some of the fragments in individual tracks are probably siblings (fragments 7 and 8 from track 22; fragments 1 and 2, track 26); therefore, we interpret the 10 fragments to represent samples of 8 unique chondrules.

A clue that chondrules were melted in unrestricted environments is their spherical shapes. Unfortunately, this textural clue, if it was ever present, was lost in the SD fragments due to fragmentation and abrasion during capture modification. Some SD fragments do exhibit

Table 11. Summary of ten possible chondrule fragments observed in seven SD tracks.

Track type	Track number	Fragment number	Assemblage	Analogous chondrule types
A	22	7	$Fo_{67–68}$ + albitic glass	Type II ferromagnesian chondrule
A	22	8	$Fo_{60–88}$ + Al, Mg glass	Type II ferromagnesian chondrule
A	26	1	Fayalite + tridymite	Silica-rich chondrule (UOC)[a]
A	26	2	Fayalite + tridymite	Silica-rich chondrule (UOC)[a]
A	27	1	$En_{79–83}$ + Ko-augite + Pyrr + Pent	Type II ferromagnesian chondrule
A	56	1	Roed + Ko-augite + En + alk sil gls	Silica-roedderite chondrule (OC)[b]
A	130	1	Fo_{97} + augite + anorthite	Al-rich chondrule
B	57	1	Fo_{97} + En_{98} + pyrrhotite	Type I ferromagnesian chondrule
B	57	103	$Fo_{81–84}$ + $En_{87–89}$ + Fe,Mg,Al,Ca sil gls	Type II ferromagnesian chondrule
B	77	7	$Fo_{61–71}$ + Fe,Mg,Al,Na glass	Type II ferromagnesian chondrule

Ko-augite = kosmochloric augite, Pyrr = pyrrhotite, Pent = pentlandite, Roed = roedderite, alk sil gls = alkali silicate glass, sil gls = silicate glass, En = enstatite, Fo forsterite, UOC = unequilibrated ordinary chondrite, OC = ordinary chondrite.
[a]Brigham et al. (1986), Wasson and Krot (1994).
[b]Krot and Wasson (1994).

round external morphologies, but these shapes are not likely to be a result of melting during formation like chondrules, but are due to abrasion from tumbling during track deceleration in aerogel. Some fragments have such distinctive mineralogy and mineral compositions that links to counterparts from chondrites seem quite reasonable. The two large fragments from track 26 (Ada) (fragments 1 and 2) are composed of rounded tridymite nodules with partial to complete MnO-rich fayalite rims (Fig. 7) as previously described. These two fragments appear to have separated from a single intact object prior to impact into aerogel. Mineralogically, the two Ada fragments resemble rare chondrule fragments in type 3 unequilibrated ordinary chondrites (Brigham et al. 1986; Wasson and Krot 1994). In these meteorites, thin rims of MnO-rich fayalite surround nodules of very pure SiO_2 and are compositionally similar to the olivines in track 26. The actual mineral grain sizes are not significantly different between Ada and the UOC's as the Ada fragments are only 2 or 3× smaller than the observed chondrules (see Figs. 4 and 6 in Brigham et al. 1986). Texturally and mineralogically, these two SD fragments are strikingly similar to the silica + fayalite chondrules. One notable difference, however, is that low-Ca pyroxenes that are present in the chondrules/clasts in the chondrites appear to be absent in the SD fragments.

The TP from track 56 is another unusual SD fragment consisting of the rare mineral roedderite coexisting with Ko-augite, FeO-poor enstatite, alkali silicate glass and accessory amounts of silica and troilite (we cannot be certain that these accessory phases are primary). In rare alkali-rich silicate chondrules in L/LL 3.3-3.7 ordinary chondrites (OC), roedderite occurs with low-Ca pyroxene, feldspathic glass, silica, and FeO-rich olivine (Krot and Wasson 1994; Wood and Holmberg 1994). Complex models involving condensation and evaporation processes in the nebula were invoked to explain their origin. In the Krot and Wasson (1994) model, later parent body metasomatism + metamorphism was additionally inferred. Fayalitic olivine is absent in track 56, so if this TP had a similar origin as the OC chondrules, it must have evolved on a path that did not produce late-stage olivine. If the TP from track 56 formed in the nebula, then it must have been removed from its source region prior to coming into contact with FeO-rich vapors as advocated in the Wood and Holmberg (1994) model for the OC roedderite-bearing chondrules. If on a parent body, it would have to have been removed, presumably by impacts, prior to circulation of alkali- and FeO-rich fluids.

Five SD fragments (Table 11) are composed of FeO-bearing olivines ± low-Ca pyroxenes ± glass that mineralogically resemble type I or II ferromagnesian chondrules. Ferromagnesian chondrule-like fragments have been reported in other SD tracks (Nakamura et al. 2008; Bridges and Changela 2010; Butterworth et al. 2010; Gainsforth et al. 2010). In the present study, two fragments from track 22 and single fragments from tracks 57 and 77 (Table 11) are composed of FeO-rich olivine with smaller quantities of albitic or Mg,Al-rich silicate glass, phase assemblages that are similar to some chondrules. FeO-rich olivines with interstitial glasses (or mesostases) are the major phases in type II chondrules (Jones 1990), thus these four SD fragments mineralogically resemble type II chondrules.

The TP from track 27 is composed of a large equilibrated FeO-rich enstatite with smaller amounts of Ko-augite and Fe-Ni sulfides (Fig. 12). The clinopyroxene is present in two discrete locations on the fragment, which may have been connected prior to capture in aerogel. If so, this suggests that the Ko-augite formed a rim or partial rim on the low-Ca pyroxene. The texture is reminiscent of FeO-rich porphyritic olivine-

pyroxene chondrules in the Semarkona meteorite where augite exclusively occurs as overgrowths on low-Ca pyroxenes (Jones 1996). In Semarkona, however, the high-Ca pyroxenes are not enriched in Na and Cr. In the chondrules, the low-Ca pyroxene is typically clinoenstatite, the same polymorph as the TP enstatite of track 27. In addition, small rounded Fe-Ni sulfide grains (troilite) that are present in chondrule mesostases may be analogous to the rounded Fe-Ni sulfide in the SD TP (Fig. 12). We note that the (Fe + Ni + Co)/S ratio in the Fe sulfide in the SD TP is very close to unity and that both Ni and Co are low, consistent with troilite.

The TP from track 57 (fragment 1, Table 11) consists of olivine (Fo_{97}) in direct contact with enstatite (En_{98}), which together are attached to a much larger pyrrhotite (Fig. 19). It is likely that these grains were part of a larger olivine + pyroxene + Fe sulfide parent grain prior to collection by the Stardust spacecraft as we observed all three phases with nearly identical compositions in other portions of the track, indicating the rupturing of a larger fragment during capture. FeO abundances similar to olivine and enstatite in this fragment are also observed in co-existing olivines and pyroxenes in type I chondrules in UOCs as reported by Jones (1994). We note that opaque Fe,Ni metal and Fe-Ni sulfides are also present in the chondrules and that at least one Fe,Ni metal fragment was found in track 57.

Finally, the TP from track 130 (Bidi) has a bulk Al_2O_3 content of 10.1 wt%, and is composed of a refractory assemblage of subequal Fo_{97}, Al- and Ti-rich clinopyroxene and anorthite (Joswiak et al. 2010), and thus matches previously studied Al-rich chondrules (MacPherson and Huss 2005). High precision oxygen isotopes measured on olivine from the potted butt are consistent with Al-rich chondrules (manuscript in preparation).

Kool Grains

A frequent mineral assemblage observed in the tracks consists of FeO-bearing olivine with Na- and Cr-rich clinopyroxene (typically augite) ± poorly crystallized albite or alkali glass ± spinel. This assemblage has been referred to as a ''Kool'' grain (Ko = kosmochloric augite, ol = FeO-rich olivine) and was discussed by Joswiak et al. (2009). In the current study, at least 9 Kool grains from 5 separate tracks, including four type B and one type A, are present (Table 2). In Kool grains, Na_2O and Cr_2O_3 contents of the clinopyroxenes are typically elevated varying in these tracks from 0.7 to 6.0 wt% (average = 2.7 wt%) and 1.6–13.0 wt% (average = 4.7 wt%), respectively. Four Kool grain fragments from track 77 and two Kool grain fragments from track 141 appear to be siblings from parent grains that were separated during collection in aerogel. Because most Kool grains are found in mineralogically diverse type B tracks, Kool grains are most often associated with Wild 2 impactors that are composed of unequilibrated mineral assemblages.

Lithologies somewhat similar to Kool grains are found in R chondrites. In Rumuruti, for instance, the only known R group fall (Schulze et al. 1994), recrystallized clasts contain equilibrated FeO-rich olivines ($Fa_{38–40}$), high-Ca pyroxenes, and Na-rich plagioclase feldspar. The clinopyroxenes, however, contain less than 0.81 wt% Na_2O and and 0.97 wt% Cr_2O_3, levels that are typically much lower than clinopyroxenes in the SD Kool grains. Low-Ca pyroxene and metal are absent from both R chondrites and Kool grains. The high FeO contents of the olivines and lack of metal are evidence that both Kool grains and R chondrites formed in relatively oxidizing environments.

FeO-rich olivines in association with high-Ca pyroxenes are present in chondrules in UOC's, but they are compositionally and texturally very different than the SD Kool grains. In type II chondrules in the Semarkona (LL3.0), Chainpur (LL3.4), and Parnallee (LL3.6) meteorites (Jones 1996), augites were shown to occur as overgrowths on low-Ca pyroxenes, a texture and mineral association not observed in the Kool grains as low-Ca pyroxenes are not present in these materials. Also, the Na and Cr contents in the Kool grain clinopyroxenes are decidedly enriched compared with the chondrule augites. Measured Na_2O and Cr_2O_3 values in the augites in these chondrules range from 0.0–0.61 wt% (average = 0.42 wt%) to 1.0–2.6 (average = 1.7 wt%), respectively, both of which are several times less than average values in the clinopyroxenes in the SD grains. Thus, textural evidence and compositional differences suggest that Kool grain clinopyroxenes are not related to the type II chondrules in UOCs. Although Kool grains apparently are not present in chondrites, they are found in chondritic interplanetary dust particles. Joswiak et al. (2009) have shown that Kool grains occur in at least four chondritic porous IDPs whose clinopyroxenes have similarly high Na and Cr contents to those in Wild 2, thus SD Kool grains appear to be more akin to IDPs than chondrites.

Three Sulfide Assemblages

We have observed the unusual association of three Fe sulfide minerals in two separate SD tracks. Fragment 2 from track 10 and the TP (fragment 1) from track 141 (Table 2) consist of mixtures of Ni-poor pyrrhotite + pentlandite + Fe-rich sphalerite. Sharp grain boundary contacts between these minerals suggest simultaneous growth of the phases. We were unable to find reports of similar three-sulfide assemblages in chondritic meteorites, but have observed the assemblage in two coarse-grained IDPs and one small cluster IDP (unpublished). In the

coarse-grained IDP U2070A-8Fa, the three sulfides are present with apparently equilibrated olivine (Fo_{94}) and enstatite (En_{95}) grains. Therefore, like Kool grains, this unusual sulfide assemblage may be linked to IDPs, but not chondritic meteorites.

Possible Condensates

Among the earliest formed minerals in the nebula are condensates of Ca, Al, and Ti oxides. These minerals include corundum, hibonite, grossite, perovskite, and spinel (Ebel and Grossman 2000), and are often observed in calcium aluminum rich inclusions in chondrites. To date, two SD tracks have been reported with fragments rich in CAI minerals. These include Inti (track 25), which contains a mixture of numerous fragments composed of spinel, anorthite, diopside, and fassaitic pyroxene (as well as minor abundances of other refractory minerals including melilite, perovskite, and osbornite) and fragment 2 from track 141 (Coki), which is composed of anorthite with spinel inclusions and Al + Ti-rich clinopyroxene (Simon et al. 2008; Matzel et al. 2010). A third track (track 104) may contain two Ca- and Al-rich fragments, which could be CAI-like fragments (Schmitz et al. 2009). As Ca, Al, and Ti oxide phases are highly refractory, they should survive the brief high temperature spikes during impact into aerogel; therefore, if they were present it is unlikely they were preferentially destroyed during capture. Forsterite, enstatite, Fe,Ni metal, and diopside are all known condensates and variously found in the tracks. An important question is whether some of these phases could be direct products of condensation from the nebula.

Perhaps significantly, the bulk of the mass of minerals in the solar nebula (of chondritic composition) will condense at temperatures beginning just below the condensation temperatures of the refractory elements Ca, Al, and Ti (Grossman 2010). At equilibrium, this would include Fe,Ni metal, forsterite, enstatite, and a small amount of diopside. Because of the low oxygen fugacity of the solar nebula, the silicates should be close to their ideal Mg-end member compositions as iron is sequestered into metal during cooling until much lower temperatures are reached. However, small amounts of Fe could enter silicates as the temperature fell to around 900–1000 K if there were an accompanying small increase in oxygen fugacity due to increased dust/gas ratios (Grossman 2010).

Of 40 olivine- and enstatite-only fragments examined in SD, only two had Fe contents below the detection limit of 0.1 wt%, the TP from track 20 (Maya), an En_{100} grain, and fragment 6 from track 77 (Puki), a LIME forsterite fragment. The TP from Maya contains no measurable minor elements except for a small amount of Al and trace Mn. Several other enstatite-only fragments (fragment 12 in track 10; fragment 2 in track 80; fragment 108 in track 77) and enstatite grains (fragment 1 in track 56) embedded in rock fragments in SD have Mg/(Mg + Fe) ratios >0.997 with less than 1.5% total minor oxides (Al_2O_3, CaO, TiO_2, Cr_2O_3, and MnO) and therefore are very close to pure enstatite. These pyroxenes are considered good candidates as condensate minerals that could have formed directly from solar gas composed principally of MgO and SiO vapor as pyroxenes forming in such an environment would not be expected to deviate far from pure enstatite.

Eight olivine fragments with Mg/(Mg + Fe) >0.995 have MnO > FeO, the LIME forsterites. These minerals were first reported in chondritic porous IDPs and UOCs by Klöck et al. (1989) who suggested that they most likely formed in gas to solid reactions in the solar nebula. As Mn condenses at ~1100 K in solid solution in olivine and is not stable in metallic form in a nebular environment and Fe was sequestered by metal, then forsterite with MnO > FeO would result if the olivines failed to incorporate Fe at lower temperatures. If this interpretation is correct, then 8 fragments representing four Wild 2 particles by analogy may also have condensate origins. In all, 27%, or 14 of 52 forsterite and enstatite fragments from SD (including forsterite and enstatite grains in rock fragments) have chemical characteristics, suggesting that they may have formed directly in the nebula by cooling gas. Ultra-refractory inclusions of V-bearing Ti nitrides along with Mo + W-rich platitum group nuggets were observed in spinels and anorthite in track 25, the Stardust CAI-rich track known as Inti (Brownlee et al. 2008; Simon et al. 2008). These inclusions are very likely to have condensate origins as well. Condensation calculations (Ebel 2006) indicate that these materials would form at very high temperatures and reducing conditions and would be expected to pre-date their host phases.

Absence of Phyllosilicate Minerals

A fundamental question regarding Wild 2 samples is whether phyllosilicates and other aqueously altered minerals are present. Such minerals might include smectites, cronstedtite, tochilinite, magnetite, Fe sulfides, and carbonates, which are commonly found in phyllosilicate-rich matrix in carbonaceous and ordinary chondrites. To date, there are no reports of phyllosilicates in SD tracks even though dozens of tracks have been studied by a host of methods. However, because phyllosilicates are generally only stable at low temperatures, it is feasible that these minerals were present in the Wild 2 projectiles, but were modified during capture heating in silica aerogel. Some tantalizing evidence of possible aqueous alteration products in Wild 2 has recently been demonstrated by Berger et al. (2011)

who have shown that several SD Fe sulfides are consistent with low temperature formation based on their mutual associations and diffraction patterns, which match low temperature polytypes. In addition, magnetite has been reported in one SD track (track 80) (Bridges et al. 2010; Stodolna et al. 2010), also confirmed in our lab on the same track, and two small (< 300 nm) carbonates were reported by Flynn et al. (2009). In chondrites, both magnetite and carbonates are secondary minerals associated with aqueously altered matrix. In the SD tracks which contain these minerals, however, no phyllosilicates are observed; thus, it is unclear whether these phases (Fe sulfides, magnetite, carbonates) formed in aqueous alteration environments or whether alternative explanations can account for their formation. Magnetite, for instance, can form at high temperatures in oxidizing conditions, while Fe sulfides may grow from vapor in low temperature, low pressure environments (Bradley 2003). Similarly, carbonates have been observed in anhydrous CP IDPs (Joswiak and Brownlee 2001), suggesting growth without hydration processes. Thus, the presence of low temperature minerals is evidence for the presence of phyllosilicates in Wild 2, but does not prove their existence.

Although we have studied > 87 coarse fragments from 16 tracks and numerous large patches of MSG in bulbous tracks using a range of TEM techniques, we have not observed any minerals uniquely indicative of aqueous alteration processes nor their dehydrated equivalents. Could phyllosilicates have originally been present but destroyed during capture, perhaps converted to MSG? Indeed, impact temperatures exceeding 1800 °C were likely during this process (Roskosz et al. 2008), temperatures well above the stability points of phyllosilicates. However, the highest temperature pulses were short in duration and destruction of all phyllosilicates would not be expected if they were present in large amounts (patches several microns or so in size). Several studies of shots of phyllosilicates using light-gas guns and launch velocities equal to or greater than 6.1 kms^{-1} have shown conclusively that some low temperature phyllosilicates will survive (Okudaira et al. 2004, 2006; Zolensky et al. 2008), particularly in grains > 1 μm in size (Noguchi et al. 2007). Thus, we would expect that bulbous tracks excavated by impactors which were composed of phyllosilicate-rich materials and that were several to tens of microns in size should have some preserved phyllosilicates and this is not observed. The proportions of MSG in some of the tracks is high and may have approached 50 vol% (Westphal et al. 2009; Stodolna et al. 2010), or higher; therefore, it is possible that significant amounts of phyllosilicates were present in the progenitor particles of bulbous tracks, but there is no direct evidence of these putative phyllosilicates.

WILD 2 IMPACTOR ANALOGS AND CHARACTERISTICS

Type A Impactors

The morphological characteristics of the type A tracks examined in this study show that the Wild 2 particles must have been composed of high strength largely nonfragmenting materials. Electron microscopy and other observations show that the type A impactors were composed of single mineral grains, possible chondrule fragments and other multi-mineralic assemblages (rocks). One characteristic common to all the type A tracks is that MSG is absent or only present at minor levels. If MSG is produced by capture heating of fine-grained materials, then this would imply that the impactors largely escaped Wild 2 without significant adhering fine-grained matrix material. A simple scenario that might account for "clean" particles escaping Wild 2 is that they were encased in ice, which sublimated away during transport between the comet and the spacecraft collector.

Microchondrules

Fragments from five type A tracks (tracks 22, 26, 27, 56, and 130) are mineralogically similar to known chondrules or chondrule fragments from chondritic meteorites. Apparent sizes for these fragments range from ~3 to ~17 μm. If these fragments are indeed related to chondrules, then an important concern is the apparent size differences between the SD fragments and "normal" chondrules, which range in size from ~150 μm up to millimeters in most meteorite groups (CH chondrites are the exception where chondrules with diameters as low as 4 μm [Scott 1988] are found).

A number of authors have shown that populations of very small chondrules exist in some meteorites. These tiny chondrules, known as microchondrules, are typically less than 40 μm in diameter and many are as small as a few microns or smaller. In a mm-sized clast from the Piancaldoli (LL3.4) ordinary chondrite, for instance, numerous radial pyroxene ($Fs_{1.3–8.7}$) microchondrules, 3–64 μm in diameter, were found associated with fine-grained silicate matrix, Fe,Ni metal, and troilite grains, and were believed to have formed by similar processes that formed larger droplet-sized chondrules (Rubin et al. 1982). Approximately 30 barred olivine microchondrules, 3–31 μm in diameter, were found in a clast embedded in matrix in the Krymka (LL3.1) ordinary chondrite (Rubin 1989). Likewise, Krot et al. (1997) reported numerous microchondrules in clasts in several type 3 OCs including Semarkona (LL3.0), Bishunpur (LL3.1), EET90161 (3.4), EET90261 (L3.4), and Piancaldoli (LL3.4). In this study, the microchondrules typically occur with fine-grained matrix in the rims of low-FeO

porphyritic olivine chondrules leading the authors to suggest that the microchondrules probably formed from melting of the surfaces of their host chondrules rather than flash heating in the nebula typical of larger chondrules postulated by most researchers.

These studies indicate that the small sizes of the putative SD chondrule fragments are not problematic to linking the fragments with known chondrule populations. The abundances of microchondrules in chondrites is low, however, compared with "normal" chondrules (Wasson 1993). Whether this means that they were not formed in the nebula during "normal" chondrule forming events, were subsequently destroyed because of their small sizes, or were removed prior to agglomeration, is not clear. The latter cause would strengthen arguments that small grains were transported from the chondrule-forming regions of the inner nebula to the Kuiper belt via models such as the X-wind proposed by Shu et al. (1997).

Large Grain IDPs

Two type A tracks (tracks 20 and 59) were produced by single mineral grain impactors. The TP from track 20 is composed of a single low-Ca pyroxene of composition En_{100}. No other fragments are present in the track. Track 59, although composed of a more complex assemblage of Fe-Ni sulfides and pure SiO_2 glass, was probably produced by an impactor made from a single pentlandite grain, which was modified to Ni-poor and Ni-rich sulfides during capture heating. No MSG was observed in either track. From studies of anhydrous IDPs collected in the stratosphere, we know that a small portion are composed of single mineral grains (Rietmeijer 1998; unpublished data). Examples of two such stratospheric IDPs, a single enstatite grain and a Fe-Ni sulfide crystal, are shown in Fig. 41. Like the impactors that produced tracks 20 and 59, these IDPs are largely composed of single mineral grains and are in the size range calculated for type A impactors (Table 1). These characteristics suggest that single mineral IDPs are plausible analogs to impactors that produced some type A tracks.

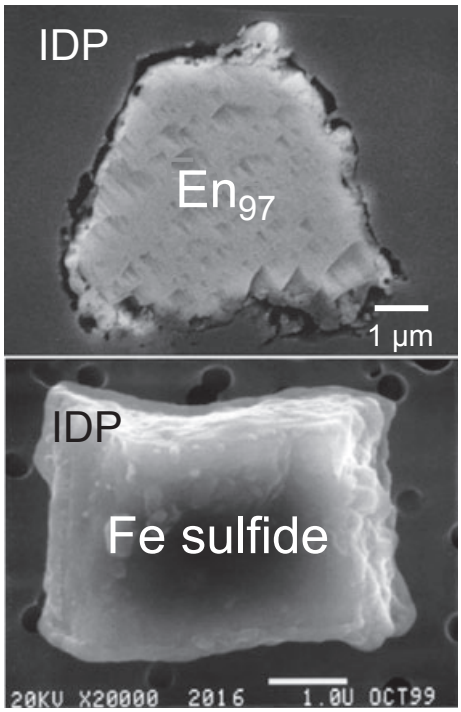

Fig. 41. Large mineral stratospheric IDPs comparable to impactor particles that produced some type A tracks. Little to no fine-grained (submicron) material is attached to these IDPs analogous to the observation that no MSG is present in the two SD tracks (tracks 20 and 59) that were produced by single mineral grain particles.

Type B Impactors

The five type B tracks that we studied (tracks 10, 41, 57, 77, and 141; Fig. 1b) contain numerous large discrete mineral and rock fragments located throughout their bulb regions and roots. Large amounts of MSG in these tracks may indicate the presence of fine-grained matrix in the original impacting particles. A striking feature of these tracks is the large variation in mineral types present (Table 2). In track 41, for instance, a mixture of individual isolated olivine fragments with widely varying compositions including $Fo_{79–85}$, $Fo_{92,}$ and LIME forsterite as well as enstatite, cristobalite, a bulk Mg-Al silicate glass (possibly primary), Kool grains, and other rock fragments were present, indicating that the original impacting particle was composed of a large assortment of unequilibrated coarse minerals and rocks and possibly fine-grained materials. Olivine and pyroxene fragments typically dominate the coarse-grained mineral fraction in the type B tracks. In general, the impactors that produced type B tracks were composed of mixtures of unequilibrated, weakly bonded coarse- and probable fine-grained (submicron) materials. Based on these characteristics, cluster IDPs and chondrite matrix(+clasts) have properties consistent with type B impactors.

Cluster IDPs as Analogs to Type B Impactors

Cluster IDPs collected in the stratosphere are composed of mixtures of chondritic fine-grained materials and diverse coarse crystalline monomineralic grains and mineral assemblages (Thomas et al. 1995; Flynn et al. 2009). Found as disaggregated clumps on collector flags, these IDPs are composed of uncompacted weakly bonded aggregates and are the weakest ET materials known. Cluster IDPs have similar properties to

those expected from the impactors that produced the type B tracks (Flynn et al. 2009) and in some cases type C tracks.

In a detailed study, Thomas et al. (1995) describe a cluster IDP, which was composed of > 50 fragments larger than 5 μm with hundreds of smaller pieces all of which were chemically and mineralogically heterogeneous. This particle would have had a size of 63 μm across if reconstructed to a density 0.5 $g.cm^{-3}$ sphere. In the coarse fraction, individual fragments were dominated by olivine- or low-Ca pyroxene-rich grains (both equilibrated and unequilibrated). LIME silicates and Fe-Ni sulfides and occasional high-Ca pyroxene, glass, and kamacite were also present. Using XRD, Flynn et al. (2009) also showed that cluster IDPs are dominated by olivine, pyroxene, and Fe-Ni sulfides, although they were unable to determine whether these phases were from the coarse- or fine-grained components or mixtures of the two. In SD, olivines (including LIME forsterites), low-Ca pyroxenes, and Fe-Ni sulfides constitute the major minerals in the type B tracks and like giant cluster interplanetary dust particles contain only minor abundances of high-Ca pyroxene, glass, and Fe,Ni metal.

Equally important as the large mineral grains in cluster IDPs is the fine-grained fraction. In the Thomas et al. (1995) study, olivine and low-Ca pyroxene dominate the fines and Fe-Ni sulfides and GEMS are abundant. Thus, a hypothetical cluster IDP containing large proportions of fine-grained (submicron) Fe,Mg silicates and sulfides as well as coarse-grained Fe,Mg silicates and sulfides and minor Fe,Ni metal would have the necessary ingredients to produce both the observed coarse fragments and MSG, which is ubiquitously distributed in type B and C tracks. Furthermore, cluster IDP sizes are similar to the expected sizes of many type B impactors.

Ishii et al. (2008) suggested that because SD tracks lack or contain low abundances of certain distinct components that are found in CP IDPs including vapor-phase enstatite whiskers and platelets, GEMS, carbon-rich materials, and presolar grains, Wild 2 is largely composed of components from the inner solar system that are typically only found in chondrites. We advocate that we cannot be certain that these distinct IDP components were not present in the Wild 2 impacting particles because of their low probability of survival during collection. All are submicron in size or have at least one direction with submicron dimensions and were likely present in fragile porous aggregates, which would further decrease their likelihood of survival. Destruction during capture would be particularly true with GEMS, which have low melting points due to high glass abundances. It would be unlikely to observe whiskers in microtome sections as they would have to be fortuitously oriented with their C-axes parallel to the plane of the section, an unlikely scenario. Recent work on large mineral and rock grains from a giant cluster IDP, believed to have a cometary origin, has shown mineralogical similarities to many large fragments from Wild 2 (Brownlee et al. 2011). This demonstrates that porous aggregate IDPs and particles derived from Wild 2 do have many materials in common, suggesting that CP IDPs and cluster IDPs could be analogous to materials that accreted to the comet.

Chondrite Matrix as an Analog to Type B Impactors

Although cluster IDPs have many of the properties consistent with impactors that produced type B tracks, chondrite matrix materials must also be considered plausible candidates. Consisting of complex mixtures of very fine-grained materials, unequilibrated mineral and rock clasts and chondrule fragments, chondrite matrix comprises significant proportions in most chondrite groups. In UOCs, interchondrule clastic matrix is often porous and hosts a large number of mineral species including silicates, oxides, sulfides, Fe,Ni metal, and many low temperature minerals (Brearley 1996; Scott and Krot 2005). Olivines and low-Ca pyroxenes are commonly observed in matrix in many type 3 chondrites including many low subtypes such as Acfer 094 (C3.0), ALHA77307 (CO3.0), Adelaide, Semarkona (LL3.0), Kakangari, Bishunpur (LL3.1), and Krymka (LL3.1). The olivines and pyroxenes can be as large as several microns or more (Scott and Krot 2005). In Krymka matrix, for example, mineral clasts consist of olivine (Fo_{60} to Fo_{94}) grains typically greater than 5 μm and up to 20 μm in length, as well as large low-Ca pyroxenes ($En_{73–95}$), Ca-rich pyroxenes, sulfides, and Al-rich silicate glass (Weisberg et al. 1997). Lithic clasts consisting of olivine + pyroxene assemblages are also found in the matrix. In general, the minerals and their relative proportions and sizes are comparable to the mineral fragments observed in type B SD tracks where olivines and low-Ca pyroxenes comprise more than half of the observed fragments (Table 2). In a study of Stardust olivines and low-Ca pyroxenes, Zolensky et al. (2008) show that Wild 2 olivine Fe/Mg ratios span a large range (Fo_4 to Fo_{100}) comparable to matrix olivines from chondrites including Murchison (CM2) and Orgueil (CI1). Low-Ca SD pyroxenes also span a large Fe/Mg ratio (En_{52} to En_{100}), a range larger than most individual chondrites, but comparable to enstatites from chondrite matrix (Zolensky et al. 2008). Thus, a hypothetical impactor composed of a portion of say, Krymka-like matrix (fine-grained materials and coarser clasts) in the size range of several tens of microns, could produce the observed morphologies of bulbous tracks and provide many of the large fragments and fine-grained components (MSG) present in these tracks.

The argument that unequilibrated chondrite matrix is analogous to Wild 2 impactors that produced type B (and C) tracks is further strengthened by comparing the minor element compositions of olivines and low-Ca pyroxenes in the SD tracks to matrix mineral clasts from chondrites of low subtypes which have suffered the least amount of parent body metamorphism. Restricted FeO contents and minor element abundances in olivines are observed in type 4–6 chondrites (dotted ovals in Fig. 34) compared with less equilibrated ones (references provided in Fig. 34 caption). The dispersion of Fe/Mg ratios in olivine in chondrites decreases with increasing metamorphic grade. The abundances of the minor elements also decrease as these elements are driven out of their crystal structures during equilibration. In SD, the Fe/Mg ratios and abundances of Ca, Cr, and Mn from olivine fragments from the type B tracks (and type C) are highly variable (Fig. 34). Fayalite contents in track 41 olivine fragments, for instance, range from 0.24 to 31 mol% and their CaO (0.04–0.26 wt%), Cr_2O_3 (0.06–0.44 wt%), and MnO (0.27–0.73 wt%) concentrations are similarly wide-ranging. Track 77 olivines have similar variations with CaO, Cr_2O_3, and MnO contents ranging from 0.04–0.40, 0.04–0.30, and 0.37 – 0.86 wt%, respectively. Both the Fe/Mg ratios and Ca, Cr, and Mn concentrations in olivines from the matrices of UOCs show wide variations which are similar to the SD olivines (Fig. 34). In particular, olivines in type IIA chondrules show considerable variation in their Mn/Fe ratios in unequilibrated ordinary, CO, and CR chondrites (Berlin et al. 2011). Similarly, wide-ranging Cr values in Wild 2 olivines mimic large variations in Cr contents in olivines in type 3.0-3.2 ordinary and carbonaceous chondrites (Grossman and Brearley 2005). Thus, the large variation of Cr in Wild 2 olvines implies a very primitive material. Olivines in the SD fragments as well as those in matrices from chondrites of low subtypes have similar chemical properties with respect to the most important major and minor elements, indicating their largely unequilibrated nature.

Like the olivines, low-Ca pyroxenes in SD also have wide variations in Al, Cr, and Mn (Fig. 37). Low-Ca pyroxenes from matrices from low subtype chondrites, such as Semarkona, correspondingly have wide ranges, reflecting a similar chemical disequilibrium.

Chondrite matrix shows systematic deviations from chondritic composition. In most chondrite groups, many of the major elements in bulk matrix are either enriched or depleted when normalized to CI. For instance, Na is depleted in carbonaceous chondrite matrix, but enriched in matrix in the ordinary chondrites Semarkona and Bishunpur, while Fe can show either depletions or enrichments depending upon which group is examined (Hutchison 2004). An important question is, how do the bulk compositions of the SD impactors that produced the bulbous tracks compare with chondrite matrix? Unfortunately, we do not have bulk analyses of the entire tracks in this study and therefore cannot make direct comparisons. However, bulk compositions from some crater residues in SD foils have been measured. The analyses of bulk residues in craters > 50 μm in diameter showed that some elements (Na and K) are enriched, while others (S, Cr, and Fe) have moderate-to-large depletions when normalized to Si and CI composition (Flynn et al. 2006). The average bulk contents of the elements Mg and Ca were essentially chondritic. Similar results were obtained from crater residues in a TOF-SIMS study by Leitner et al. (2008) although Ca was slightly enriched above CI. In both studies, large compositional ranges in the crater residue compositions showed variations by factors of 200× or more for some elements. Thus, it appears that large bulk chemical heterogeneities are present in different SD impactors. It is not clear whether these results are applicable to the SD tracks in this study, but they do show that some SD impactors that produced type B tracks, like bulk chondrite matrix, are not chondritic in all elements.

Type C Impactors

Type C tracks have similar properties to type B tracks except that their width/length ratios are greater and they lack large central roots beneath their bulbs. This suggests that the fragments in type C tracks exhibit a smaller size variation (are more evenly sorted) than type B tracks. The impactors that produced type C tracks must have been inherently weak, possibly due to having high internal porosities or large proportions of fine-grained matrix allowing them to easily disaggregate into numerous fragments during capture. These characteristics are consistent with both cluster IDPs and chondrite matrix. The Wild 2 impactors that produced type C tracks were probably similar to type B impactors, but did not contain large structurally strong mineral or rock fragments.

Petrologic Type Classification

One method to assess the primitiveness of the original Wild 2 particles that produced the type B/C tracks is to apply the classification scheme originally proposed by Van Schmus and Wood (1967) and later discussed by Huss et al. (2005). In chondrites, Van Schmus and Wood (1967) used ten categories based on textural and mineralogical criteria to measure equilibration. The criteria that are used in the classification method that are applicable to the SD tracks include the Fe/Mg heterogeneity of olivines and low-Ca pyroxenes, abundance of feldspar, Ni content of sulfides,

and atomic structural state of low-Ca pyroxenes. Type 3 chondrites display the least amount of re-equilibration with type 2 and 1 showing progressively more aqueous alteration, respectively, and types 4–6 displaying increasing thermal metamorphism. Here, we argue that reconstructed SD particles most closely equate to unequilibrated chondrites of petrologic type 3 in the Van Schmus and Wood (1967) classification scheme.

Van Schmus and Wood (1967) showed that olivines and low-Ca pyroxenes in the most unequilibrated type 3 chondrites have heterogeneities of > 5% in their Fe and Mg contents from their mean values. How do the SD olivines and low-Ca pyroxenes in the bulbous tracks compare? Calculation of the Mg/(Mg + Fe) ratios in these olivines show deviations ranging from 5% to 18%. In Febo, the only track containing multiple low-Ca pyroxenes, we calculate a mean Mg/(Mg + Fe) ratio of 0.93 and a standard deviation of 7.7%. We showed above that the minor elements (which are also homogenized during equilibration) vary widely in both the SD olivines and pyroxenes. Thus, it appears that the Fe-Mg and minor element heterogeneity of the SD olivines and pyroxenes equate reasonably well to unequilibrated type 3 chondrites.

A second criterion in the classification scheme correlates increasing feldspar abundance with increasing petrologic type from 2 to 6. Only chondrites of petrologic type 2 or 3 contain few to no feldspar minerals. In equilibrated chondrites, the proportions of feldspar increase as this mineral grows at the expense of other phases. In SD, monomineralic feldspar fragments are rare as only two fragments were found from a total of 87 fragments observed. Thus, this criterion is qualitatively consistent with a type 3 classification.

A third measure considers the mean Ni content in Fe sulfides. In unmetamorphosed chondrites, Fe sulfides, principally troilite, contain up to 3 wt% Ni, which drops to less than 0.5 wt% in metamorphosed samples. Pentlandite may contain up to 45 wt% Ni. In Stardust, the Ni contents of Fe sulfides are somewhat variable, but often are larger than 0.5 wt%. For instance, in track 10 (Arinna), the Ni content measured in three large pyrrhotites ranges from 0.0 to 5.4 wt%, while in track 57 (Febo), Ni contents of three of four analyses of the Fe sulfide TP are > 0.9 wt%. Two pyrrhotites in track 77 have Ni contents > 0.6 wt% and three of four analyses of the Fe sulfide which comprises the TP from Coki (track 141) have Ni abundances > 0.5 wt%. Thus, the Ni contents of many Fe sulfide fragments from SD are high, similar to Fe sulfides in unmetamorphosed chondrites.

Van Schmus and Wood (1967) showed that chondrules and chondrule fragments are absent in type 1, sparse in type 2, easily delineated in unequilibrated type 3 chondrites, and become less well-defined in high petrologic types due to solid state recrystallization from increasing thermal metamorphism. In SD, 11% of all the large fragments studied may be chondrule fragments (Table 11), as they have similar mineralogical and textural properties to known chondrule types. If these SD fragments are actual chondrule fragments, then the progenitor particles from which they were derived did not experience significantly high thermal metamorphism or extensive aqueous alteration, a scenario that is consistent with unequilibrated chondrite types.

Low-Ca pyroxenes in unequilibrated chondrites tend to have predominantly monoclinic atomic structures with the monoclinic/orthorhombic ratio decreasing with increasing equilibration (Van Schmus and Wood 1967). Although the crystalline structures of most SD low-Ca pyroxenes are not known, some of the low-Ca pyroxenes that we observed are monoclinic. Orthorhombic as well as mixed monoclinic/orthorhombic types also occur. Finally, the high abundance of MSG in the bulbous tracks, believed to indicate the presence of significant fine-grained materials in the original Wild 2 particles, equates to chondrites that contained abundant matrix. As matrix decreases in abundance and individual minerals increase in size during increasing equilibration, the high abundances of probable fine-grained materials in the Wild 2 particles would be consistent with little to no metamorphism.

Application of the Van Schmus and Wood (1967) classification scheme to the SD fragments and track properties broadly indicates that the SD progenitor particles equate to chondrites of around petrologic type 3 and therefore are likely very primitive. Taken together, these properties suggest that the metamorphosed chondrites, which constitute the largest sampling of chondrites found on Earth, are severely underrepresented in Stardust compared with their unequilibrated counterparts. This may be evidence that the progenitors were not present in large parent bodies prior to accretion in comet Wild 2.

Summary of Impactor Characteristics and Possible Origins of Progenitor Particles

The abundances and distribution of the coarse fragments and fine-grained materials (MSG) in the tracks, the chemical compositions of the large mineral and rock fragments, and the physical properties of the different track types are some of the characteristics that were used to reconstruct hypothetical impactor particles that were derived from Wild 2. Figure 42 illustrates envisioned impactors and analogous ET materials that have the physical and mineralogical properties that could have produced each track type. Clearly, type A

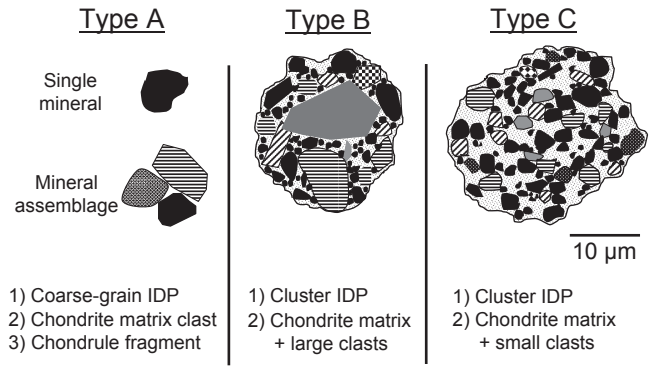

Fig. 42. Characteristics of hypothetical impactors that produced type A, B, and C tracks. Type A tracks were produced by single mineral or competent assemblages of a few minerals without adhering fine-grained (submicron) materials. Analogous extraterrestrial materials include coarse-grained IDPs, matrix clasts, or chondrule fragments from chondrites. Calculated impactor diameters range from 7 to 14 μm. Type B tracks were produced by large impactors composed of mixtures of unequilibrated coarse- and fine-grained materials. The coarse materials include both single mineral grains and rock fragments. The wide dispersion of the coarse fragments in these tracks indicates that the impactors were structurally weak and/or highly porous allowing easy disaggregation of the constituent fragments during impact into aerogel. These characteristics are consistent with cluster IDPs or chondrite matrix (+clasts). Type C tracks were produced by impactors very similar to type B except that the proportions of fine to coarse materials was higher and the embedded coarse fragments were smaller or weaker than in type B tracks. Cluster IDPs or chondrite matrix(+small clasts) are likely analog ET materials. Scale bar applies to all three drawings.

impactors were texturally dissimilar to those that produced type B/C tracks. In this scenario, type A impactors that we worked on were generally smaller and composed of simpler mineralogy, typically being composed of either single mineral grains or small competent mineral assemblages or rock fragments with little to no fine-grained materials. The lack of appreciable amounts of fine-grain material adhering to the impactor particles suggests that their progenitors accreted to comet Wild 2 as "clean" grains. Expulsion of grains from the comet from heating during approach to the Sun was likely a gentle process and would not be expected to physically separate coarse minerals from adhering fines (Brownlee et al. 2006). For "clean" grains to be accreted to the comet, two general histories can be envisioned: (1) they may have been collisionally produced fragments or (2) they may have been early generation nebular solids. We did not observe shock effects in most fragments from the type A tracks, although most debris liberated in collisions is generally not shocked. In the second scenario, progenitor particles were nebular products that were transported directly to the outer nebula, possibly encased in ices. In this scenario, type A impactors represent chondrule fragments or coarse-grained clasts (or large mineral IDPs) that were not previously incorporated into larger bodies. The chondrule fragments may have been produced by direct collisions between smaller chondrules in a turbulent nebula. Some of the SD fragments (type A) could be broken microchondrules.

Impactors that produced track types B and C were probably very similar in their physical characteristics with the major differences being in the proportions of fine- to coarse-grained components and an upper size limit of the coarse-grained fraction in the particles that produced the type C tracks (coarse fragments were smaller in the C type impactors). Type B/C impactors had the following characteristics (Fig. 42): They (1) were mixtures of coarse fragments and fine-grained materials, (2) were composed of unequilibrated mineral assemblages and rock clasts, and (3) were aggregates of loosely bonded grains possibly with high porosities. These characteristics point to either cluster IDPs or chondrite matrix (clasts + fine-grained materials) as the best known extraterrestrial analogs. Like the type A impactors, an important question concerns whether the progenitor particles were derived from parent bodies or directly from the nebula prior to incorporation into comet Wild 2. Although we cannot adequately address this question due to insufficient evidence, we favor a direct nebular source region in part because of the lack of phyllosilicate minerals in the SD tracks and the unequilibrated nature of the bulbous track impactors indicating that these materials were not subjected to thermal metamorphism and therefore did not reside in parent bodies. Shock effects are absent in most fragments from type B/C tracks as well, which might be expected in materials forcibly removed from large bodies.

Fragments from type B/C tracks are aggregates of fine and coarse materials that were ejected from the comet. Many of the Wild 2 particles that produced type A tracks are competent impactors many of which are mineralogically similar to chondrule fragments and therefore may have been produced in the chondrule-forming region(s) of the nebula. If these Wild 2 particles are chondrule fragments (or microchondrules), then they must have been transported to the outer nebula perhaps by radial transport mechanisms such as turbulent convection (Ciesla 2007) or X-winds (Shu et al. 1997). Such transport may have resulted in collisions, perhaps with other chondrules, resulting in fragmentation prior to incorporation into Wild 2.

CONCLUSIONS

We studied in detail the compositions and textures of 87 large mineral and rock fragments from 16 Stardust

tracks and their possible relationships to one another. Included were 55 single mineral and 32 rock fragments from 10 carrot-shaped type A tracks, 5 bulbous type B tracks, and a single bulbous type C track. Olivine and low-Ca pyroxene comprised the largest proportions of single mineral fragments representing 53% and 23% (by number), respectively. Eight percent (by number) of the single mineral fragments were composed of Fe-Ni sulfides. A small number of other single phase fragments were also found including Fe,Ni metal, feldspar, high-Ca pyroxene, and a single occurrence of cristobalite. Two fragments composed of bulk silicate glass are believed to be primary materials derived directly from comet Wild 2. All of the monomineralic olivine fragments and nearly all of the low-Ca pyroxene fragments were found in the type B and C tracks. Comparison of the components between all 16 tracks indicates that each track was mineralogically unique. The simplest tracks were composed of clean roots with only single mineral terminal particles, while some mineralogically complex tracks consisted of > 50 coarse fragments with significant MSG dispersed throughout their track volumes.

Impactors that produced type A tracks were composed of single mineral grains or competent mixtures of a small number of minerals or rock fragments, generally without fine-grained matrix. Track lengths of the 10 type A tracks show that the impactors ranged in size from 7 – 14 μm. These characteristics suggest that impactors that produced type A tracks are analogous to large mineral IDPs or mineral/lithic clasts in unequilibrated chondrites, which may have accreted to comet Wild 2 without previous incorporation into parent bodies.

The properties of impactors that produced type B and C tracks are: (1) They were composed of mixtures of coarse ($\sim >1$ μm)- and fine-grained (submicron) materials; (2) were loosely bonded and possibly highly porous, therefore structurally weak; and (3) composed of unequilibrated minerals. Large fragments in type C tracks were probably smaller or structurally weaker than type B counterparts. The large range of Fe/Mg ratios and of minor element abundances in the coarse olivines and pyroxenes in these tracks is similar to large mineral clasts in chondrite matrix of UOCs and large mineral grains in cluster IDPs, indicating that type B and C impactors are directly analogous to these materials.

Thirty-two rock fragments were found in all three track types. On the basis of mineral assemblages, mineral compositions, and textures, 10 fragments from 7 tracks may be linked with chondrule fragments from well-known chondrule types including ferromagnesian, silica-rich, and Al-rich chondrules. A single refractory inclusion consisting of anorthite with small spinel inclusions and partially rimmed by a refractory high-Ca pyroxene was found in a type B track. Eight Kool grain (kosmochloric high-Ca pyroxene + FeO-rich olivine ± albite or glass ± spinel) fragments from 5 tracks and 2 pyrrhotite + pentlandite + Fe-rich sphalerite fragments were present in two separate tracks and are unique materials that are not observed in chondrites, but are found in CP IDPs.

Up to 40% of the monomineralic olivine and pyroxene fragments could be primary nebular condensates. These include Fe-free and low-Fe pyroxenes and olivines and LIME forsterites. Except for a single fragment of anorthite with a partial rim of fassaitic pyroxene found in track 141, and a small three-pyroxene fragment containing aluminous diopside (track 80, fragment 1), refractory Ca-, Al-, and Ti-rich minerals were generally not observed in the tracks.

No phyllosilicates were found in any of the tracks studied. The possibility that MSG in the bulbous tracks could be thermally altered material that was derived from primary phyllosilicates and associated phases is unlikely as small amounts of original material would be expected to survive in some of the large patches (up to 10 μm or more) and this has not been observed. It is possible, however, that small amounts of phyllosilicates were present in the Wild 2 particles, but did not survive the high temperatures of capture in aerogel.

Although significant modification occurred to the exteriors of impacting Wild 2 particles the interiors of solid micron grains were very well preserved. Detailed observations of many large fragments along with other track characteristics indicate that most major components in chondritic meteorites are present in Wild 2 including chondrules (fragments), refractory inclusions, fine-grained matrix (modified to MSG), large mineral/rock clasts, and moderately refractory condensate minerals. The unusual materials, Kool grains and the 3-sulfide assemblages, imply direct links to chondritic IDPs as these assemblages are not found in chondrites.

It appears that comet Wild 2's rocky components are meteoritic-like materials that are also seen in primitive chondrites and IDPs. These components appear to have formed in the inner solar system and were transported to the edge of the solar nebula to form comets. An intriguing possibility is that the transportation process sampled material from most and perhaps all of the solar nebula. If this is the case, Wild 2, although it is composed of meteoritic materials, will never actually match the mix of materials found in specific chondrite groups, whose properties are dominated by materials that were predominantly formed in a localized region.

Acknowledgments—The manuscript was greatly improved by reviews from Julien Stodolna and an anonymous

reviewer, and we thank both for their thoughtful comments. We kindly express our gratitude to Hope Ishii and John Bradley for organization of the 3rd Timber Cove Stardust Conference and their efforts to produce this special edition. Special thanks to Scott Braswell from the Center for Nanotechnology, University of Washington, for FESEM assistance. This work was supported by the National Aeronautics and Space Administration (NASA) grants NNG06GG00GS05 and NNX10AI89GS01.

Editorial Handling—Dr. John Bradley

REFERENCES

Abraham K., Gebert W., Medenbach O., Schreyer W., and Hentschel G. 1983. Eifelite, $KNa_3Mg_4Si_{12}O_{30}$, a new mineral of the osumulite group with octahedral sodium. *Contributions to Mineralogy and Petrology* 82:252–258.

A'Hearn M. H. 2011. Comets as building blocks. *Annual Review of Astronomy and Astrophysics* 49:281–299.

Alexander C. M. O'D., Barber D. J., and Hutchison R. 1989a. The microstructure of Semarkona and Bishunpur. *Geochimica et Cosmochimica Acta* 53:3045–3057.

Alexander C. M. O'D., Hutchison R., and Barber D. J. 1989b. Origin of chondrule rims and interchondrule matrices in unequilibrated ordinary chondrites. *Earth and Planetary Science Letters* 95:187–207.

Bayliss P., Berry L. G., Mrose M. E., and Smith D. D., eds. 1980. *JCPDS mineral powder diffraction file data book*. Swarthmore, PA: JCPDS International Centre for Diffraction Data.

Berger E. L., Keller L. P., Joswiak D., Matrajt G., and Lauretta D. S. 2008. Low-temperature sulfides in Stardust TEM analysis of a sphalerite/pyrrhotite assemblage from track 7 (abstract #5298). 71st Annual Meeting of the Meteoritical Society. *Meteoritics & Planetary Science* 43.

Berger E. L., Zega T. J., Keller L. P., and Lauretta D. S. 2011. Evidence for aqueous activity on comet 81P/Wild 2 from sulfide mineral assemblages in Stardust samples and CI chondrites. *Geochimica et Cosmochimica Acta* 75:3501–3513.

Berlin J., Jones R. H., and Brearley A. J. 2011. Fe-Mn systematics of type IIA chondrules in unequilibrated CO, CR and ordinary chondrites. *Meteoritics & Planetary Science* 46:513–533.

Bradley J. 2003. The astromineralogy of interplanetary dust particles. In *Astromineralogy lecture notes in physics*, edited by Henning T. K. Berlin, Germany: Springer-Verlag. pp. 217–235.

Brearley A. J. 1996. Nature of matrix in unequilibrated chondrites and its possible relationship to chondrules. In *Chondrules and the protoplanetary disk*, edited by Hewins R. H., Jones R. H. and Scott E. R. D. New York: Cambridge University Press. pp. 137–151.

Brearley A. J. and Jones R. H. 1998. Chondritic meteorites. In *Planetary materials*, edited by Papike J. J., Reviews in Mineralogy, vol. 36. Washington, D.C.: Mineralogical Society of America. pp. 3-1 to 3-398.

Bridges J. C. and Changela H. G. 2010. Chondrule fragments in Stardust tracks 113 and 154 (abstract #5280). 73rd Annual Meeting of the Meteoritical Society. *Meteoritics & Planetary Science* 45.

Bridges J. C., Burchell M. J., Changela H. C., Foster F. J., Creighton J. A., Carpenter J. D., Gurman S. J., Franchi I. A., and Busemann H. 2010. Iron oxides in comet 81P/Wild 2. *Meteoritics & Planetary Science* 45:55–72.

Brigham C. A., Yabuki H., Ouyang Z., Murrell M. T., El Goresy A., and Burnett D. S. 1986. Silica-bearing chondrules and clasts in ordinary chondrites. *Geochimica et Cosmochimica Acta* 50:1655–1666.

Brownlee D. E. 2004. Comets. In *Meteorites, comets and planets*, edited by Davis A. M. Treatise on Geochemistry, vol. 1. Oxford: Elsevier-Pergamon, pp. 663–688.

Brownlee D., Tsou P., Aléon J., Alexander C. M. O'D., Araki T., Bajt S., Baratta G. A., Bastien R., Bland P., Bleuet P., Borg J., Bradley J. P., Brearley A., Brenker F., Brennan S., Bridges J. C., Browning N. D., Brucato J. R., Bullock E., Burchell M. J., Busemann H., Butterworth A., Chaussidon M., Cheuvront A., Chi M., Cintala M. J., Clark B. C., Clemett S. J., Cody G., Colangeli L., Cooper G., Cordier P., Daghlian C., Dai Z., D'Hendecourt L., Djouadi Z., Dominguez G., Duxbury T., Dworkin J. P., Ebel D. S., Economou T. E., Fakra S., Fairey S. A. J., Fallon S., Ferrini G., Ferroir T., Fleckenstein H., Floss C., Flynn G., Franchi I. A., Fries M., Gainsforth Z., Gallien J.-P., Genge M., Gilles M. K., Gillet P., Gilmour J., Glavin D. P., Gounelle M., Grady M. M., Graham G. A., Grant P. G., Green S. F., Grossemy F., Grossman L., Grossman J. N., Guan Y., Hagiya K., Harvey R., Heck P., Herzog G. F., Hoppe P., Hörz F., Huth J., Hutcheon I. D., Ignatyev K., Ishii H., Ito M., Jacob D., Jacobsen C., Jacobsen S., Jones S., Joswiak D., Jurewicz A., Kearsley A. T., Keller L. P., Khodja H., Kilcoyne A. L. D., Kissel J., Krot A., Langenhorst F., Lanzirotti A., Le L., Leshin L. A., Leitner J., Lemelle L., Leroux H., Liu M.-C., Luening K., Lyon I., MacPherson G., Marcus M. A., Marhas K., Marty B., Matrajt G., McKeegan K., Meibom A., Mennella V., Messenger K., Messenger S., Mikouchi T., Mostefaoui S., Nakamura T., Nakano T., Newville M., Nittler L. R., Ohnishi I., Ohsumi K., Okudaira K., Papanastassiou D. A., Palma R., Palumbo M. E., Pepin R. O., Perkins D., Perronnet M., Pianetta P., Rao W., Rietmeijer F. J. M., Robert F., Rost D., Rotundi A., Ryan R., Sandford S. A., Schwandt C. S., See T. H., Schlutter D., Sheffield-Parker J., Simionovici A., Simon S., Sitnitsky I., Snead C. J., Spencer M. K., Stadermann F. J., Steele A., Stephan T., Stroud R., Susini J., Sutton S. R., Suzuki Y., Taheri M., Taylor S., Teslich N., Tomeoka K., Tomioka N., Toppani A., Trigo-Rodríguez J. M., Troadec D., Tsuchiyama A., Tuzzolino A. J., Tyliszczak T., Uesugi K., Velbel M., Vellenga J., Vicenzi E., Vincze L., Warren J., Weber I., Weisberg M., Westphal A. J., Wirick S., Wooden D., Wopenka B., Wozniakiewicz P., Wright I., Yabuta H., Yano H., Young E. D., Zare R. N., Zega T., Ziegler K., Zimmermann L., Zinner E., and Zolensky M. 2006. Comet 81P/Wild 2 under a microscope. *Science* 314:1711–1716.

Brownlee D. E., Joswiak D., Matrajt G., Bradley J., and Ebel D. S. 2008. Ultra-refractory attogram inclusions in comet dust—First condensates? (abstract #1978). 39th Lunar and Planetary Science Conference. CD-ROM.

Brownlee D. E., Joswiak D., and Matrajt G. 2011. Large coarse-grained solid particles in comets – A uqibuitously distributed component in the solar nebula? (abstract #2235). 42nd Lunar and Planetary Science Conference. CD-ROM.

Bullock E. S., Gounelle M., Lauretta D. S., Grady M. M., and Russell E. 2005. Mineralogy and texture of Fe-Ni sulfides in CI1 chondrites: Clues to the extent of aqueous alteration on the CI1 parent body. *Geochimica et Cosmochimica Acta* 69:2687–2700.

Burchell M. J., Fairey S. A. J., Wozniakiewicz P., Brownlee D. E., Hörz F., Kearsley A. T., See T. H., Tsou P., Westphal A., Green S. F., Trigo-Rodríguez J. M., and Domingúez G. 2008. Characteristics of cometary dust tracks in Stardust aerogel and laboratory calibrations. *Meteoritics & Planetary Science* 43:23–40.

Busemann H., Young A. E., Alexander C. M. O'D., Hoppe P., Mukhopadhyay S., and Nittler L. R. 2006. Interstellar chemistry recorded in organic matter from primitive meteorites. *Science* 312:727–730.

Butterworth A. L., Gainsforth Z., Baufille A., Bonal L., Brownlee D. E., Fakra S. C., Huss G. R., Joswiak D., Kunz M., Marcus M. A., Nagashima K., Ogliore R. C., Tamura N., Telus M., Tylisczak T., and Westphal A. J. 2010. A type IIA chondrule fragment from comet 81P/Wild 2 in Stardust track C2052,2,74 (abstract #1533). 41st Lunar and Planetary Science Conference. CD-ROM.

Chi M., Ishii H. A., Simon S. B., Bradley J. P., Dai Z., Joswiak D., Browning N. D., and Matrajt G. 2009. The origin of refractory minerals in comet 81P/Wild 2. *Geochimica et Cosmochimica Acta* 73:7150–7161.

Ciesla F. 2007. Outward transport of high-temperature materials around the midplane of the solar nebula. *Science* 318:613–615.

Cliff G. and Lorimer G. W. 1975. The quantitative analysis of thin specimens. *Journal of Microscopy* 103:203–207.

Duke J. M. 1976. Distribution of the period four transition elements among olivine, calcic clinopyroxene and mafic silicate liquid: Experimental results. *Journal of Petrology* 17:499–521.

Ebel D. S. 2006. Condensation of rocky material in astrophysical environments. In *Meteorites and the early solar system II*, edited by Lauretta D. S. and McSween H. Y. Jr. Tucson, Arizona: University of Arizona Press. pp. 253–277.

Ebel D. S. and Grossman L. 2000. Condensation in dust-enriched systems. *Geochimica et Cosmochimica Acta* 64:339–366.

Flynn G. J., Bleuet P., Borg J., Bradley J. P., Brenker F. E., Brennan S., Bridges J., Brownlee D. E., Bullock E. S., Burghammer M., Clark B. C., Dai Z. R., Daghlian C. P., Djouadi Z., Fakra S., Ferroir T., Floss C., Franchi I. A., Gainsforth Z., Gallien J.-P., Gillet P., Grant P. G., Graham G. A., Green S. F., Grossemy F., Heck P. R., Herzog G. F., Hoppe P., Hörz F., Huth J., Ignatyev K., Ishii H. A., Janssens K., Joswiak D., Kearsley A. T., Khodja H., Lanzirotti A., Leitner J., Lemelle L., Leroux H., Luening K., MacPherson G. J., Marhas K. K., Marcus M. A., Matrajt G., Nakamura T., Nakamura-Messenger K., Nakano T., Newville M., Papanastassiou D. A., Pianetta P., Rao W., Riekel C., Rietmeijer F. J. M., Rost D., Schwandt C. S., See T. H., Sheffield-Parker J., Simionovici A., Sitnitsky I., Snead C. J., Stadermann F. J., Stephan T., Stroud R. M., Susini J., Suzuki Y., Sutton S. R., Taylor S., Teslich N., Troadec D., Tsou P., Tsuchiyama A., Uesugi K., Vekemans B., Vicenzi E. P., Vincze L., Westphal A. J., Wozniakiewicz P., Zinner E., and Zolensky M. E. 2006. Elemental compositions of comet 81P/Wild 2 samples collected by Stardust. *Science* 314:1731–1735.

Flynn G. J., Lanzirotti A., and Sutton S. R. 2009. Elemental and mineralogical compositions of cluster IDPs: A possible analog to the Wild 2 particles collected by Stardust. 40th Lunar and Planetary Science Conference. CD-ROM.

Fuchs L. H. 1966. Roedderite, a new mineral from the Indarch meteorite. *American Mineralogist* 51:949–955.

Gainsforth Z., Butterworth A. L., Bonal L., Brownlee D. E., Huss G. R., Joswiak D., Ogliore R. C., Telus M., Tyliczszak T., and Westphal A. J. 2010. Coordinated TEM/STXM/IMS analysis of a type IIa chondrule fragment from comet 81P/Wild 2 Stardust track C2052,2,74. 73rd Annual Meeting of the Meteoritical Society. *Meteoritics & Planetary Science* 45.

Graetsch H. and Topalovic-Dierdorf I. 1996. ^{29}Si MAS NMR spectrum and superstructure of modulated tridymite L3-T_O (MX-1). *European Journal of Mineralogy* 8:103–113.

Green S. F., McDonald J. A. M., McBride N., Colwell M. T. S. H., Tuzzolino A. J., Economou T. E., Tsou P., Clark B. C., and Brownlee D. E. 2004. The dust mass distribution of comet 81P/Wild 2. *Journal of Geophysical Research* 109(E12S04):1–13.

Green S. F., McBride N., Colwell M. T. S. H., McDonnell J. A. M., Tuzzolino A. J., Economou T. E., Clark B. C., Sekanina Z., Tsou P., and Brownlee D. E. 2007. Stardust Wild 2 dust measurements. In *Workshop on Dust in Planetary Systems (ESA SP-643)*, held Sept. 26-30, 2005, edited by Krueger H. and Graps A. Kauai, Hawaii: no. 1280. 35–44.

Grossman L. 2010. Vapor-condensed phase processes in the early solar system. *Meteoritics & Planetary Science* 45:7–20.

Grossman J. N. and Brearley A. J. 2005. The onset of metamorphism in ordinary and carbonaceous chondrites. *Meteoritics & Planetary Science* 40:87–122.

Hanner M. S. and Zolensky M. E. 2010. The mineralogy of comet dust. In *Astromineralogy, Lecture Notes in Physics*, edited by Henning T., vol. 815. Berlin: Springer. pp. 203–232.

Hörz F., Bastien R., Borg J., Bradley J. P., Bridges J. C., Brownlee D. E., Burchell M. J., Chi M., Cintala M. J., Dai Z. R., Djouadi Z., Dominguez G., Economou T. E., Fairey S. A. J., Floss C., Franchi I. A., Graham G. A., Green S. F., Heck P., Hoppe P., Huth J., Ishii H., Kearsley A. T., Kissel J., Leitner J., Leroux H., Marhas K., Messenger K., Schwandt C. S., See T. H., Snead C., Stadermann I. F. J., Stephan T., Stroud R., Teslich N., Trigo-Rodríguez J. M., Tuzzolino A. J., Troadec D., Tsou P., Warren J., Westphal A., Wozniakiewicz P., Wright I., and Zinner E. 2006. Impact features on Stardust: Implications for comet 81P/Wild 2 Dust. *Science* 314:1716–1719.

Huang S., Lu J., Prinz M., Weisberg M. K., Benoit P. H., and Sears D. W. G. 1996. Chondrules: Their diversity and the role of open-system processes during their formation. *Icarus* 122:316–346.

Huss G. R., Rubin A. E., and Grossman J. N. 2005. Thermal metamorphism in chondrites. In *Meteorites and the early solar system II*, edited by Lauretta D. S., Leshin L. A., and McSween H. Y. Jr. Tucson: The University of Arizona Press. pp. 567–586.

Hutchison R. 2004. *Meteorites: A petrologic, chemical and isotopic synthesis*. Cambridge: Cambridge University Press. 506 p.

Ishii H. A., Bradley J. P., Dai Z. R., Chi M., Kearsley A. T., Burchell M. J., Browning N. D., and Molster F. 2008. Comparison of comet 81P/Wild 2 dust with interplanetary dust from comets. *Science* 319:447–450.

Jacob D., Stodolna J., Leroux H., Langenhorst F., and Houdellier F. 2009. Pyroxenes microstructure in comet 81P/Wild 2 terminal Stardust particles. *Meteoritics & Planetary Science* 44:1475–1488.

Jones R. H. 1990. Petrology and mineralogy of type II, FeO-rich chondrules in Semarkona (LL3.0): Origin by closed-system fractional crystallization, with evidence for supercooling. *Geochimica et Cosmochimica Acta* 54:1785–1802.

Jones R. H. 1994. Petrology of FeO-poor, porphyritic pyroxene chondrules in the Semarkona chondrite. *Geochimica et Cosmochimica Acta* 58:5325–5340.

Jones R. H. 1996. FeO-rich, porphyritic pyroxene chondrules in unequilibrated ordinary chondrites. *Geochimica et Cosmochimica Acta* 60:3115–3138.

Joswiak D. J. and Brownlee D. E. 2001. Carbonate mineralogy in stratospheric IDPs: Compositions, co-exisiting smectite and comparison to CI carbonaceous chondrites (abstract #1998). 32nd Lunar and and Planetary Science Conference. CD-ROM.

Joswiak D. J., Brownlee D. E., and Matrajt G. 2007. Mineralogy of terminal particles and other large mineral fragments obtained from Stardust tracks. 70th Annual Meteoritical Society Meeting, Tucson, Arizona. *Meteoritics & Planetary Science* 42:5256.

Joswiak D. J., Brownlee D. E., Matrajt G., Westphal A. J., and Snead C. J. 2009. Kosmochloric Ca-rich pyroxenes and FeO-rich olivines (Kool grains) and associated phases in Stardust tracks and chondritic porous interplanetary dust particles: Possible precursors to FeO-rich type II chondrules in ordinary chondrites. *Meteoritics & Planetary Science* 44:1561–1588.

Joswiak D. J., Brownlee D. E., Matrajt G., Messenger S. M., and Ito M. 2010. Stardust track 130 terminal particle: Possible Al-rich chondrule fragment or altered amoeboid olivine aggregate (abstract #2119). 41st Lunar and Planetary Science Conference. CD-ROM.

Joy D. C., Romig A. D. Jr., and Goldstein J. I. 1986. *Principles of analytical electron microscopy*. New York: Plenum Press. 448p.

Kearsley A. T., Burchell M. J., Price M. C., Cole M. J., Wozniakiewicz P. J., Ishii H. A., Bradley J. P., Fries M., and Foster N. J. 2012. Experimental impact features in Stardust aerogel: How track morphology reflects particle structure, composition and density. *Meteoritics & Planetary Science* 47. This issue.

Klöck W., Thomas K. L., McKay D. S., and Palme H. 1989. Unusual olivine and pyroxene composition in interplanetary dust and unequilibrated ordinary chondrites. *Nature* 339:126–128.

Krot A. N. and Wasson J. T. 1994. Silica-merrihueite/roedderite-bearing chondrules and clasts in ordinary chondrites: New occurrences and possible origins. *Meteoritics* 29:707–718.

Krot A. N., Rubin A. E., Keil K., and Wasson J. T. 1997. Microchondrules in ordinary chondrites: Implications for chondrule formation. *Geochimica et Cosmochimica Acta* 61:463–473.

Leitner J., Stephan T., Kearsley A. T., Hörz F., Flynn G. J., and Sandford S. A. 2008. TOF-SIMS analysis of crater residues from Wild 2 cometary particles on Stardust aluminum foil. *Meteoritics & Planetary Science* 43:161–185.

Leroux H., Jacob D., Stodolna J., Nakamura-Messenger K., and Zolensky M. E. 2008a. Igneous Ca-rich pyroxene in comet 81P/Wild 2. *American Mineralogist* 93:1933–1936.

Leroux H., Rietmeijer F. J. M., Velbel M. A., Brearley A. J., Jacob D., Langenhorst F., Bridges J. C., Zega T. J., Stroud R. M., Cordier P., Harvey R. P., Lee M., Gounelle M., and Zolensky M. E. 2008b. A TEM study of thermally modified comet 81P/Wild 2 dust particles by interactions with the aerogel matrix during the Stardust capture process. *Meteoritics & Planetary Science* 43:97–120.

MacPherson G. J. and Huss G. R. 2005. Petrogenesis of Al-rich chondrules: Evidence from bulk compositions and phase equilibria. *Geochimica et Cosmochimica Acta* 69:3099–3127.

Matrajt G. and Brownlee D. E. 2006. Acrylic embedding of Stardust particles encased in aerogel. *Meteoritics & Planetary Science* 41:1695–1835.

Matrajt G., Ito M., Wirick S., Messenger S., Brownlee D. E., Joswiak D., Flynn G., Sandford S., Snead C., and Westphal A. 2008. Carbon investigation of two Stardust particles: A TEM, NanoSIMS, and XANES study. *Meteoritics & Planetary Science* 43:315–334.

Matsunami S., Nisihimura H., and Takeshi H. 1990. The chemical compositions and textures of matrices and chondrule rims of unequilibrated ordinary chondrites-II. Their constituents and implications for the formation of matrix olivine. *Proceedings of the NIPR Symposium on Antarctic Meteorites* 3:147–180.

Matzel J. E. P., Ishii H. A., Joswiak D., Hutcheon I. D., Bradley J. P., Brownlee D., Weber P. K., Teslich N., Matrajt G., McKeegan K. D., and MacPherson G. J. 2010. Constraints on the formation age of cometary material from the NASA Stardust mission. *Science* 328:483–486.

McKeegan K. D., Aléon J., Bradley J., Brownlee D., Busemann H., Butterworth A., Chaussidon M., Fallon S., Floss C., Gilmour J., Gounelle M., Graham G., Guan Y., Heck P. R., Hoppe P., Hutcheon I. D., Huth J., Ishii H., Ito M., Jacobsen S. B., Kearsley A., Leshin L. A., Liu M.-C., Lyon I., Marhas K., Marty B., Matrajt G., Meibom A., Messenger S., Mostefaoui S., Mukhopadhyay S., Nakamura-Messenger K., Nittler L., Palma R., Pepin R. O., Papanastassiou D. A., Robert F., Schlutter D., Snead C. J., Stadermann F. J., Stroud R., Tsou P., Westphal A., Young E. D., Ziegler K., Zimmermann L., and Zinner E. 2006. Isotopic compositions of cometary matter returned by Stardust. *Science* 314:1724–1728.

Messenger S., Joswiak D., Ito M., Matrajt G., and Brownlee D. E. 2009. Discovery of presolar SiC from comet Wild-2 (abstract #1790). 40th Lunar and Planetary Science conference. CD-ROM.

Nakamura T., Tsuchiyama A., Akaki T., Uesugi K., Nakano T., Takeuchi A., Suzuki Y., and Noguchi T. 2008a. Bulk mineralogy and three-dimensional structures of individual Stardust particles deduced from synchrotron X-ray diffraction and microtomography analysis. *Meteoritics & Planetary Science* 43:247–259.

Nakamura T., Noguchi T., Tsuchiyama A., Ushikubo T., Kita N. T., Valley J. W., Zolensky M. E., Kakazu Y., Sakamoto K., Mashio E., Uesugi K., and Nakano T. 2008b. Chondrule-like objects in short-period comet 81P/Wild 2. *Science* 321:1664–1667.

Nakamura-Messenger K., Keller L. P., Clemett S. J., Messenger S., and Ito M. 2011. Nanometer-scale anatomy of entire Stardust tracks. *Meteoritics & Planetary Science* 46:1033–1057.

Noguchi T., Nakamura T., Okudaira K., Yano H., Sugita S., and Burchell M. J. 2007. Thermal alteration of hydrated minerals during hypervelocity capture to silica aerogel at

the flyby speed of Stardust. *Meteoritics & Planetary Science* 42:357–372.

Ogliore R. C., Butterworth A. L., Fakra S. C., Gainsforth Z., Marcus M. A., and Westphal A. J. 2010. Comparison of the oxidation state of Fe in comet 81P/Wild 2 and chondritic-porous interplanetary dust particles. *Earth and Planetary Science Letters* 296:278–286.

Okudaira K., Noguchi T., Nakamura T., Sugita S., Sekine Y., and Yano H. 2004. Evaluation of mineralogical alteration of micrometeoroid analog materials captured in aerogel. *Advances in Space Research* 34:2299–2304.

Okudaira K., Yano H., Noguchi T., Nakamura T., Burchell M. J., and Cole M. J. 2006. Are they really intact? – Evaluation of captured micrometeoroid analogs by aerogel at the flyby speed of Stardust (abstract #1832). 37th Lunar and Planetary Science Conference. CD-ROM.

Price M. C., Kearsley A. T., Burchell M. J., Hörz F., Borg J., Bridges J. C., Cole M. J., Floss C., Graham G., Green S. F., Hoppe P., Leroux H., Marhas K. K., Park N., Stroud R., Stadermann F. J., Telisch N., and Wozniakiewicz P. J. 2010. Comet 81P/Wild 2: The size distribution of finer (sub-10 μm) dust collected by the Stardust spacecraft. *Meteoritics & Planetary Science* 45:1409–1428.

Rhamdhani M. A., Hayes P. C., and Jak E. 2008. Subsolidus phase equilibria of the Fe-Ni-O system. *Metallurgical and Materials Transactions* 39B:690–701.

Rietmeijer F. J. M. 1998. Interplanetary dust particles. In *Planetary materials*, edited by Papike J. J. Reviews in Mineralogy, vol. 36. Washington, D.C.: Mineralogical Society of America, pp. 95–397.

Roeder P. L. and Emslie R. F. 1970. Olivine-liquid equilibrium. *Contributions to Mineralogy and Petrology* 29:275–289.

Roskosz M., Leroux H., and Watson H. C. 2008. Thermal history, partial preservation and sampling bias recorded by Stardust cometary grains during their capture. *Earth and Planetary Science Letters* 273:195–202.

Rubin A. E. 1989. An olivine-microchondrule-bearing clast in the Krymka meteorite. *Meteoritics* 24:191–192.

Rubin A. E., Scott E. R. D., and Keil K. 1982. Microchondrule-bearing clast in the Piancaldoli LL3 meteorite: A new kind of type 3 chondrite and its relevance to the history of chondrules. *Geochimica et Cosmochimica Acta* 46:1763–1776.

Schmitz S. and Brenker F. E. 2008. Microstructural indications for protoenstatite precursor of cometary $MgSiO_3$ pyroxene: A further high-temperature component of comet Wild 2. *The Astrophysical Journal* 681:L105–L108.

Schmitz S., Brenker F. E., Schoonjans T., Vekemans B., Silversmit G., Vincze L., Burghammer M., and Riekel C. 2009. In situ identification of a CAI candidate in 81P/Wild 2 cometary dust by confocal high resolution synchrotron X-ray fluorescence. *Geochimica et Cosmochimica Acta* 73: 5483–5492.

Schulze H., Bischoff A., Palme H., Spettel B., Dreibus G., and Otto J. 1994. Mineralogy and chemistry of Rumuruti; the first meteorite fall of the new R chondrite group. *Meteoritics* 29:275–286.

Scott E. R. D. 1988. A new kind of primitive chondrite, Allan Hills 85085. *Earth and Planetary Science Letters* 91:1–18.

Scott E. R. D. and Krot A. N. 2005. Chondrites and their components. In *Meteorites, comets and planets*, edited by Davis A. M. Treatise on Geochemistry, vol. 1, Oxford: Elsevier-Pergamon, pp. 143–200.

Shu F. H., Shang H., Glassgold A. E., and Lee T. 1997. X-rays and fluctuating X-winds from protostars. *Science* 277:1475–1479.

Simon S. B., Joswiak D., Ishii H. A., Bradley J. P., Chi M., Grossman L., Aleon J., Brownlee D. E., Fallon S., Hutcheon I. D., Matrajt G., and McKeegan K. D. 2008. A refractory inclusion returned by Stardust from comet 81P/Wild 2. *Meteoritics & Planetary Science* 43:1861–1877.

Stadermann F. J., Hoppe P., Floss C., Heck P. R., Hörz F., Huth J., Kearsley A. T., Leitner J., Marhas K. K., McKeegan K. D., and Stephan T. 2008. Stardust in Stardust—The C, N, and O isotopic compositions of Wild 2 cometary matter in Al foil impacts. *Meteoritics & Planetary Science* 43:299–313.

Stephan T., Flynn G. J., Sandford S. A., and Zolensky M. E. 2008. TOF-SIMS analysis of cometary particles extracted from Stardust aerogel. *Meteoritics & Planetary Science* 43:285–298.

Stodolna J., Jacob D., and Leroux H. 2009. A TEM study of four particles extracted from the Stardust track 80. *Meteoritics & Planetary Science* 44:1511–1518.

Stodolna J., Jacob D., and Leroux H.. 2010. Mineralogy of Stardust track 80: Evidences for aqueous alteration and igneous process (abstract #1533). 41st Lunar and Planetary Science Conference. CD-ROM.

Stodolna J., Jacob D., and Leroux H. 2011. Comparing Wild 2 fine-grained material to matrix of primitive meteorites (abstract #2025). 42nd Lunar and Planetary Science Conference. CD-ROM.

Thomas K. L., Blanford G. E., Clemett S. J., Flynn G. J., Keller L. P., Klöck W., Maechling C. R., McKay D. S., Messenger S., Nier A. O., Schlutter D. J., Sutton S. R., Warren J. L., and Zare R. N. 1995. An asteroidal breccia: The anatomy of a cluster IDP. *Geochimica et Cosmochimica Acta* 59:2797–2815.

Tomeoka K., Tomioka N., and Ohnishi I. 2007. Silicates and glass in comet Wild 2 samples: An analytical transmission electron microscope study (abstract #1267). 38th Lunar and Planetary Science Conference. CD-ROM.

Tomeoka K., Tomioka N., and Ohnishi I. 2008. Silicate minerals and Si-O glass in comet Wild 2 samples: Transmission electron microscopy. *Meteoritics & Planetary Science* 43:273–284.

Trigo-Rodríguez J. M., Domínguez G., Burchell M. J., Hörz F., and Llorca J. 2008. Bulbous tracks arising from hypervelocity capture in aerogel. *Meteoritics & Planetary Science* 43:75–86.

Tuzzolino A. J., Economou T. E., Clark B. C., Tsou P., Brownlee D. E., Green S. F., McDonnell J. A. M., McBride N., and Colwell M. T. S. H. 2004. Dust measurements in the coma of comet 81P/Wild 2 by the dust flux monitor instrument. *Science* 304:1776–1780.

Van Schmus W. R. and Wood J. A. 1967. A chemical-petrologic classification for the chondritic meteorites. *Geochimica et Cosmochimica Acta* 31:747–765.

Velbel M. A. and Harvey R. P. 2009. Along-track compositional and textural variation in extensively melted grains returned from comet 81P/Wild 2 by the Stardust mission: Implications for capture-melting process. *Meteoritics & Planetary Science* 44:1519–1540.

Wasson J. T. 1993. Constraints on chondrule origins. *Meteoritics* 28:14–28.

Wasson J. T. and Krot A. N. 1994. Fayalite-silica association in unequilibrated ordinary chondrites: Evidence for

aqueous alteration on a parent body. *Earth and Planetary Science Letters* 122:403–416.

Weisberg M. K., Zolensky M. E., and Prinz M. 1997. Fayalitic olivine in matrix of the Krymka LL3.1 chondrite: Vapor-solid growth in the solar nebula. *Meteoritics & Planetary Science* 32:791–801.

Westphal A. J., Snead C. J., Butterworth A. L., Graham G. A., Bradley J. P., Bajt S., Grant P. G., Bench G., Brennan S., and Pianetta P. 2004. Aerogel keystones: Extraction of complete hypervelocity impact events from aerogel collectors. *Meteoritics & Planetary Science* 39:1375–1386.

Westphal A. J., Fakra S. C., Gainsforth Z., Marcus M. A., Orliore R. C., and Butterworth A. L. 2009. Mixing fraction of inner solar system material in comet 81P/Wild 2. *The Astrophysical Journal* 694:18–28.

Wood J. A. and Holmberg B. B. 1994. Constraints placed on the chondrule-forming process by merrihueite in the Mezö-Madaras chondrite. *Icarus* 108:309–324.

Wooden D. H. 2008. Cometary refractory grains: Interstellar and nebular sources. *Space Science Reviews* 138:75–108.

Zolensky M. E., Zega T. J., Yano T., Wirick S., Westphal A. J., Weisberg M. K., Weber I., Warren J. L., Velbel M. A., Tsuchiyama A., Tsou P., Toppani A., Tomioka N., Tomeoka K., Teslich N., Taheri M., Susini J., Stroud R., Stephan T., Stadermann F. J., Snead C. J., Simon S. B., Simionovici A., See T. H., Robert F., Rietmeijer F. J. M., Rao W., Perronnet M. C., Papanastassiou D. A., Okudaira K., Ohsumi K., Ohnishi I., Nakamura-Messenger K., Nakamura T., Mostefaoui S., Mikouchi T., Meibom A., Matrajt G., Marcus M. A., Leroux H., Lemelle L., Le L., Lanzirotti A., Langenhorst F., Krot A. N., Keller L. P., Kearsley A. T., Joswiak D., Jacob D., Ishii H., Harvey R., Hagiya K., Grossman L., Grossman J. N., Graham G. A., Gounelle M., Gillet P., Genge M. J., Flynn G., Ferroir T., Fallon S., Ebel D. S., Dai Z. R., Cordier P., Clark B., Chi M., Butterworth A. L., Brownlee D. E., Bridges J. C., Brennan S., Brearley A., Bradley J. P., Bleuet P., Bland P. A., and Bastien R. 2006. Mineralogy and petrology of comet 81P/Wild 2 nucleus samples. *Science* 314:1735–1739.

Zolensky M., Nakamura-Messenger K., Rietmiejer F., Leroux H., Mikouchi T., Ohsumi K., Simon S., Grossman L., Stephan T., Weisberg M., Velbel M., Zega T., Stroud R., Tomeoka K., Ohnishi I., Tomioka N., Nakamura T., Matrajt G., Joswiak D., Brownlee D., Langenhorst F., Krot A., Kearsley A., Ishii H., Graham G., Dai Z. R., Chi M., Bradley J., Hagiya K., Gounelle M., Keller L., and Bridges J. 2008. Comparing Wild 2 particles to chondrites and IDPs. *Meteoritics & Planetary Science* 43:261–272.